An Experimental and Numerical Investigation into the Vertical Dependence of Taylor-Columns Generated by a Rotating Disc

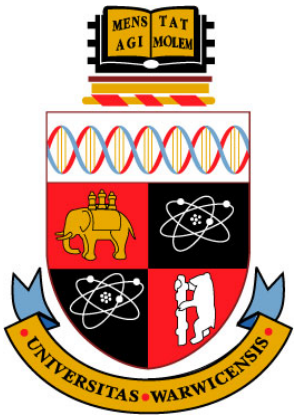

Jozef Hubertus Alfonsus Vlaskamp

School of Engineering

University of Warwick

A thesis submitted for the degree of

Doctor of Philosophy

April 2011

Contents

List of Figures

List of Tables

Acknowledgements

The author would like to express his gratitude to all the people who have helped to make the project possible.

First of all, I would like to thank Prof. Peter Thomas for his guidance during the project, and his support in using the experimental setup. Furthermore, I would like to thank Prof. Rainer Hollerbach for contributing many brilliant ideas to the project, as well as his invaluable support on the numerical and theoretical side.

I would like to thank the academic staff at the School of Engineering, most importantly Prof. Robert Kerr for his support on improving the numerical code and his very useful feedback and Prof. Peter Bryanston-Cross for his generous provision of the ”DaVis-dongle”. The technical staff at the School of Engineering are thanked for all their support, and their very skillful construction of the experimental equipment.

I thank the group from Hokkaido University, Japan, Prof. Yuichi Murai, Mr. Yuichi Nambu and Takahiro Yoshimoto for a great collaboration both inside the lab and out. I thank Prof. GertJan van Heijst of the Eindhoven University of Technology for many inspiring discussions.

My colleagues, especially Dr. David Hunter, Dr. Mark Brend, Ms. Sandy Gregorio, Mr. Ian Chandler, Mr. Visoth Tiev, Dr. Matthew Graves, Mr. James Brown, Mr. Carlos Duque Daza, Dr. James Jewkes and Ms. Amy Jones have been a infinite source of friendship and support throughout my time at the University of Warwick, for which I am very grateful.

Finally, I would like to thank Mr. Frank Vlaskamp, Mr. Daan Vlaskamp and Ms. Ioanna Stavrinidou for their continuing support throught my PhD.

Abstract

The presence of strong background rotation changes the dynamics of the fluid dramatically. The Taylor-Proudman theorem states that no variation in the velocity field may exist parallel to the axis of rotation when geostrophy applies. One of the most important implications of the Taylor-Proudman theorem is the presence of Taylor-Columns around solid objects moving in the fluid. The study presented here considers the Taylor-Columns generated by a differentially rotating disc located on the axis of rotation of a rotating fluid. The Taylor-Column rotates at an angular velocity intermediate to the disc and the tank, and is bounded by a vertical free shear layer. The large turntable at the University of Warwick allows a series of unique experiments to be performed in very deep water at high h/r, with h the water depth and r the disc radius.

A direct numerical simulation has been performed in spherical geometry, at h/r of 5,10 and 20 and Ekman numbers of $10^{-5} < E < 10^{-2}$. The results show the classic solution with no vertical dependence as predicted by the Taylor-Proudman theorem.

For the experimental investigation, a fully automated, traverse mounted stereo-PIV system has been developed which provides data-acquisition at different heights in the Taylor-Column. This allows investigation of the vertical dependence of the flow. Experiments have been performed with $E \sim 10^{-3}$ and $h/r = 80$. For positive differential disc rotation, a vertical dependence in the angular velocity was found, contradicting the Taylor-Proudman theorem and the numerical predictions. For negative differential rotation, this vertical dependence was not found. Stratification due to temperature gradients in the flow are suggested as a possible cause for the observed discrepancy.

Statement of Originality

The work presented in this thesis is my own work, except where noted. This material has not been previously submitted for another degree at a degree granting institution.

Chapter 1

Introduction

In many applications in Fluid Dynamics background rotation plays an important role. The weather system on Earth is greatly affected by the rotation of the Earth, by altering the direction of wind and ocean currents [8]. In the interior of planets rotation induces currents in the liquid outer core which have been suggested as the source of the magnetic field [14]. Engineering applications can be found in centrifugal separations [24] [33] or turbomachinery [39].

The presence of strong background rotation changes the dynamics of the fluid dramatically. The Taylor-Proudman theorem, derived in section 2.1, states that no variation in the velocity field can exist parallel to the axis of rotation when geostrophy applies [38]. The relative movement of solid bodies in the fluid produces Taylor-Columns, columns of fluid parallel to the axis of rotation which move together with the object.

The study presented here considers the Taylor-Columns generated by a differentially rotating disc located on the axis of rotation, as shown in figure 1.1. This setup is very

similar to the classic Stewartson-layer problem [35]. The rotating disc generates a Taylor-Column above and below itself, which rotates at an angular velocity intermediate between the disc rotation and the tank rotation. A thin boundary layer exists on the surface of the disc, the Ekman-layer, which reduces the angular velocity of the disc to the angular velocity of the Taylor-Column. A free shear layer is formed between the Taylor-Column and the quiescent fluid, the Stewartson layer. If the differential rotation is sufficiently strong, the Stewartson-layer will become unstable, and show patterns of waves as illustrated in 3.1.

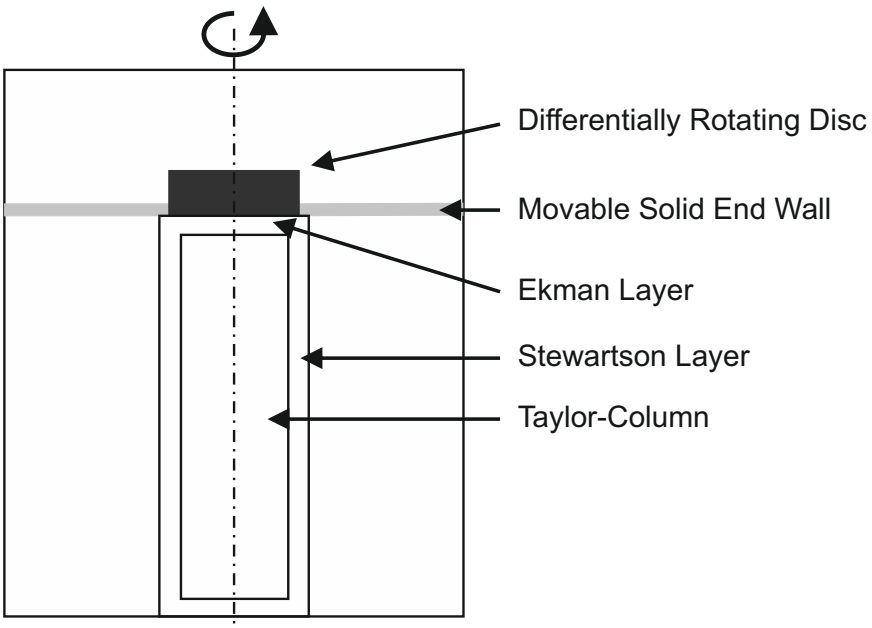

Figure 1.1: The experimental geometry. A differentially rotating disc is placed inside a rotating tank forming a Taylor-Column. An Ekman-layer exists on the disc, and vertical Stewartson layers are formed.

Previous experimental studies [3][9][13][28] have been performed in shallow water, with discs of relative large radius. Because of the shallow depth, none of the previous studies specifically investigated the possibility of a vertical dependence in the flow

which violates the Taylor-Proudman theorem. The large turntable facility at the University of Warwick, of which the water tank is 2.5m deep and 1m in diameter, allows experiments to be conducted on a much larger scale than possible in previous experiments. The much greater water depth allowed the first study of the vertical variation of the Taylor-Column in this geometry to be performed. The experimental work is supported by further numerical work using direct numerical simulation.

Two aspects of the flow are investigated: the angular velocity of the Taylor-Column, and the stability of the Stewartson layer. To measure at different heights of the tank, a fully-automated, translating stereo-PIV system has been developed. The development of the system is described in chapter 7.

The results of the numerical simulations are presented in chapter 5. Experimental results are presented in chapter 10.

Chapter 2

Theory

In this chapter a brief overview is given of the theoretical background of the project. The Taylor-Proudman theorem is first derived, after which the flow generated by a rotating disc in a rotating fluid is described.

2.1 Taylor-Proudman Theorem

The discovery of the most remarkable aspect of rotating flows, the uniformity along the axis of rotation, is attributed to Taylor [36] and Proudman [31], who derived the theorem and provided experimental verification.

The Taylor-Proudman Theorem can be derived as follows [38]:

The Navier-Stokes equations in a rotating frame are

$$\frac{\partial \mathbf{u}}{\partial t} + \mathbf{u} \cdot \nabla \mathbf{u} = -\frac{1}{\rho} \nabla p - \boldsymbol{\Omega} \times (\boldsymbol{\Omega} \times \mathbf{r}) - 2\boldsymbol{\Omega} \times \mathbf{u} + \nu \nabla^2 \mathbf{u} \tag{2.1}$$

with **u** representing the velocity, ρ the density, p the pressure, Ω the overall rotation rate and ν the kinematic viscosity.

The second term on the right hand side is the centrifugal force and the third term the Coriolis force.

The centrifugal force can be included in the pressure term by replacing the pressure by

$$p = p - \frac{1}{2}\Omega^2 r'^2; \tag{2.2}$$

Where r' is the distance to the axis of rotation.
The flow is assumed to be dominated by the Coriolis force, with inertial and viscous forces comparatively small, that is

$$|\mathbf{u} \cdot \nabla \mathbf{u}| \ll |\mathbf{\Omega} \times \mathbf{u}| \tag{2.3}$$

and

$$\left|\nu \nabla^2 \mathbf{u}\right| \ll |\mathbf{\Omega} \times \mathbf{u}| \tag{2.4}$$

equation 2.1 reduces to

$$2\mathbf{\Omega} \times \mathbf{u} = -\frac{1}{\rho} \nabla p \tag{2.5}$$

Taking the curl, this yields

$$\nabla \times (\mathbf{\Omega} \times \mathbf{u}) = 0 \tag{2.6}$$

which can be expanded to

$$\mathbf{\Omega} \cdot \nabla \mathbf{u} - \mathbf{u} \cdot \nabla \mathbf{\Omega} + \mathbf{u}(\nabla \cdot \mathbf{\Omega}) - \mathbf{\Omega}(\nabla \cdot \mathbf{u}) = 0 \tag{2.7}$$

The second and third terms are zero, as $\mathbf{\Omega}$ has no spatial dependence. The continuity equation remains

$$\nabla \cdot \mathbf{u} = 0 \tag{2.8}$$

which reduces equation 2.7 to

$$\mathbf{\Omega} \cdot \nabla \mathbf{u} = 0 \tag{2.9}$$

When the rotation axis is in the z-direction, this becomes

$$\Omega \frac{\partial \mathbf{u}}{\partial z} = 0 \tag{2.10}$$

As $\mathbf{\Omega} \neq 0$, this means

$$\frac{\partial \mathbf{u}}{\partial z} = 0 \tag{2.11}$$

In components

$$\frac{\partial u}{\partial z} = \frac{\partial v}{\partial z} = \frac{\partial w}{\partial z} = 0 \tag{2.12}$$

Which states there is no vertical variation in the velocity field parallel to the axis of rotation.

The Taylor-Proudman theorem predicts the existence of Taylor-Columns. If a solid object is moved around slowly, a column of fluid will form along the object parallel to the axis of rotation. In addition to the Taylor-Columns generated by differential rotation, as considered in this study, translational motion (either perpendicular or parallel to the axis of rotation) also creates Taylor-Columns. An example is the translation of a sphere [26] [40].

2.2 Non-Dimensional Numbers

The flow of a rotating disc in a rotating fluid is described by two non-dimensional numbers, the Ekman number and the Rossby number.

The Ekman number is defined as

$$E = \frac{\nu}{\Omega L^2} \tag{2.13}$$

with ν the kinematic viscosity, Ω the rotation rate of the tank and L a length scale.

Various length scales are used for L. In Oceanography, where the vertical length scale is often orders of magnitude smaller than the horizontal length scale, the Ekman number is usually defined with the water depth as length scale [8]. In laboratory experiments, either the disc radius [13] or water depth [9] are used. While in some studies the radius and depth are in the same order of magnitude and the choice is unimportant [9], this is certainly not the case for the experiments performed in this study. To differentiate between the two definitions, they are defined as:

$$E_r = \frac{\nu}{\Omega r^2} \tag{2.14}$$

with r the radius of the disc, and

$$E_h = \frac{\nu}{\Omega h^2} \tag{2.15}$$

with h the water depth or height of the vessel.

When discussing previous (experimental) work, the definition used by the authors of

the study will be retained. The numerical code used in the present study is in spherical geometry, and uses an Ekman number defined on the radius of the inner sphere, and is essentially equivalent to E_r.

The Rossby number is defined as

$$Ro = \frac{\omega}{\Omega} \tag{2.16}$$

with ω the differential rotation of the disc. When Ro is negative, the disc spins anti-cyclonically. Note that ω is the rotation within the rotating frame of reference. The absolute rotation of the disc in the inertial lab-frame is $\Omega + \omega$.

2.3 Taylor-Columns Generated by a Rotating Disc

Stewartson [35] first considered the problem of two rotating discs on the axis of rotation on opposite sides of a rotating tank in 1957, as shown in figure 2.1. The addition of a second disc introduces an additional symmetry, which simplifies the analysis. As the Taylor-Column is forced from both sides, the angular velocity in the interior is equal to ω. The angular velocity in the Taylor-Column is adjusted to the background rotation rate by two nested shear layers, the Stewartson-layers, of thickness $O(E^{1/3})$ and $O(E^{1/4})$, of which the $E^{1/4}$ layer providing most of the change in angular velocity.

The Ekman-layer of thickness $O(E^{1/2})$ adjusts from the velocity of the disc to the velocity in the interior of the Taylor-Column. For the two-disc configuration, the difference in angular velocity between the disc and the interior of the Taylor-Column is small, and the Ekman-layer is expected to play a minor role. In the single-disc configuration,

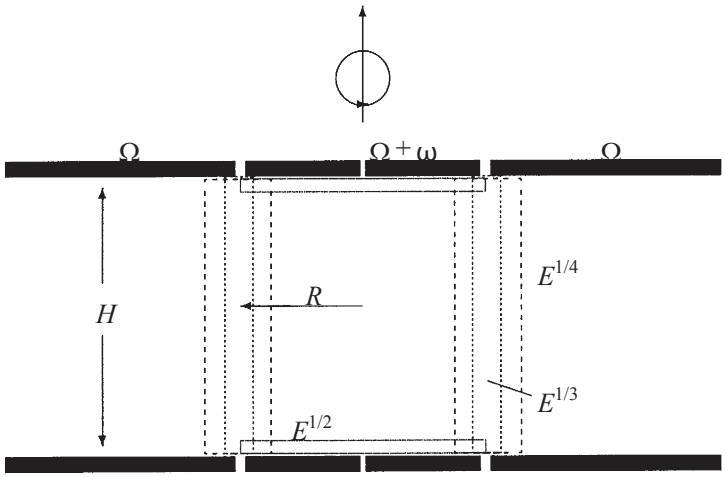

Figure 2.1: The Stewartson-layer solution for flow between two discs rotating differentially to the background rotation. Reprinted from [9].

the Taylor-Column rotates at $\omega/2$, intermediate between the disc and the tank, and the adjustment of the angular velocity over the Ekman-layer is significant [16].

A secondary meridional circulation is induced in the flow by the Ekman layers in the single disc configuration, as shown in figure 2.2. When the fluid is in solid body rotation, the centrifugal forces are balanced by a pressure gradient. Close to the disc, for $\omega > 0$, the local angular velocity is higher than in the interior of the Taylor-Column, and a net outward centrifugal force remains which pumps fluid out of the interior of the Taylor-Column spinning it outwards. The fluid travels downward in the $E^{1/3}$ layer, and moves inwards in the bottom Ekman-layer completing the circuit. For $\omega < 0$ the flow is reversed.

Due to the lesser importance of the Ekman-layer in the two-disc configuration, it can be expected that the meridional circulation equally is less important or is indeed absent altogether. Numerical simulations by Aguiar [3] however show that a meridional circulation does exist in the two-disc configuration, where it is confined to the edge of

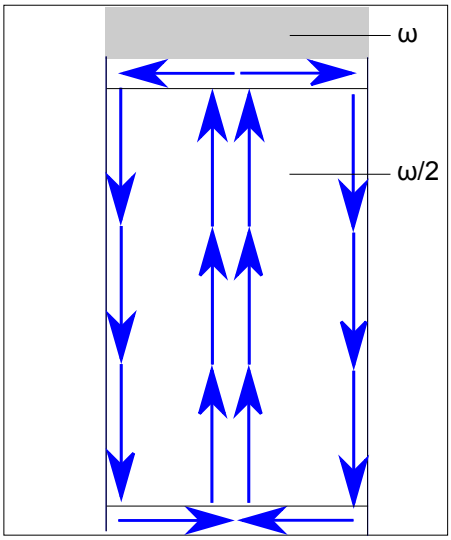

Figure 2.2: The meridional circulation for the single-disc configuration. Fluid is forced outward by the centrifugal force in the Ekman-layer on the disc surface, transported downwards in the Stewartson-layer, inwards on the lower Ekman-layer completing the circuit through the Taylor-Column.

the Taylor-Column, with flow returned at mid-height.

The vertical extent of Taylor-Columns generated by a single rotating disc have been calculated by Greenspan [11] to be $E^{-1}r$. In practical experiments in water, where $\nu = 10^{-6}$, $\Omega \sim 10$RPM and $r \sim 2.5$cm, the lowest E_r attained is $\sim 10^{-3}$, predicting Taylor-Columns of length $10^3 r$, which is practically infinite.

2.4 Rayleigh-Criterion

The flow is hydrodynamically stable if the Rayleigh-Criterion is satisfied, i.e. if the angular momentum increases outward. A physical interpretation [17] is shown in figure 2.3. If the angular momentum increases outwards and a fluid parcel is displaced from

r to $r + d$ with $d > 0$, the parcel will have insufficient angular momentum to maintain its new position and will be pushed back to its original position. If $d < 0$ the angular momentum will be too large for the new position, and the parcel will move outwards to its original position. The flow is therefore stable to small perturbations.

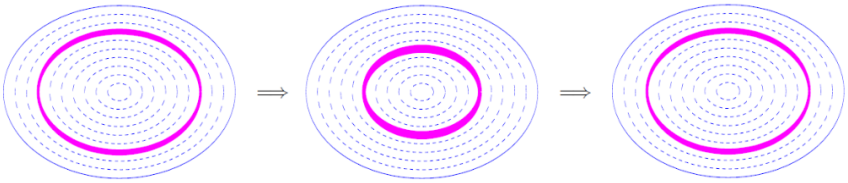

Figure 2.3: A physical interpretation of the Rayleigh criterion. When the flow is stable, a displaced parcel will return to its original position. Adapted from [17]

The Rayleigh-Criterion for the experimental configuration can be written as:

$$r^2(\Omega + \omega) > (r + d)^2\Omega \tag{2.17}$$

with r the radius of the disc, d the width of the shear layer, Ω the overall rotation rate and ω the differential rotation.

Expanding equation 2.17 yields

$$r^2\Omega + r^2\omega > (r^2 + d^2 + 2rd)\Omega \tag{2.18}$$

By dropping $d^2\Omega$, which is small compared to the other terms, and crossing out $r^2\Omega$

on both sides this reduces to

$$r^2\omega > 2rd\Omega \tag{2.19}$$

This can be rearranged to

$$\frac{\omega}{\Omega} > \frac{2d}{r} \tag{2.20}$$

Using $Ro = \frac{\omega}{\Omega}$, and $d = E^{1/4}r$ as an estimate for the shear layer thickness this becomes

$$Ro > 2E^{1/4} \tag{2.21}$$

If $E = 10^{-3}$, then the critical Ro becomes

$$Ro_c \approx 0.35 \tag{2.22}$$

For the experimental study with $E_r \sim 10^{-3}$, the Rayleigh-Criterion predicts that $Ro_c \approx 0.35$.

Chapter 3

Previous Experimental Work

A number of experimental studies have previously been performed investigating the Taylor-Columns generated by a rotating disc. A summary of these studies and their results is given below.

3.1 Hide and Titman

Hide and Titman [13] performed the first experimental study in 1967. A cylindrical Perspex tank of 30cm high and 19cm radius has been used, with 5 discs of diameters between 2.5 and 7.5cm positioned at 22cm from the bottom of the tank. The tank is fitted with a lid, and thus has solid boundaries at both the top and bottom. The primary visualisation technique is dye.

No quantitative measurements of the azimuthal velocity in the Taylor-Column have been performed. Qualitatively the Taylor-Column has been observed to “rotate at a

uniform speed intermediate between that of the tank and that of the disc". The experiments performed by Hide and Titman have an emphasis on finding the critical Rossby number, Ro_c, and the instability modes, as well as some measurements of the meridional circulation. The instabilities resemble waves superposed on the circular Taylor-Column, drawings of their visualisations are reproduced in figure 3.1.

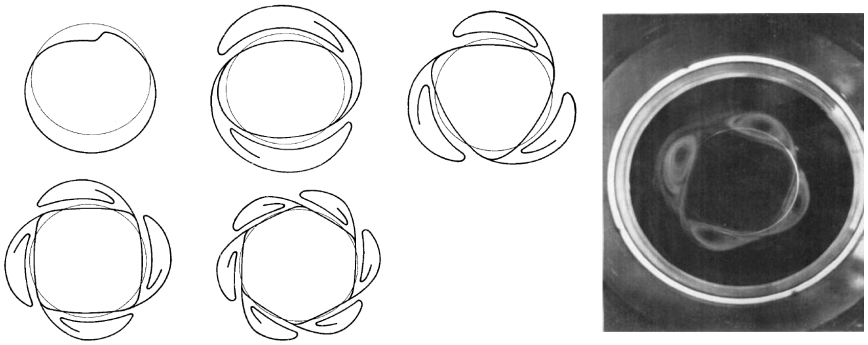

Figure 3.1: Drawings of the instabilities as observed by Hide and Titman. On the right, a photograph of a mode 4 instability. Reprinted from [13]

In figure 3.2 the experimentally determined regime diagram is reproduced. Ro_c was found to be independent of the sign of differential rotation and the radius of the disc, with a best fit for the dependence of Ro_c on E given by $Ro_c = 16.8E_r^{0.568}$.

While the critical value for positive and negative Ro is similar, a strong asymmetry in the observed critical instability modes exists. While for positive Ro instabilities with $m = 2$ to $m = 6$ have been found, with m representing the number of half waves superposed on the circular flow as shown in figure 3.1. For negative Ro only $m = 1$ has been observed. No cause of this asymmetry has been identified. If the Rossby number is increased further above the critical value this reduces the number of waves, and settles down at $m = 2$ for $Ro > 0.2$.

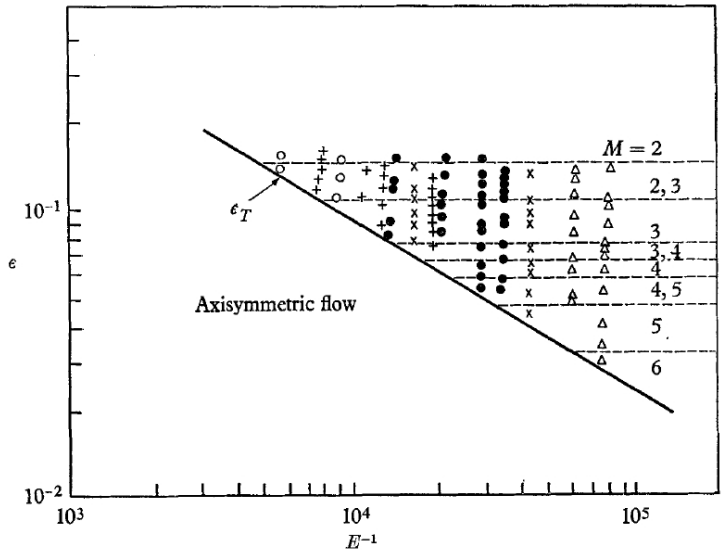

Figure 3.2: The regime diagram as found by Hide and Titman. In the graph, *Ro* is denoted by ϵ. The Ekman number is based on the radius of the disc. Reprinted from [13]

An important feature of the experimental configuration used by Hide and Titman is the positioning of the disc. The 2.5cm thick disc is submerged in the centre of the tank. This causes a discontinuous step in fluid height to exist at the edge of the disc, with much greater thickness than the Ekman-layer thickness of $\sim$ 3mm. It has been suggested that this feature is responsible for the asymmetry found in the instability modes [16].

3.2 Niino and Misawa

Niino and Misawa [28] performed a series of experiments with two counter-rotating concentric discs in a rotating tank in 1984. The experimental geometry is shown in figure 3.3. The smaller disc, of radius 20.0cm is rotated differentially with the tank

at $+\omega$, and the larger disc with radius 39.0cm is rotated at $-\omega$. This introduces an additional symmetry in the experiment. The overall radius of the tank is 39.2cm, and it can be rotated up to 11RPM. The fluid depth is relatively shallow, at 10.3cm and is bounded by a rigid lid at the top. The flow is visualised by generating coloured fluid in the Ekman layer.

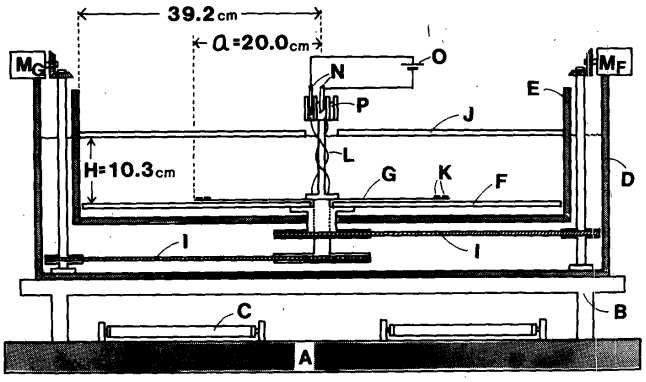

Figure 3.3: The experimental setup used by Niino and Misawa. The inner disc G is spun with ω and the outer disc with $-\omega$. Tank A is spun at Ω. Full details on the experimental setup can be found in the original paper. Reprinted from [28]

The flow is assumed to have no vertical variation, and no direct measurements of the azimuthal velocity have been performed. The non-dimensional parameter chosen to characterise the flow is the Reynolds number rather than the Rossby number, defined as $Re = VL/\nu$. It was found that the stability of the flow can be determined purely by this Reynolds number, with the flow going unstable above $Re_c = 11.7$. The stability criterion was found not to depend on the overall tank rotation Ω.

The influence of the circular geometry on the stability of the flow has been investigated, and high curvature was found to stabilise the flow. The shear layer thickness is defined as $L = (E/4)^{(1/4)}H$, and the non-dimensional radius as $\gamma = r/L$. The circular geometry

becomes unimportant when the vertical shear layer is thin relative to the disc radius, when $\gamma > 25$. All experiments have been performed in relatively shallow water with a large radius disc, with $25 < \gamma < 50$, at which the effects of the circular geometry are expected to be negligible.

Instability modes have been determined only for positive differential rotation of the (inner) disc, and therefore provide no further insight in the asymmetry observed by Hide and Titman. The regime diagram is reproduced in figure 3.4. Niino and Misawa use a non-dimensionalised wavenumber, defined as $k = (E/4)^{1/4}Hn/a$. The number of waves observed physically, n, is an integer, but the non-dimensionalisation causes k to behave continuously due to the inclusion of a continuous Ek.

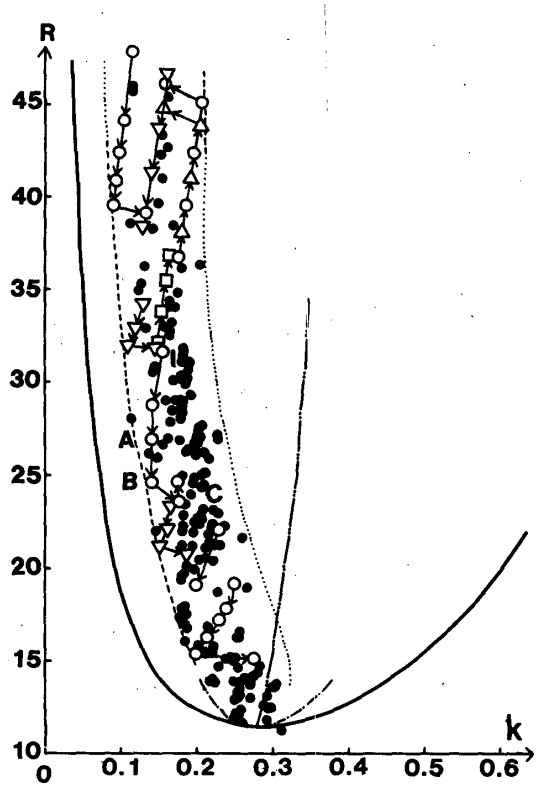

Figure 3.4: The regime diagram found by Niino and Misawa. Reprinted from [28]

3.3 Früh and Read

Früh and Read [9] performed a series of experiments with a split-disc setup in 1999. Two discs are placed on the axis of rotation, at opposite sides of the tank. The discs sit flush with the lid and bottom, and are spun at the same differential rotation rate. This introduces a top-down symmetry not present in Hide and Titman or Niino and Misawa's experiments, but with a close similarity to Stewartson's theoretical work. Measurements are performed using both Laser Doppler Velocimetry and a 2D PIV system.

The regime diagrams are reproduced in figure 3.5 for positive *Ro* and figure 3.6 for negative *Ro*. For both positive and negative differential rotation of the discs instability modes $m \geq 2$ have been found.

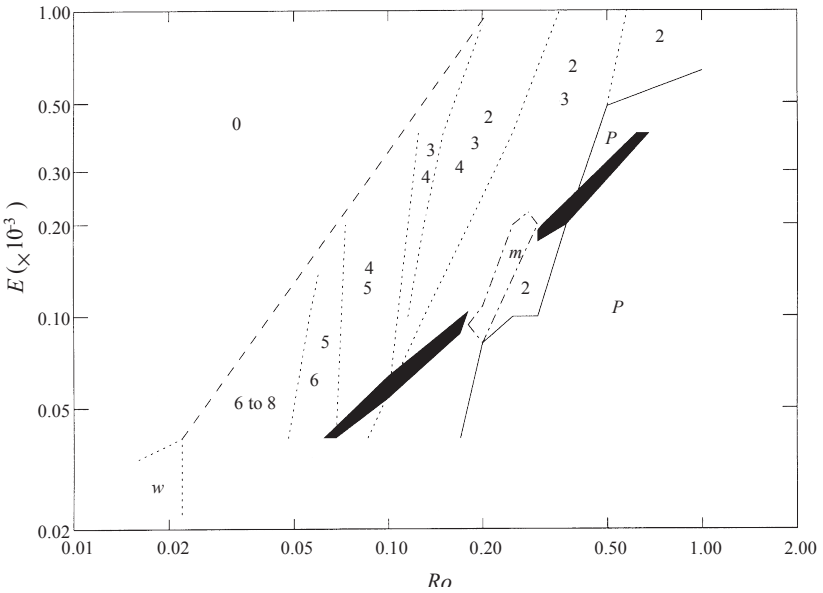

Figure 3.5: The regime diagram found for +*Ro* by Früh and Read. Reprinted from [9].

The "noisy vortex" regime, denoted by *nV*, in figure 3.6, is only found for a small

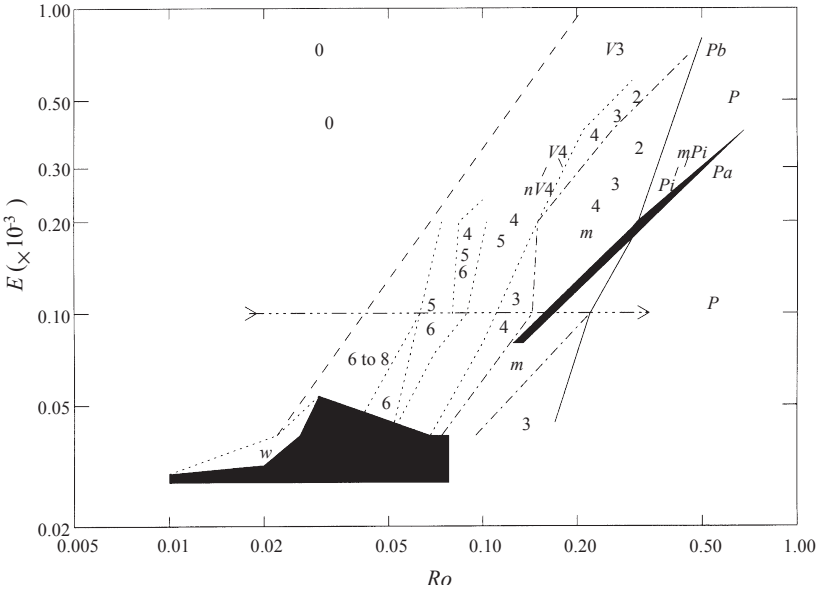

Figure 3.6: The regime diagram found for $-Ro$ by Früh and Read. Reprinted from [9].

number of conditions. It is characterised by a significant increase in the background noise in the signal. Noise spikes are in the same order as the flow velocity in the Taylor-Column. Analysis of the signal found that "the noisy vortex state contains the same deterministic dynamics as the periodic vortices only with added white noise."

The "period-doubled"-vortex regime occurs at high Ro. This is described as "a spatially period-doubled flow with strong $m = 1$ and $m = 2$ components of one strong and one weak vortex in a distorted jet stream." An example is shown in figure 3.7.

The results of Früh and Read for the most unstable mode are not consistent with the observations of Hide and Titman. Früh and Read found that the sign of Ro is unimportant in determining the mode number, with $2 < m < 6$ for both $\pm Ro$. Hide and Titman found $\pm Ro$ producing distinctly different results, indicating that the sign of Ro is important. Früh and Read suggest the difference in geometry between the two experiments is a possible cause. By placing a relatively thick disc in the centre of the

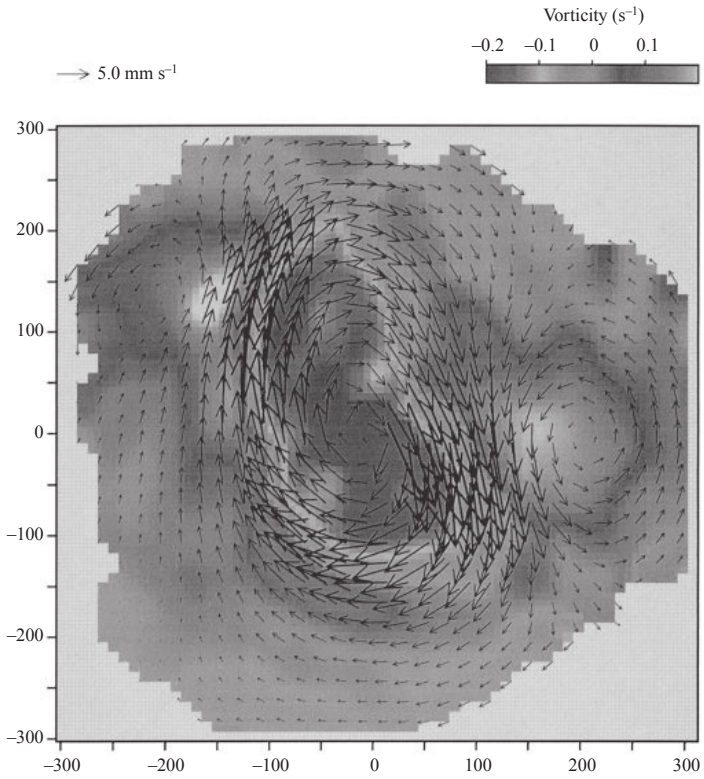

Figure 3.7: A period doubled vortex as found by Früh and Read at high *Ro*. Reprinted from [9].

tank in Hide and Titman's experiments, a discontinuous step in fluid height is present. In Früh and Read's experiments, the disc sits flush with the boundaries, and there is no such step in fluid height.

3.4 Hollerbach

Hollerbach [16] further investigated the discrepancy between the results of Früh and Read and Hide and Titman numerically in 2003. Simulations are conducted in a differentially rotating spherical shell, which gives rise to similar Stewartson-layers and

instabilities as are found in cylindrical geometry. The geometry most closely resembles the geometry of Hide and Titman, and the results, shown in figure 3.8, exhibit the same asymmetry in m for $\pm Ro$. 1

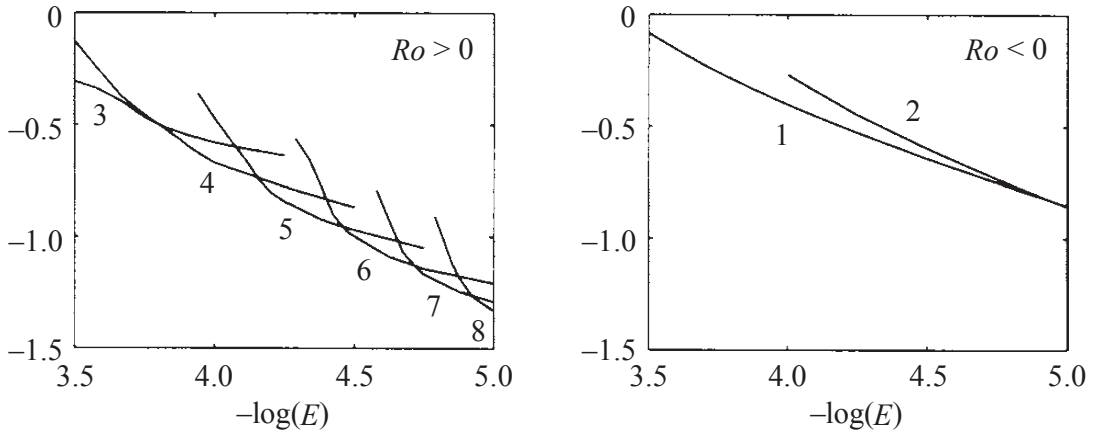

Figure 3.8: The numerical results from Hollerbach show a similar asymmetry as in Hide and Titmans experimental results. Reprinted from [16].

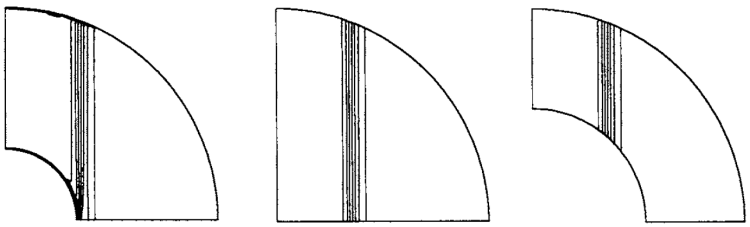

Figure 3.9: Contours of the angular velocity. The original solution (left) is extended into a full sphere (middle) or reduced with a larger inner sphere (right). Reprinted from [16].

Similar to Hide and Titman's experiments, the spherical geometry of the numerical simulation has a discontinuous step in fluid height at the edge of the inner sphere. The axisymmetric flow is (nearly) independent of z, and it is straightforward to extend the solution to a full sphere, which effectively removes the inner sphere completely. The

second method of removing the step in fluid height is enlarging the inner sphere, while keeping the solution for the basic state found for the smaller sphere, which moves the step in fluid height away from the edge of the Stewartson layers. Both geometries are shown in figure 3.9.

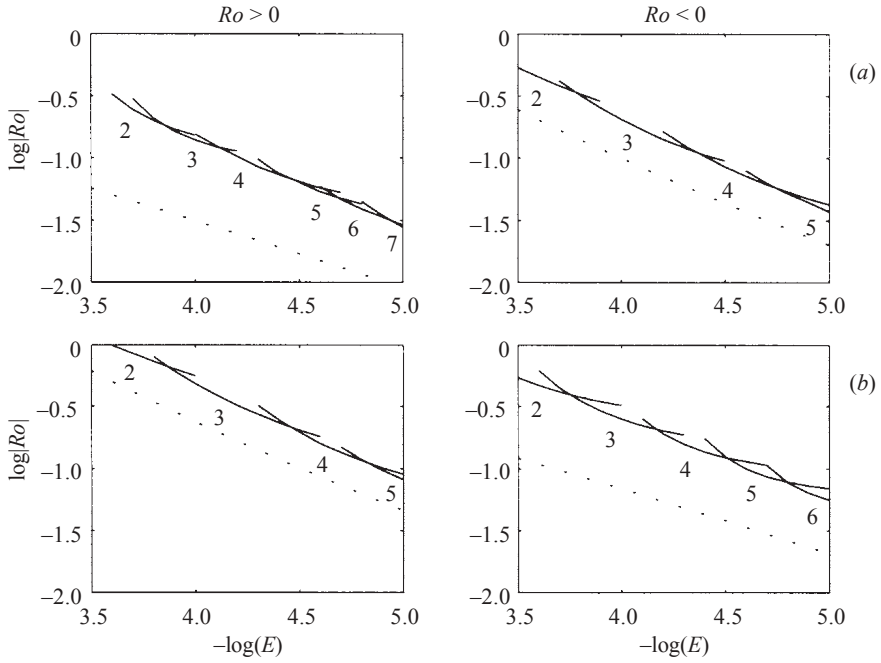

Figure 3.10: By extending the solution to a full sphere (top) or by increasing the size of the inner sphere (bottom) the results change dramatically, and are consistent with Früh and Read. Image reprinted from [16].

The results obtained with both the larger inner sphere and the full sphere, shown in figure 3.10, are significantly different compared to figure 3.8. For both $\pm Ro$ the instabilities progress to higher m, consistent with the results found by Früh and Read. This proves that the geometry is the crucial factor that explains the discrepancy between the earlier experimental studies.

3.5 Aguiar

Aguiar [3] performed further work on the same experimental setup as Früh and Read in 2008, with a number of new configurations to try to further investigate the cause of the discrepancy between the results of Hide and Titman and Früh and Read.

For discs flush with or having a small displacement relative to the end-walls, Aguiar found no significant difference between the instability modes produced by $\pm Ro$. For a single thick immersed disc of 1.5cm thickness, a difference between $\pm Ro$ has been found, with typically $m_{Ro>0} = m_{Ro<0} + 4$. While this asymmetry is not as pronounced as Hide and Titmans results, it is nonetheless a significant difference. A repetition of the experiment with a thin disc of 0.5cm showed no asymmetry, and it has been concluded that the thickness of an immersed disc determines m. Experiments with a sloping bottom around the disc, with a smooth variation in fluid height, do not show a wave number asymmetry. This is seen as confirmation of Hollerbach's hypothesis that the step in fluid height is necessary for the asymmetry to occur.

No attempts have been made to investigate any vertical dependence of the flow. The PIV-system used by Aguiar uses a very thick lightsheet of 4cm relative to the fluid depth of 10cm, which makes it unsuitable for this kind of study. Furthermore, in the two-disc configuration the vertical shaft through the centre of the tank will provide additional forcing which may suppress any vertical variation.

Chapter 4

Objectives

According to the Taylor-Proudman theorem, there is no vertical variation in the flow. This is indeed observed by previous studies, both numerically [16] and experimentally [13],[28], where, apart from very thin Ekman layers on the disc and the solid boundaries, no vertical variation has been observed. Theoretical predictions of the length of the Taylor-Column are of order of $1000r$, which is much greater than could be achieved in any existing experimental setup, or can be accessed easily computationally.

None of the previous experimental studies have performed detailed quantitative studies of the vertical variation in the angular velocity in the Taylor-Column. They have been significantly limited in this respect by the relatively shallow tanks used and by technical limitations in flow visualisation. Furthermore, the theory predicts that there should not be any variation at all even in much deeper tanks, and investigating vertical variation has understandably not been a priority in any of the studies.

The large rotating turntable at Warwick offers a much deeper tank of 2.5m, allow-

ing for a much greater depth-to-radius ratio than in previous studies. Using modern flow-visualisation quantitative measurements of the azimuthal velocity inside the Taylor-Column can be made at different heights. This provides a unique possibility to investigate the validity of the Taylor-Proudman theorem in relatively deep water.

In addition to the measurements of the azimuthal velocity, the instability modes produced by the Taylor-Column are to be investigated further, both with and without solid boundaries around the disc to produce geometries similar to respectively Früh and Read and Hide and Titman. This is supported by further numerical work.

The design and implementation of the Particle-Image-Velocimetry (PIV)-system is an important technical objective. The large size of the experimental apparatus, combined with the objective to measure the flow at different heights, necessitate a custom designed, state-of-the-art stereo-PIV system that is small and light enough to be mounted on a traverse on the side of the tank. Full automation of the system and re-usability for future projects are equally important design goals.

4.1 Summary of Objectives

The objectives of the study are, in order of importance:

1. Experimentally determine the vertical dependence of the azimuthal velocity in the Taylor-Column in very deep water.
2. Determine the instability modes both numerically and experimentally.
3. Construct a fully automated stereo-PIV system suitable for measuring velocities in the horizontal plane at different heights of the tank.

Chapter 5

Numerical Simulation

A series of numerical simulations have been performed, starting in mid-2007 and running until end-2010. The simulations support the experimental work, by providing predictions of the stability and structure of the Taylor-Column. The numerical code is a direct numerical simulation of the closely related problem of two differentially rotating concentric spheres, developed by Hollerbach [15]. The geometry is shown in figure 5.1 The numerical code is used to predict the angular velocity distribution as well as the critical Rossby number and instability modes in the flow, by solving the Navier-Stokes equation in spherical geometry.

For the purpose of the current investigation the numerical code has mostly been used unmodified to the original, with no changes made to the algorithms in the code, and only minor code changes have been made for efficiency reasons. A more detailed description of the underlying algorithms used in the code can be found in [15].

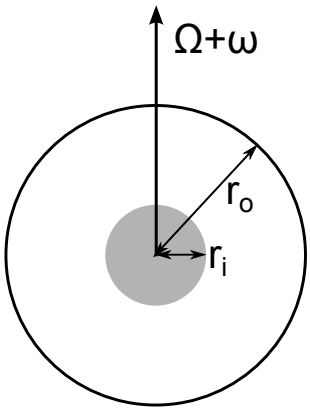

Figure 5.1: The numerical code computes the flow between two differentially rotating concentric spheres

The difference in geometry between the simulations and experiments may cause small differences in the flow field. To investigate this, a repetition of experiments can be run with a spinning half-sphere at the top of the tank replacing the disc, providing a very close similarity in geometry. Due to time constraints imposed by the relocation of the facility, it was not possible to conduct this additional experimental study at the time of writing.

5.1 Axisymmetric Basic State

The first phase of the simulation computes the axisymmetric basic state. The Navier-Stokes equation is written as [16]:

$$\frac{\partial \mathbf{U}}{\partial t} + Ro\mathbf{U} \cdot \nabla \mathbf{U} + 2\hat{\mathbf{e}}_z \times \mathbf{U} = -\nabla p + E_r \nabla^2 \mathbf{U} \tag{5.1}$$

with the Ekman number defined as

$$E_r \equiv \frac{\nu}{\Omega(R_i)^2} \tag{5.2}$$

and the Rossby number as

$$Ro \equiv \frac{\omega}{\Omega} \tag{5.3}$$

Equation 5.1 is solved using a spectral solver. Depending on the required resolution, calculating the axisymmetric basic state requires between a few hours on a single processor at low resolution to several months on 8 processors at high resolution.

5.2 Non-Axisymmetric Instabilities

Once the axisymmetric basic state has been found, the next phase is to test the stability of individual modes. Linearising equation about the obtained axi-symmetric basic state U_0, the following equation is obtained [16]:

$$\frac{\partial \mathbf{u}}{\partial t} + Ro(\mathbf{u} \cdot \nabla \mathbf{U_0} + \mathbf{U_0} \cdot \nabla \mathbf{u}) + 2\hat{\mathbf{e}}_\mathbf{z} \times \mathbf{u} = -\nabla p + E_r \nabla^2 \mathbf{u} \tag{5.4}$$

As the different non-axisymmetric modes decouple, each mode can be time-stepped individually and the code can effectively remain 2D, which reduces memory and processing demands. The code is run until the most dominant eigenmode emerges. Due to the large number of modes to be tested, this is the most time consuming step.

To find the critical Rossby number Ro_c, the axisymmetric basic state is first computed for a given E_r and Ro, before time-stepping equation 5.4 for several values of m. If the solution grows or decays, Ro is decreased or increased and the process is repeated, including the calculation of the basic state. This is repeated until the growth rate is 0, where the shear layer first becomes unstable.

5.3 Choice of Parameter Range

In addition to E and Ro the radius-ratio between the two spheres, defined as R_o/R_i as shown in figure 5.1, needs to be set. Increasing R_o/R_i effectively reduces the size of the inner sphere. A small inner sphere increases the computational resources needed, in order to accurately resolve the small scale flow structures.

The availability of computing resources dictates the parameter range that is numerically accessible. R_o/R_i is the most important parameter in determining the amount of memory and processor time required. Decreasing the Ekman number or increasing the Rossby number will also increase the computational cost significantly. Fortunately, when the Ekman number is decreased the critical Rossby number also decreases, which partially mitigates the increased computational expense at low Ekman numbers.

To allow a direct comparison between numerical simulation and experimental results ideally an overlap exists between the parameter ranges of both. Numerical work and experimental work are unfortunately bound by different, conflicting, constraints. Due to the size of the apparatus, a large radius-ratio (the ratio between the radius of the disc

and the depth of the tank) is favourable, as a small disc is advantageous from a flow visualisation point of view. The rotation rates of both the tank and disc are heavily limited by technical constraints, whereas very small or very large rotation rates can easily be achieved numerically.

The three discs originally designed for the experimental work correspond to $R_o/R_i = 40$, $R_o/R_i = 80$ $R_o/R_i = 160$ numerically, with corresponding Ekman numbers $E_r \sim 10^{-3}$. The smallest $R_o/R_i = 40$ was initially chosen as a starting point for the numerical work, with $E_r = 10^{-3}$. However, this proved too ambitious, both in terms of required memory and run time. The more modest $R_o/R_i = 10$ has greatly reduced processor and memory requirements, and has been chosen as a new starting point. $R_o/R_i = 5$ $R_o/R_i = 20$ have been added at a later date, to investigate the dependence of the solution on R_o/R_i.

The supercomputers do not provide a simple mechanism to determine the total processor time required for each simulation, which consists of many shorter runs until the solution converges. The very large number of individual runs made keeping a manual tally impractical, therefore detailed total run-times are not available. For purposes of determining the parameters to use for the simulation, most importantly R_o/R_i and E_r, only rough order of magnitude estimates of the run time were needed. The total runtime consumed for all numerical work is estimated to be in excess of 50 processor years.

At all three values of R_o/R_i processing time increased dramatically around $E_r = 10^{-5}$.

This limited the simulation to relatively high E_r. Running above $E_r = 10^{-3}$ also proved challenging, both due to the high critical Ro and the difficulty getting a converged solution for the axisymmetric basic state. This limited the easily accessible numerical range to $10^{-3} < E_r < 10^{-5}$.

5.4 Compilers and Parallelisation

Various computers have been used to run code, a full list of the machines is given in appendix A. Originally, the code was compiled with the G77 Fortran compiler, and run as a serial code running on a single processor. When the switch to the supercomputers Francesca and Skua was made, this became a problem. The memory and processor requirements of the code are significant when run in the envisioned parameter range, and a serial code leads to very inefficient use of resources on the supercomputers and very long running time. Finding the critical Rossby number is an iterative process, which compounds the problem of a very long running time: one set of parameters is ideally run completely before moving on to the next estimate. With a large number of processors it is possible to run many simulations at the same time, trying several estimates simultaneously. This is, however, a very inefficient strategy as many conditions will be run needlessly.

The two supercomputers, Skua and Francesca, are optimised for parallel codes, with relatively small amounts of memory per core. Running a code with large memory requirements on a supercomputer can therefore lead to significant processor wastage, as a node has unused processors but no free memory. The growing trend for multi-core

processors even in low-end computers means this problem is no longer confined to the supercomputer or workstation realm, and parallelism is gaining importance even for commodity hardware. On Skua, which was the most heavily used machine in this project, processors are allocated in pairs, with 3.9GB of RAM available per pair. Running a serial code wastes a minimum of 1 processor, which increases to 3, 5, 7 or more processors wasted each time another multiple of 3.9GB of RAM is requested. This lead to very poor efficiency in running the code, which needed to be addressed before large scale computation could be performed.

The necessary improvements to the code have been made mid-2008, which involved changing to the Intel Fortran compiler and restructuring some of the loops. The Intel Fortran compiler offers an automatic parallelisation option, which has been used successfully on the modified code. The changes made to the code and compiler showed a very significant improvement: benchmarking showed the code to run 5 times quicker compared to G77 even without any parallelisation, with near perfect scaling for computing the non-axisymmetric instabilities of up to 8 processors on large memory runs. This reduces the real time required to run a simulation by a factor 40, benchmarks are shown in table 5.1.

Table 5.1: Total runtime and relative speedup for a partial run with 6GB memory requirement

	G77 1 CPU	IFORT 1 CPU	IFORT 4 CPU	IFORT 8 CPU
Runtime	1022	225	55	24
Relative Speedup	1	4.5	18.6	42.6

The improvement in processing speed represents a huge efficiency gain. The reduced

processor wastage combined with the basic improvements in compiler efficiency translate into a improvement in efficiency of a factor 10 for simulations requiring less than 3.9GB of RAM, to a factor 40 for codes requiring more than 11.7GB of RAM.

5.5 Results

5.5.1 Angular Velocity

The computed angular velocity, of which a typical plot is shown in figure 5.2, shows the classical Stewartson-layer solution for $E < 10^{-3}$, with the Taylor-Column reaching the outer sphere and no vertical variation in the angular velocity. Similar to Hollerbach's [16] results, the axisymmetric basic state shows very little dependence on Ro for a given E_r. Near the centre of the Taylor-Column the angular velocity is in the order of 0.5ω, reducing to 0 near the edge, which is consistent with the theoretical predictions.

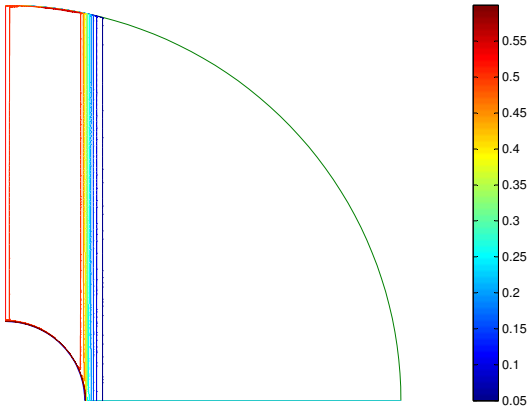

Figure 5.2: A typical angular velocity contour for $R_o/R_i = 5$, $E_r = 10^{-5}$ and $Ro = 0.02$

5.5.2 Critical Rossby number

The critical Rossby number is plotted in figure 5.3 for $+Ro$ and figure 5.4 for $-Ro$. For $-Ro$, the critical Ro is significantly higher than for $+Ro$, meaning that anti-cyclonic disc rotation is more stable than positive.

Ro_c has a comparatively small dependence on R_o/R_i. Ro_c scales with E_r approximately as

$$Ro_c \propto E_r^a \tag{5.5}$$

The current study extends the parameter range to much greater R_o/R_i. Values for a obtained are found to be in agreement with the previous experimental, theoretical and numerical work. Table 5.2 shows a comparison between the different studies.

Table 5.2: Values for a of difference studies for the scaling of $Ro_c \propto E^a$

	Busse [7]	Hide & Titman [13]	Früh & Read [9]	Hollerbach [16]	Ratio=5	Ratio=10	Ratio=20
Ro	0.75	0.6	0.72	0.65	0.64	0.74	0.68
$-Ro$	0.75	0.6	0.72	0.45	0.47	0.48	0.63

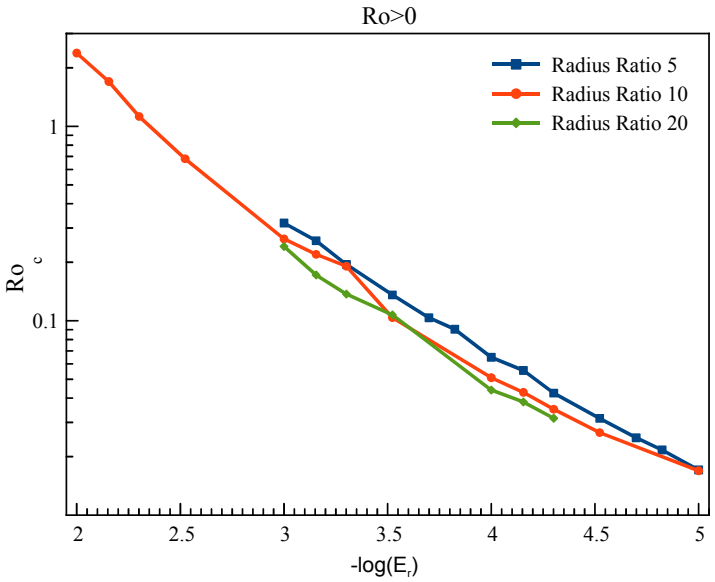

Figure 5.3: The critical Rossby number for $Ro > 0$ as a function of E_r

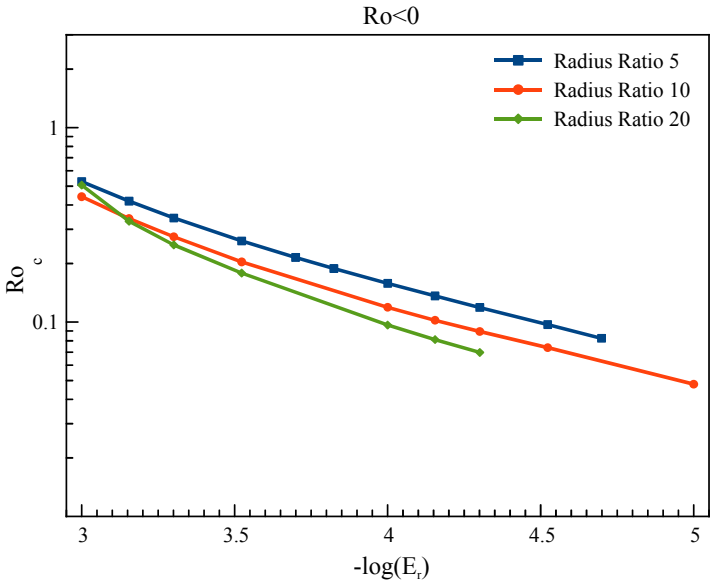

Figure 5.4: The critical Rossby number for $Ro < 0$ as a function of E_r

5.6 Instability Modes

The most unstable modes for positive Ro are shown in figure 5.5, 5.6 and 5.7 for different values of R_o/R_i. While Ro_c does not have a strong dependence on R_o/R_i, the mode number m does. At $R_o/R_i = 5$, shown in figure 5.5, m increases very rapidly with decreasing E_r, reaching $m = 10$ at $E_r = 10^{-5}$. At the same E_r, $R_o/R_i = 10$, shown in figure 5.5, reaches $m = 6$. For E_r, $R_o/R_i = 20$, at the same E_r only $m = 4$ is reached.

The rapid increase in m for $R_o/R_i = 5$ greatly increased the processing time at low E_r. A much greater number of modes needs to be tested, and each run took longer to converge. While the resolution could be much lower than the higher R_o/R_i, the total runtime did not decrease significantly at low E_r. Around $E = 10^{-5}$ the processing time starts increasing dramatically, which puts them beyond the reach of current computing resources.

For $-Ro$, the results are consistent with Hide and Titman [13], the study which the numerical geometry most closely resembles, with mode 1 being dominant. Only at low E_r and $R_o/R_i = 5$, $m = 2$ is found. While fewer modes need to be tested for $-Ro$, the run time has been found to be longer, with similar dramatic increases in processing time around $E_r = 10^{-5}$.

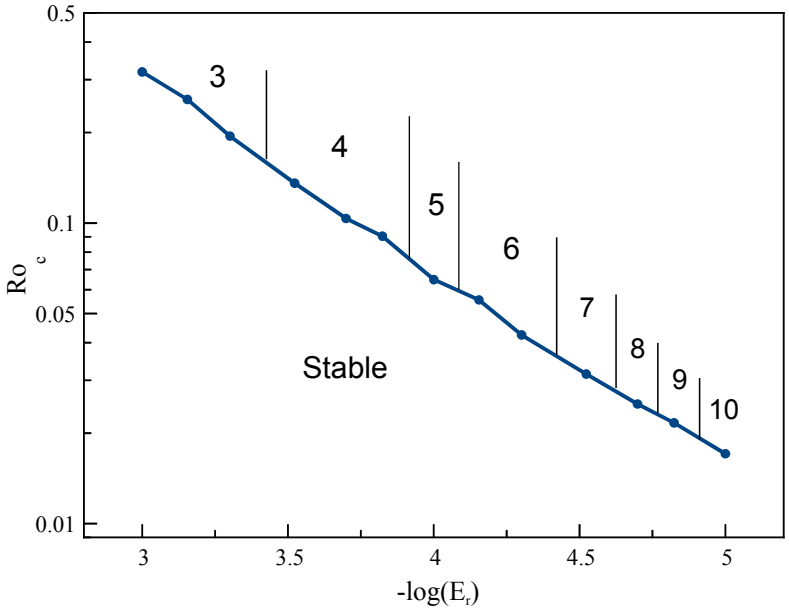

Figure 5.5: Instability Modes for $R_o/R_i = 5$

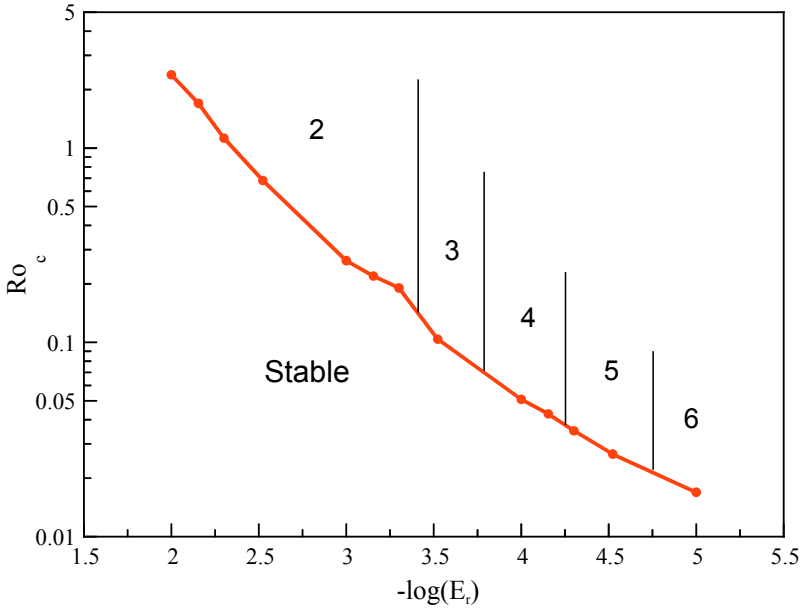

Figure 5.6: Instability Modes for $R_o/R_i = 10$

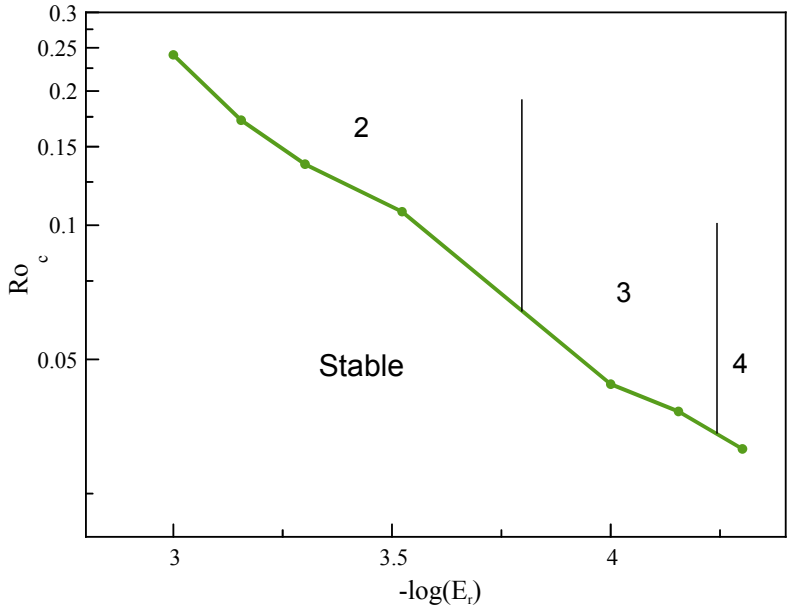

Figure 5.7: Instability Modes for $R_o/R_i = 20$

5.7 Conclusion

The angular velocity in the Taylor-Column, shown in figure 5.2, exhibits the classic result predicted by the Taylor-Proudman theorem. Below $E_r = 10^{-3}$, the angular velocity shows no vertical variation, except for the thin Ekman layers near the boundaries. The instability modes found numerically show the same asymmetry between positive and negative *Ro* as in the Hide and Titman [13] study, whose geometry it most closely resembles.

The critical Rossby number where the Taylor-Column first goes unstable has been found to have little dependence on the R_o/R_i. While the experiment has a much greater R_o/R_i than can be achieved numerically, a reasonable prediction of the expected critical *Ro* can be expected to be made from the simulations. As *m* is highly dependent on

the R_o/R_i, extrapolation to the experimental conditions is not possible.

The numerical simulation predicts $Ro_c \approx 0.2$ for the experimental runs, which is technically achievable. However, due to experimental limitations, the focus of the experimental work has shifted emphasis towards investigating the azimuthal velocity profiles in the Taylor-Column.

Chapter 6

Experimental Setup

This chapter contains a description of the setup used for the experiments. It is very closely linked with chapter 7, which describes the flow visualisation systems in more detail. As the rotating tank is a reusable system, it can be thought of as a "work-in-progress" indefinitely, where future users of the facility improve parts as technology progresses. For their benefit, some of the design decisions are covered, including suggestions on how the system can be improved.

A simplified drawing of the experimental setup used is shown in figure 6.1. It shows the location of the disc, and the primary Particle Image Velocimetry (PIV) systems mounted on the traverse. A second PIV system using a vertical lightsheet has also been used, but is not shown in the figure.

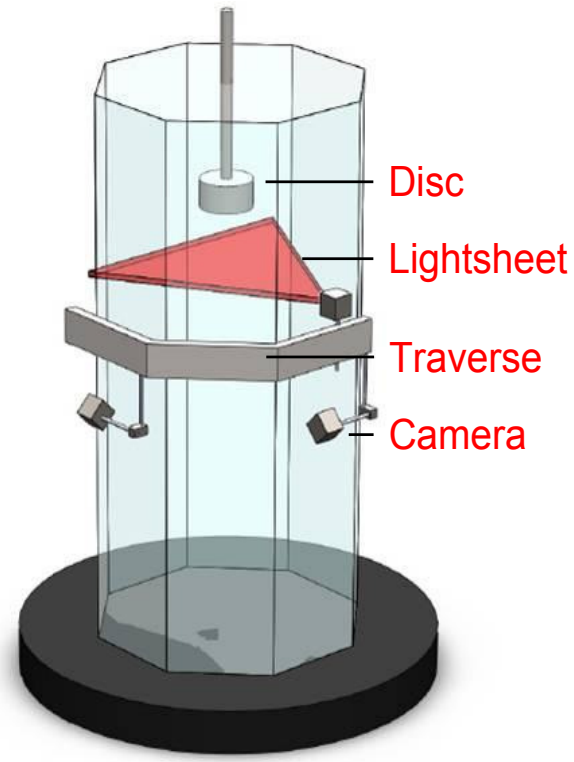

Figure 6.1: The experimental setup, showing the disc and one of the PIV systems on the traverse on the side of the tank.

6.1 Tank

Experiments have been performed on the large turntable at the University of Warwick, shown in figure 6.2. The apparatus was designed in-house and put into service in 2004, as a means to study the influence of background rotation on various flows. The first major studies were performed on Vortex Rings [6], and two short studies have been performed on the wake of a sphere [40] [43]. The glass tank is octagonal, as the flat surfaces simplify flow visualisation, and 2.5m high, with a 1m diameter. When completely filled, the tank holds approximately 2000 litres of water. The turntable is designed to run at a maximum rotation rate of 60RPM, but is currently limited to

20RPM due to the limitations of the motor. The apparatus was dismantled immediately after the final experiments were run as part of a wider refurbishment and is currently being rebuilt.

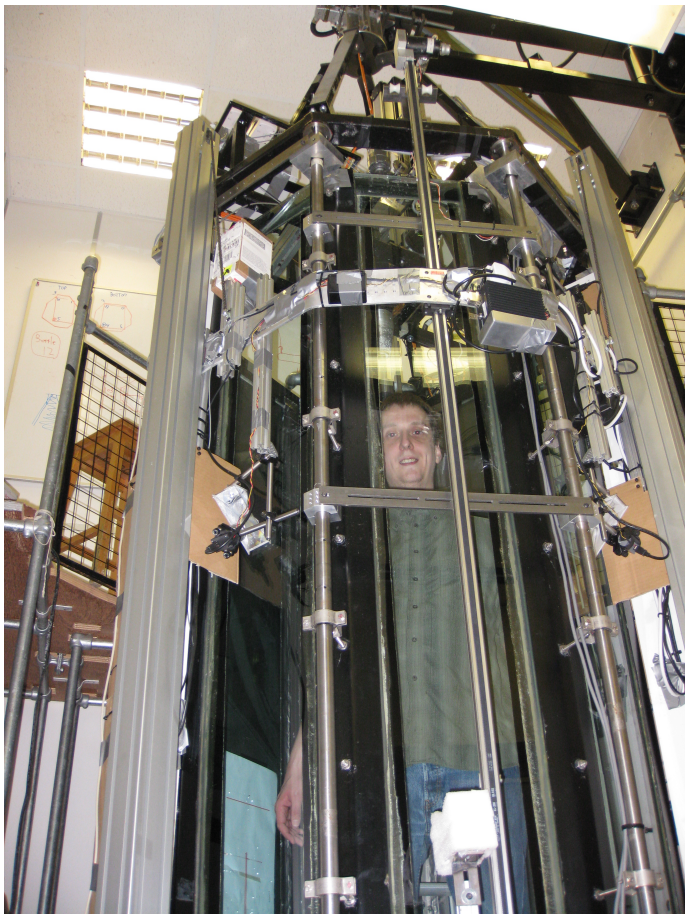

Figure 6.2: The large rotating tank.

Leakages of the tank were a problem during the initial experiments. The silicon sealant used to fill the gaps between the glass panels and the metal supports had strongly deteriorated over time, leading to several major leakages which potentially could damage the motor and control system, as well as posing a danger to other laboratories around it. After several unsuccessful attempts to repair the original seals, a full refurbishment

of the seals was carried out. The stronger materials used prevented further leaks from occurring.

The tank is rotated using a Bautz M714I 5kW servo motor, controlled by a Pacific Scientific SCE900 servo motor controller which provides constant angular velocity through a feedback loop. The motor is connected to the turntable via a 30:1 gearbox and 2:1 drive. During the first experimental runs at 5RPM tank rotation a large oscillation was found on the resulting vectorfields. It was determined that the rotation rate of the tank was not constant, and oscillated around 5RPM. This oscillation can be seen visually at very low rotation rates, such as 1RPM, where a very clear speeding up and slowing down can be observed.

As the oscillation of the tank has a well known amplitude and frequency, it is technically possible to subtract the oscillation from the resulting vectorfields. This does, however, increase the complexity of the processing significantly. More importantly, as the disc is rigidly attached to the tank, oscillating tank rotation will lead to an oscillatory forcing by the disc and the sidewalls, which may have a significant effect on the flow. During the previous study performed [6] on the apparatus rotation rates that are a multiple of 3 have been used successfully, these were tried instead and found to work well. The subsequent experiments run at 6, 9 and 12 RPM do not show any significant oscillation of the tank on the PIV results. In the experimental runs at 18RPM the oscillation is again strongly present, due to oscillations in the motor-controller.

During the 18RPM runs, the tank made an emergency stop due to overload of the mo-

tor. While the experimental series at 18RPM could successfully be completed, pushing the rotation rate of the tank higher to investigate if the rotational-stability returns has not been tried to prevent damage to the motor. A refurbishment of the apparatus is planned as part of the re-housing, which will include upgrading of the motor. It is recommended to include an assessment of the stability of the rotation as part of the recommissioning of the apparatus, using direct measurement methods such as using accelerometers, to allow quick optimisation of the motor control parameters.

6.2 Disc Assembly

A support system for the rotating disc has been added to the experimental setup. As the tank is a multi-functional platform, intended for many different experiments, an important design requirement is the ability to quickly install and remove the equipment, as well as not interfering with the existing experimental equipment.

Previous experimental work by Hide and Titman [13] and Früh and Read [9] has employed respectively a single disc immersed in the fluid and two discs at opposite ends of the vessel rotating in between solid walls. The single disc most closely matches the geometry used in the numerical simulation, and therefore has been chosen for the experiments.

Choosing the location of the disc is the second important design decision. If the fluid has a uniform density, gravity is balanced by a pressure gradient. The experiment is

thus independent of gravity. This means the disc can be either placed at the top or the bottom of the tank without any difference to be expected in the results. Locating the disc at the top of the tank has many technical advantages, as much fewer mechanical linkages are needed. Placing the disc at the top does not restrict access to and movement of operators inside the tank which is essential for cleaning purposes and installation of equipment inside of the tank.

Three discs have been manufactured for the experiment, with radii of 1.25cm, 2.5cm and 10cm and a height of 5cm. The discs, shown in figure 6.3 have been machined in-house out of aluminium.

Figure 6.3: The three discs manufactured for the project.

A support structure for the disc and electric motor has been designed, shown in figure

6.4. The motor is mounted on a solid metal plate which is attached to the existing frame on the top of the tank. The disc is mounted on a rotating shaft which is fed through the existing vortex ring generator assembly, and is held in place with three small screws. The disc sits approximately 50cm below the water-line when the tank is completely filled.

Dye-visualisation was expected to be an important flow visualisation technique at the time the system was designed, and a method of introducing dye directly into the Taylor Column has been implemented. A tube is fed through the hollow shaft from the disc to a rotary joint at the top, to which a tube to a dye-pump can be connected. The discs have a small hole drilled through the centre, allowing the injection of dye directly into the Taylor Column.

6.3 Motor

A 90W Parvalux PM3CMB-50VDC motor has been used to drive the disc. A 40:1 reduction gearbox is integrated into the motor, with an additional 20:1 reduction on the shaft to provide disc rotation rates between 1RPM and 6RPM. By reversing the polarity of the voltage the rotation direction can be changed.

A control system has been designed and implemented that allows remote adjustment of the rotation rate and rotation direction of the motor. A microcontroller-based system using a Bluetooth wireless link has been developed, utilising a simple terminal interface to change the rotation parameters. The Bluetooth link and terminal interface

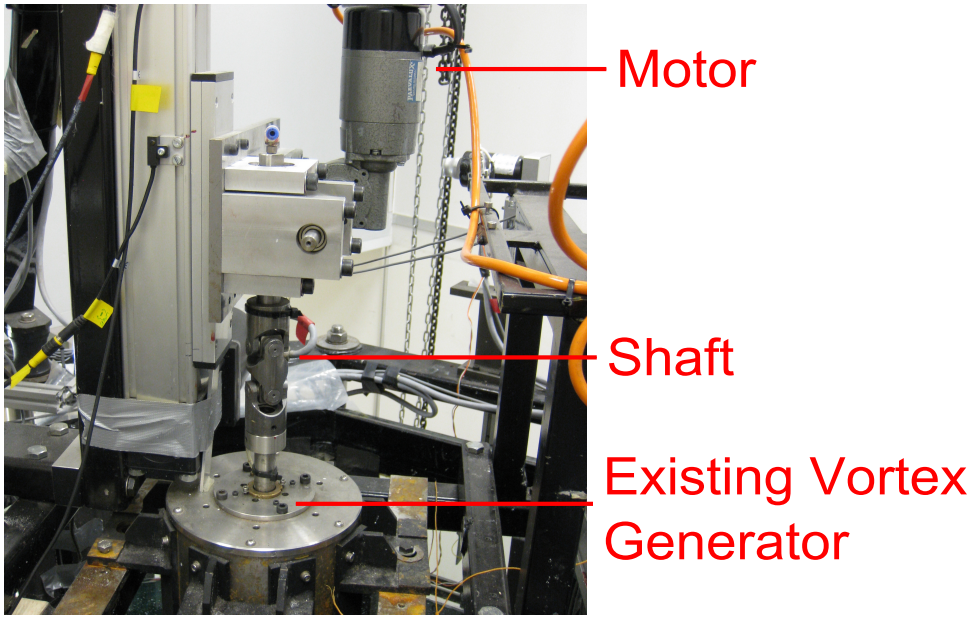

Figure 6.4: The DC motor driving the disc.

provide the flexibility required to be controlled manually from a computer off the tank during initial testing as well as the later fully automated control. The circuit diagram is included in appendix B.

The original prototype used Pulse Width Modulation (PWM) to modulate the motor directly, with an H-bridge to adjust rotation direction. PWM is a commonly used technique to control motors or other actuators with a pulsed digital output, which requires less complex circuits than changing the analog voltage directly [42]. The duty-cycle D is defined as

$$D = t_{on}/(t_{on} + t_{off}) = t_{on}/t_{period} \tag{6.1}$$

with t_{on} the time duration of the ”on”-state and t_{off} the time duration of the ”off”-

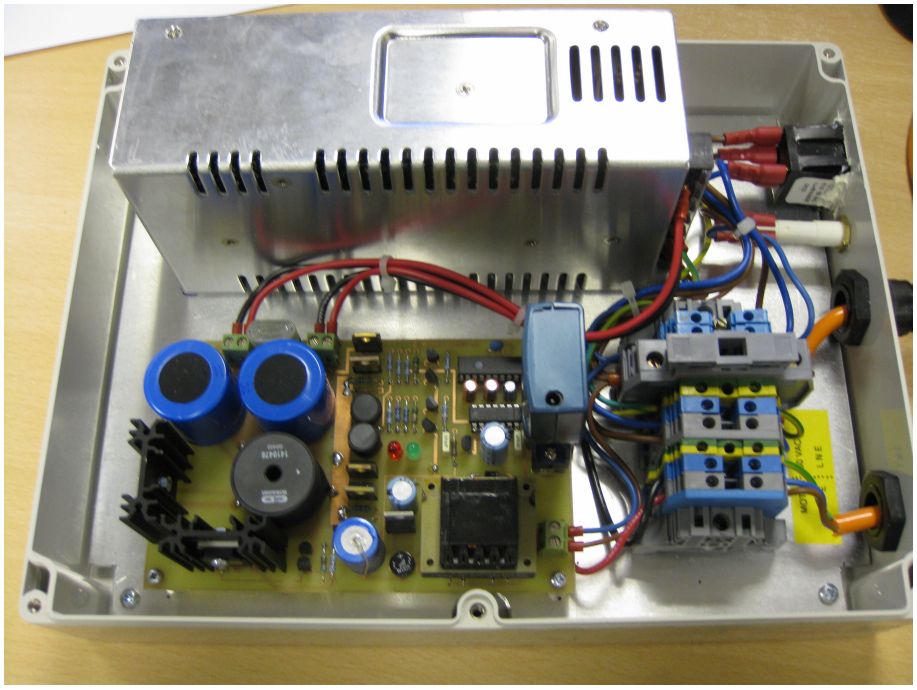

Figure 6.5: The wireless motor controller.

state. The PWM period t_{period} is the total cycle time, which is the inverse of the PWM frequency.

By varying the duty-cycle as shown in figure 6.6 the speed of the motor can be controlled. If the switching frequency is sufficiently high, the inertia and inductance of the motor will prevent any significant speeding-up and slowing down. The switching frequency used in the motor controllor is approximately 20kHz, which is also outside of the audible range to prevent acoustic noise from the motor and circuit.

While the setup using PWM worked, and provided a linear relationship between duty-cycle and angular velocity, a change in the power stage was implemented in the final model. Due to concerns expressed by technicians regarding the long-term suitability of the motor for PWM, it was decided to change the power input to the motor to a

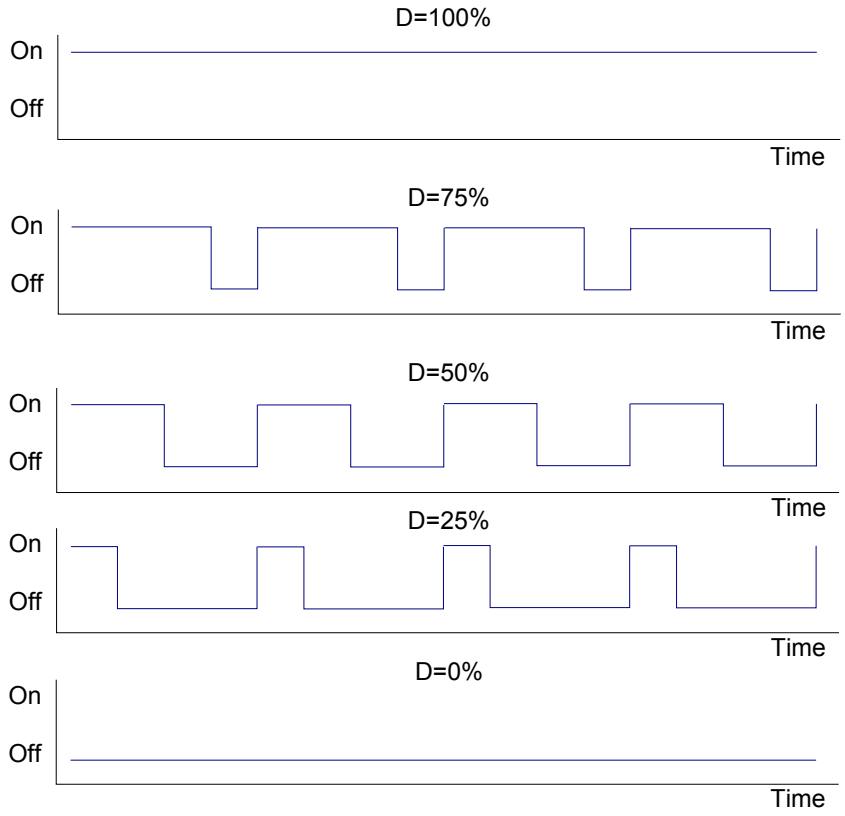

Figure 6.6: PWM changes the duration (width) of the ”on”-pulse to adjust the speed of the motor.

rudimentary switch-mode power supply controlled by the PWM output of the microcontroller. Later communication with the manufacturer of the motor proved the concerns about direct PWM of the motor unfounded, but the design was left unchanged. While the calibration curve is no longer linear and has less resolution at low rotation rates compared to direct PWM, this did not cause any serious problems as the final experiments were all conducted at high rotation speeds where the resolution actually improved. If higher low-end resolution is desired for future experiments, the original design can be implemented.

The rotation speed of the disc at a given setting was found to have small load depen-

dence and drift over time, as well as having a slightly different response at reverse rotation rates. To get a real-time measurement of the actual velocity, a chopper wheel was added on the shaft turning inside of a slotted optoswitch as shown in figure 6.7. As the motor-controller had already been completed, the measurement system is completely separate.

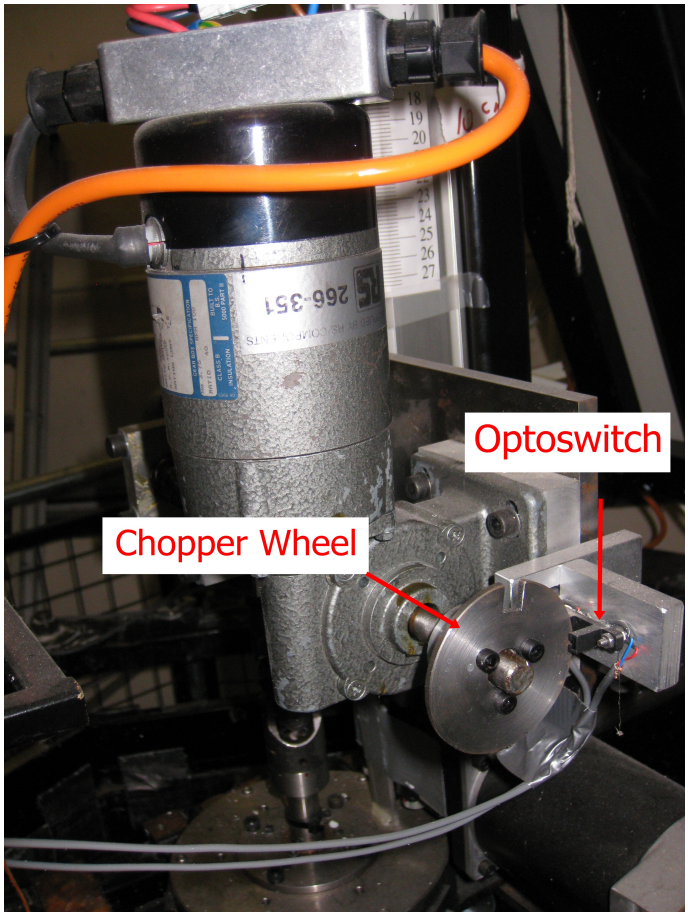

Figure 6.7: The chopper wheel and optical sensor allow measuring of the rotation rate of the disc.

The electronics for the rotation measurement system are shared with the temperature measurement system. The circuit diagram is shown in appendix B. The optoswitch

generates a pulse every time the hole in the chopper wheel passes through it. The signal from the optoswitch is debounced using a dedicated microcontroller, before being passed into the counter unit of the main microcontroller on the board. An interrupt routine on the main microcontroller, executed every 60.0s, saves the state of the counter, and, after a temperature conversion, sends the counter and temperature information over a serial cable to the control software running on the computer on the turntable which converts it into angular velocities. The design of the interrupt routine reduces the jitter in saving the state of the counter to a few microseconds. A water-proofing problem with the thermometers, which share the control circuit, caused short-circuits which caused angular velocity data to be missing for a very small number of the experiments. In these cases, the angular velocities from other measurement series have been used, which are sufficiently similar to not pose any problem in analysing the results.

6.4 End-Plates

An important difference in experimental geometry between the studies of Hide and Titman [13] and Früh and Read [9] is the location of the disc: flush with the wall, or immersed in the fluid. To investigate the effect of the solid boundary on the flow, a series of end-plates has been designed and manufactured. The end-plate is held in place using a Bosch frame attached to the tank superstructure as shown in figure 6.8. The gap-width between the disc and the plate is approximately 1mm.

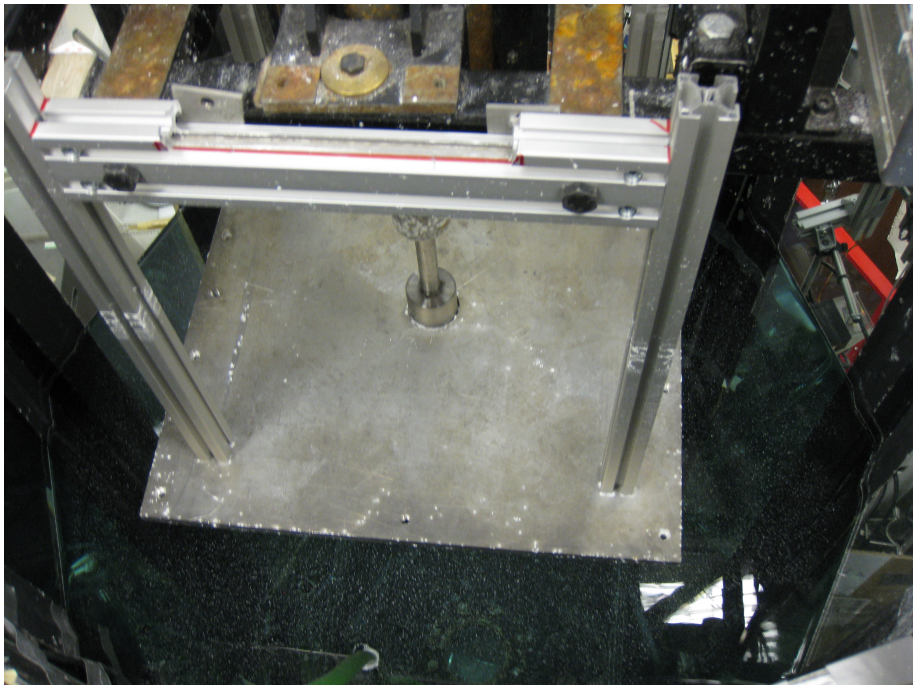

Figure 6.8: Top view of the solid end-wall around the disc

6.5 Traverse

The traverse, mounted on the side of the tank, supports both PIV systems as shown in figure 6.1 and 6.9. It uses a Nanotec 4H5618C0408 stepper motor, controlled by a Parker Zeta4 stepper controller. The traverse can normally be translated along the entire vertical extent of the tank, however, the components of the visualisation system limited the travel to 110cm, to prevent the cameras hitting the turntable.

Communication with the traverse is through the same 6K4 motor controller as the tank rotation, and is accessed using a simple serial interface. Only two commands are used during the experiment, the first setting the distance to be moved, the second the command to move. To reduce wear on the motor and belt, and, more importantly, to prevent

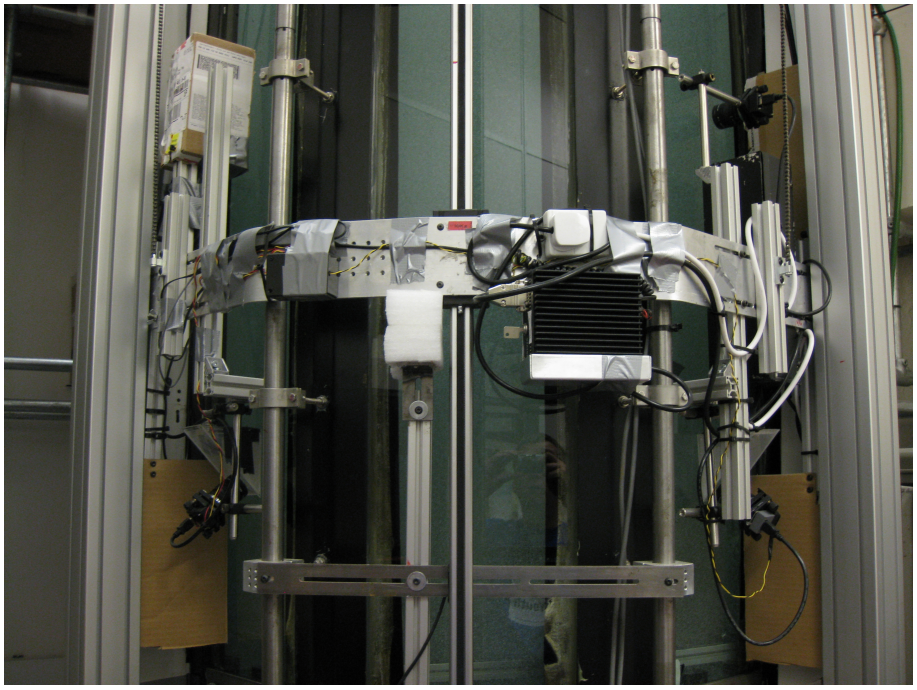

Figure 6.9: The traverse, containing the two lasers, three cameras and associated electronics of the two PIV systems. The long vertical aluminium structures on either side contain the counterweights.

excessive vibration causing misalignment in the PIV system, all traverse motions are limited to 1 cm/s.

The stepper motor powering the traverse is unable to support the weight of the approximately 15kg of equipment that was mounted on the traverse, making a counterweight necessary. A design based on the Minitec system [27] has been installed, which allows rapid design and installation using pre-fabricated parts. The two counterweights run inside two long hollow sections, which can be seen in figure 6.9 and 6.10 as the long vertical members, and are connected to the traverse via a chain and pulley system. Enclosing the counterweights eliminates the risk of them either swinging outwards due to the centrifugal force and hitting the scaffolding around the tank, or swinging inwards

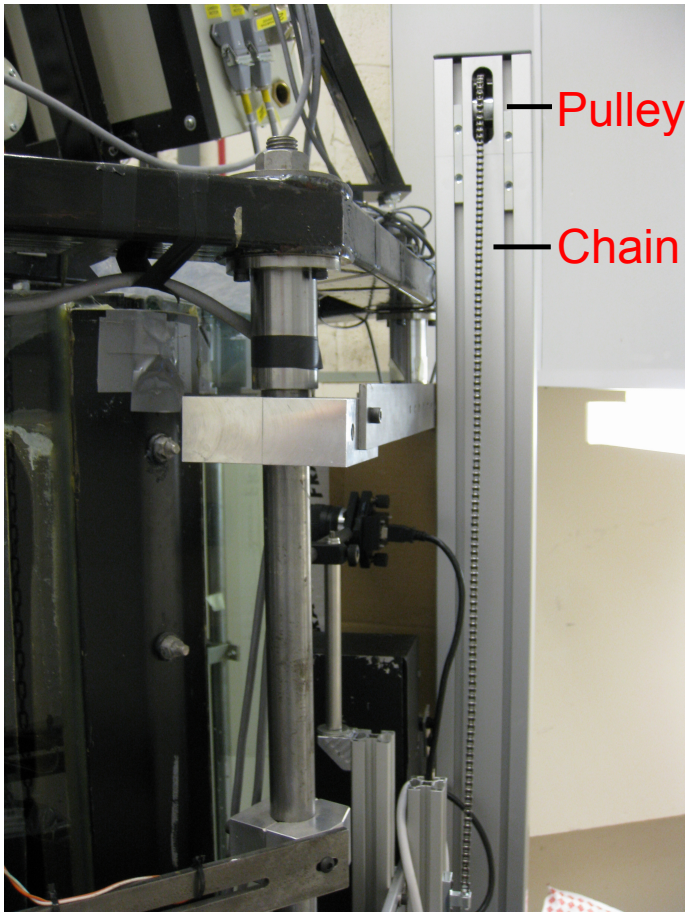

Figure 6.10: The chain and pulley system connects the traverse to the counterweights moving inside the vertical members.

and breaking the glass windows of the tank.

6.6 Temperature Measurement

Careful measurement of the temperature in the tank is important for several reasons. Before conducting any experiments, the water in the tank needs to reach room temperature. The water from the tap is around 10°C, significantly colder than the ambient

temperature of 22°C in the laboratory. The temperature of the water affects both its viscosity and density, with the density variation a possible cause of stratification which can significantly affect the experiments. Temperature variations can also cause convection currents to develop, which are a potential source of flow noise. To assess the temperature of the water in the tank and ambient air in the lab a number of digital thermometers are placed around the tank. Inside the tank, four thermometers are placed near the top at corners of the octagonal tank, and four near the bottom. Outside of the tank, only 2 are placed at both top and bottom at opposite ends of the tank, as these measurements are less important.

The Maxim-IC DS18x20 used for the temperature measurement are single-chip, digital thermometers with a 1-wire interface and measure the temperature with ± 0.5°C accuracy [25]. The integration of all signal-conditioning into the chip and the digital interface allows long cable lengths, with only 2 conductor cables needed as no separate power and data lines are needed due to the ability to operate on parasitic power. The thermometers are made waterproof by inserting them in a small metal tube and sealing of the ends with silicon, as shown in figure 6.11.

During the experiments, it was found that the temperature differences when filling the tank with cold water caused the silicon sealant to contract, allowing water to seep in along the wires. This corroded the contacts, which caused a short circuit between the data and ground pins, preventing data from being transmitted from any thermometer due to the shared bus. As during a temperature conversion the data line is connected directly to the 5V rail, the short circuit can cause the supply voltage to collapse causing the microcontroller to stall or reset depending on the duration. For nearly all exper-

Figure 6.11: One of the digital thermometers on the outside of the tank, inside its protective casing.

iments at least one thermometer at the top and the bottom produced valid data. The thermometers are to be replaced with higher accuracy models in the future, at which time the water-proofing issue will also be addressed.

Chapter 7

Flow Visualisation

Two, fully automated, traversable, Particle Image Velocimetry (PIV) systems have been developed to visualise the flow. This chapter describes the background of PIV, as well as the implementation on the experimental setup.

Previous work on the experimental facility has been performed using borrowed equipment [6], which was unavailable for the current study. In the long-term strategy for the experimental setup, a dedicated PIV system is essential for efficient use of the facility. The development has been a significant undertaking, and has required the significant amount of the time available for the project. The system has specifically been designed to be reusable, and as such offers important benefits to future users of the rotating tank.

7.1 Dye-visualisation

A small number of experiments with dye-visualisation have been performed, but were ultimately unsuccessful. Dye was injected into the Taylor-Column through a small hole in the disc. The flow inside the Taylor-Column is very slow, and dispersion of dye into the surrounding fluid before being transported around the Taylor-Column was found to be a problem. The mechanism for dye-transport is the meridional circulation, discussed in section 2.3, which has velocities in the order of mm/s. Especially for positive disc rotation this is a problem, as the dye is first spun outwards due to centrifugal forces close to the disc. Dye-visualisation has been abandoned at a very early stage, and PIV has been used as the only visualisation method throughout the study.

7.2 Particle Image Velocimetry

Particle Image Velocimetry (PIV) is a non-invasive quantitative method of flow visualisation, and has become one of the most widely used techniques in fluid dynamics in recent years. The earliest implementations in the 1980s relied on optical methods [1], but advances in computing and digital camera technology have made fully digital image evaluation techniques possible. Due to the much reduced complexity, digital PIV has practically fully replaced optical methods [2].

The traditional PIV-setup consists out of a single laser expanded into a lightsheet, illuminating seeding particles in the flow, with a single camera at right angles with the lightsheet as shown in figure 7.1.

The velocity vector is determined by calculating the particle displacement between

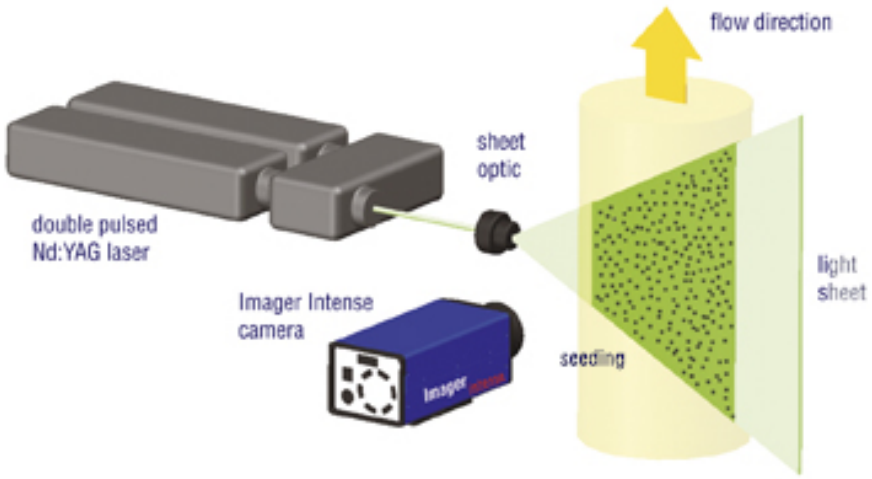

Figure 7.1: The traditional 2D2C PIV setup, a single laser illuminating a sheet of particles, with a single camera. Reproduced from [21]

two images. Depending on the camera setup, pairs are created automatically, or they are created from a sequence by combining frame i and $i + n$ into a pair as shown in figure 7.2. The number of frames n between the two images in a pair depends on the flow speed and shutter time of the camera. PIV is said to be time-resolved if the measurements are continuous, with a sufficiently high frame rate to capture transient phenomena.

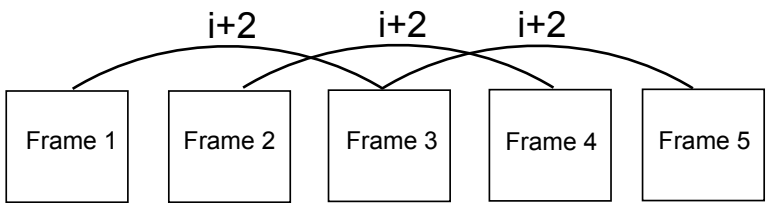

Figure 7.2: Image pairs can be created from a sequence of images.

7.2.1 Cross-Correlation

The particle displacement function d is found using cross-correlation of the image pair, by using

$$R_{II'}(x, y) = \sum_{i=-K}^{K} \sum_{j=-L}^{L} I(i, j)I'(i + x, j + y) \tag{7.1}$$

where I and I' are the intensity values obtained from the images, with I' being a larger window than I. I is shifted over the larger window I'. The cross-correlation has the highest value when the statistical degree of match between the two images is maximum. More efficient implementations of the algorithm exist, which are widely employed by PIV packages [32].

The size of the interrogation window, $N \times N$ pixels, determines the maximum particle displacement that can be obtained. The theoretical maximum, based on the Nyquist criterion is $N/2$, but a more conservative estimate is that the size should be chosen so that no displacement is greater than $N/4$ [19]. The window size must satisfy:

$$N = 4v_{max}d_{pixel}\Delta t \tag{7.2}$$

where v_{max} is the maximum velocity, d_{pixel} the pixel spacing and Δt the time between frames.

To upwardly extend the range of velocities that can be measured, either the interrogation window can be increased, or the image separation δt can be decreased. Increasing

the window size has the disadvantage of an increased spatial averaging, while decreasing the image separation may require increased laser power.

7.2.2 Imaging

The particles are imaged on the sensor of the camera as shown in figure 7.3. The displacement in the image, $d = x_i\prime - x_i$ is related to the real world displacement $D = X_i\prime - X_i$ as

$$x_i' - x_i = -M(D_X + D_Z\frac{x_i'}{z_0}) \tag{7.3}$$

$$y_i' - y_i = -M(D_Y + D_Z\frac{y_i'}{z_0}) \tag{7.4}$$

where M is the magnification of the optical system.

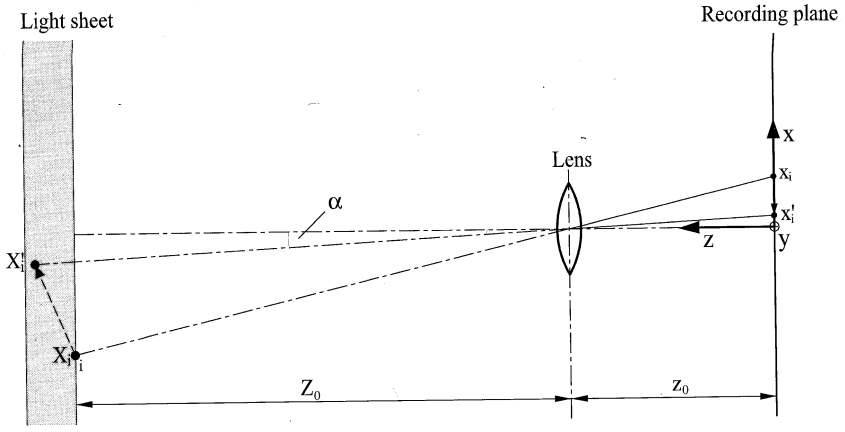

Figure 7.3: The imaging of a particle displacement on a digital camera. Reprinted from [32].

From these equations it can be seen that movement perpendicular to the lightsheet, D_Z, introduces an error in the measurement. Furthermore, if the optical axis of the camera

is not perpendicular to the lightsheet, this introduces a significant error even if no out-of-plane velocity exists. Both problems can be adequately resolved using a stereo-PIV system, as has been used in the present study.

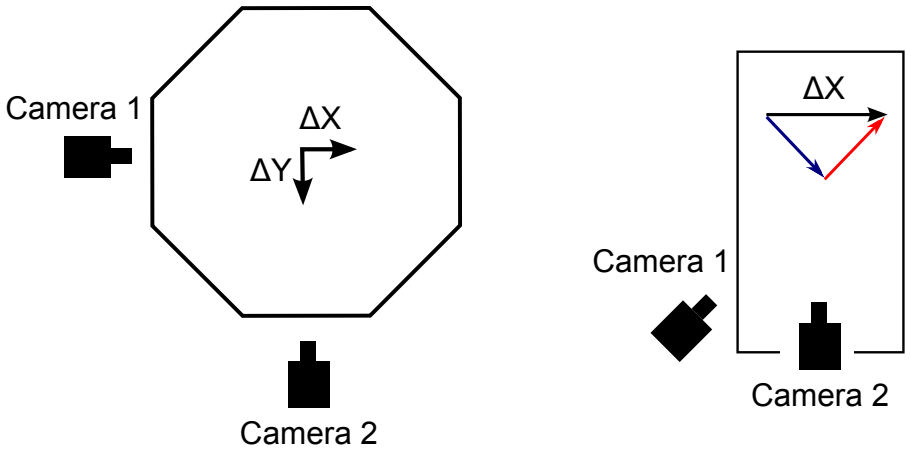

(a) Top View (b) Side View

Figure 7.4:
In (a) the top view of the two cameras in the stereo-PIV setup. In (b) the side view. The displacements observed by a single camera are ambiguous if an out-of-plane component is present, requiring a stereo-PIV system.

The origin of the error introduced by using a single camera which is not perpendicular to the lightsheet can be understood as follows. In figure 7.4, a displacement in the x direction is decomposed into components perpendicular (blue) and parallel (red) to the optical axis. Camera 1, on the left side of the tank, will see only the perpendicular component of the motion, the blue arrow. As the parallel component is not known, he new location of the particle could be anywhere on the red arrow. By using a second camera, perpendicular to the first, this ambiguity can be removed. Camera 2 can resolve the x-component directly without ambiguity. Combining the measurements of the two cameras, stereo-PIV, provides the x, y and z components without ambiguity.

A step in refractive index occurs between air and the water in the tank. According to Snell's law [12] light is refracted on an interface as

$$\sin\theta_2 = \frac{n_1}{n_2}\sin\theta_1 \tag{7.5}$$

in which each θ is the angle with the normal, and both n are the refractive indices of the media. If the refractive index change occurs at an angle that is not normal to the interface, distortion of the image will occur. Figure 7.5 shows the area imaged by a camera lens close to the wall of the tank. The blue rays show the undistorted image area, the red rays the area captured if the refraction of the water-air interface is taken into account. It can be seen that the length of d_1 is longer than d_2, which leads to distortion. This can be prevented using water filled prisms, which bring the angle at which the refractive index step occurs close enough to 90° to eliminate the effects of refraction.

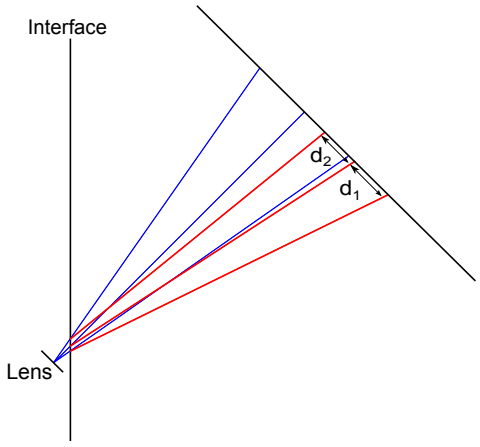

Figure 7.5: If the refractive index step does not occur at 90°, the image will be distorted.

If the optical axis of a camera is not perpendicular to the field of view, part of the image will be out-of-focus. This can be resolved by using the Scheimpflug principle [30], by tilting the lens relative to the camera as shown in figure 7.6. When all three red lines intersect in one point, the image will be in focus.

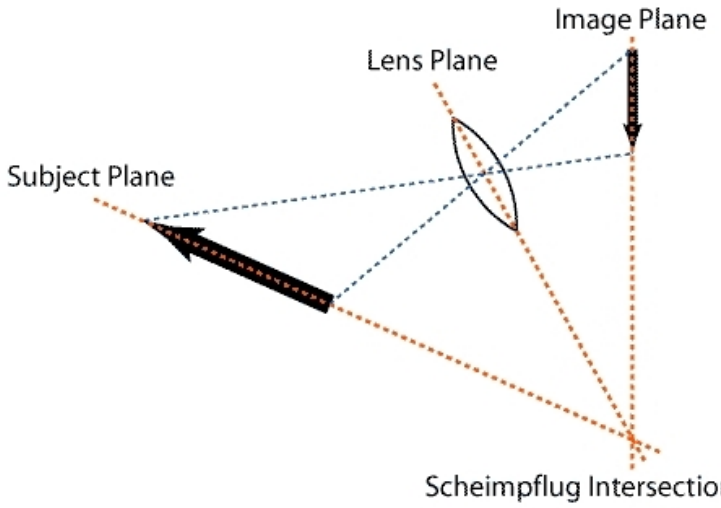

Figure 7.6: The Scheimpflug principle. Reprinted from [41].

7.2.3 Stereo-PIV

Stereo PIV is an extension of the basic PIV method, using two cameras to simultaneously record different views of the measurement plane. The images from both cameras are first correlated in the same way as in 2-component PIV. As the relative positions of the two cameras are known, the two vectorfields can be combined into a single 3-component vectorfield. This provides both the in-plane and out-of-plane components of the velocity in a single measurement [30]. For the experiments in the current investigation stereo-PIV has another, very important, advantage: it corrects for the ambiguity in the in-plane components introduced by the placing the cameras at 45° to the light-

sheet.

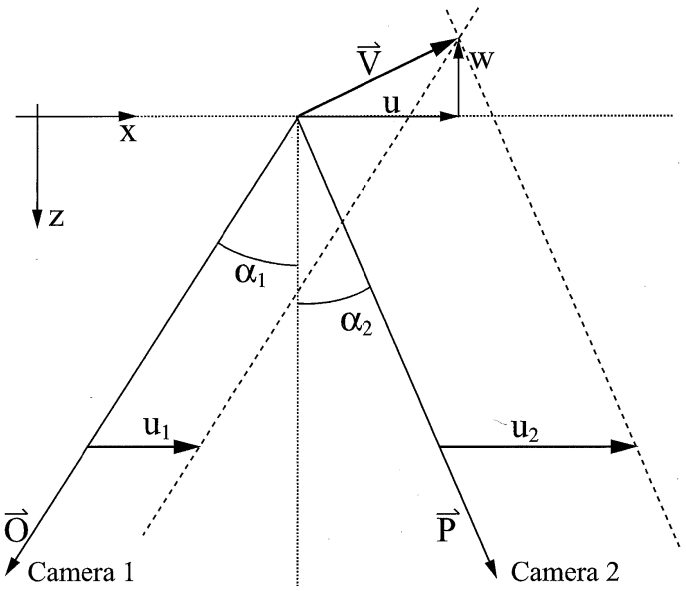

Figure 7.7: The imaging of a particle displacement on a stereo-PIV system. Reprinted from [32].

The principle of Stereo-PIV can be derived as follows [32]:

Starting with the basic equations for the mapping of particle displacements

$$x_i' - x_i = -M(D_X + D_Z \frac{x_i'}{z_0}) \tag{7.6}$$

$$y_i' - y_i = -M(D_Y + D_Z \frac{y_i'}{z_0}) \tag{7.7}$$

Then, define two angles α and β, which are the angles between the Z-axis and the ray from the particle through the lens to the recording plane in respectively the XZ-plane

and the YZ-plane. This is shown in figure 7.7.

$$\tan\alpha = \frac{x_i'}{z_0} \tag{7.8}$$

$$\tan\beta = \frac{y_i'}{z_0} \tag{7.9}$$

The velocities measured by camera 1 are then

$$U_1 = -\frac{x_i' - x_i}{M\delta t} \tag{7.10}$$

$$V_1 = -\frac{y_i' - y_i}{M\delta t} \tag{7.11}$$

For camera 2, the velocities can be determined in a similar manner. It is then possible to reconstruct U,V and W from the measured velocities. Assuming that both α and β are nonzero

$$U = \frac{U_1 \tan\alpha_2 + U_2 \tan\alpha_1}{\tan\alpha_1 + \tan\alpha_2} \tag{7.12}$$

$$V = \frac{V_1 \tan\beta_2 + V_2 \tan\beta_1}{\tan\beta_1 + \tan\beta_2} \tag{7.13}$$

$$W = \frac{U_1 - U_2}{\tan\alpha_1 + \tan\alpha_2} \tag{7.14}$$

$$W = \frac{V_1 - V_2}{\tan\beta_1 + \tan\beta_2} \tag{7.15}$$

This leads to an overdetermined system that can be solved using the least-squares method. Setting up matrices U_{meas}, V and A

$$\begin{bmatrix} U_1 & V_1 & U_2 & V_2 \end{bmatrix} = \begin{bmatrix} 1 & 0 & -\frac{O_x}{O_z} \\ 0 & 1 & -\frac{O_y}{O_z} \\ 1 & 0 & -\frac{P_x}{P_z} \\ 0 & 1 & -\frac{O_x}{O_z} \end{bmatrix} \cdot \begin{bmatrix} U & V & W \end{bmatrix} \tag{7.16}$$

$$\boldsymbol{U}_{meas} = \boldsymbol{A} \cdot \boldsymbol{V} \tag{7.17}$$

The velocity vector V can then be found using

$$\boldsymbol{V} = (\boldsymbol{A}^{\boldsymbol{T}} \cdot \boldsymbol{A}) \cdot \boldsymbol{A}^{\boldsymbol{T}} \boldsymbol{U}_{meas} \tag{7.18}$$

The residual of the least-squares method provides an indication of the quality of the measurement.

7.2.4 PIV-Hardware

Traditionally, PIV is performed using double pulsed Nd-YAG lasers [32]. With pulse durations in the order of nanoseconds and pulse separation in the order of microseconds, they are essential for high-speed flow visualisation. Nd-YAG lasers come at a

very high price, in the order of £20,000 at the time of writing for a 200mJ double pulsed laser with a repetition rate of 15Hz.

In recent years powerful, yet cheap, laser diodes have become available. As they are continuous wave lasers, they have some drawbacks for certain high-speed PIV applications, as the longer exposure time required may lead to streaking in the particle images. For low speed flows a relatively long exposure time is acceptable, and diode lasers can offer substantial cost-savings over traditional pulsed solutions in these applications. The velocities in the Taylor-Column are in the order of mm/s, and diode lasers are an attractive option.

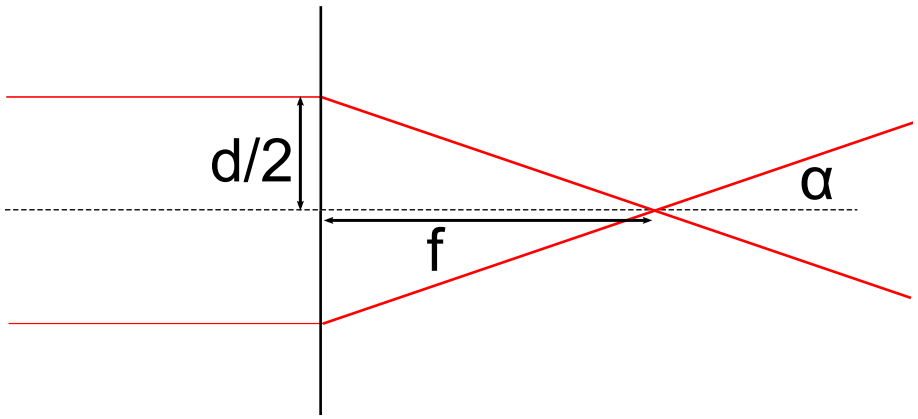

Figure 7.8: The fan angle of a cylindrical lens depends on the beam diameter and focal length.

The lightsheet is created by expanding the laser beam in one direction. Most common line generating lenses used for PIV are cylindrical lenses. The fan angle, α of the lightsheet is determined by the diameter d of the beam and the focal length f, as shown

in figure 7.8, and is given by

$$\alpha = \frac{d_{beam}}{2f} \tag{7.19}$$

with d_{beam} the diameter of the beam and f the focal length of the lens.

The lightsheet thickness should be such that sufficient particles are present in both images. This is determined by the out-of-plane velocity, and as a guide the lightsheet thickness δz should conform to [19]

$$w\Delta t/\delta z < 0.25. \tag{7.20}$$

7.2.5 Implementation of the PIV-Systems

Two PIV systems have been used to investigate the Taylor-Column: the primary is a stereo-PIV system with a horizontal lightsheet, the secondary is a standard system with a vertical lightsheet. Both PIV systems are time-resolved, owing to the very low flow velocities and low frame rates necessary to visualise the flow. Both PIV systems are mounted on the same traverse to allow data collection at a number of vertical positions without the need for recalibration.

7.2.6 Cameras

For the horizontal lightsheet, two cameras are positioned on the side of the tank, looking up at the lightsheet as shown in figure 6.1. The main advantage of this configuration is that by placing the cameras and lightsheet generating optics on the traverse, they can be moved together along the side of the tank, without requiring adjustment of the cameras or a full recalibration. The vertical lightsheet uses a single camera on the traverse.

Figure 7.9: The Scheimpflug mounts allow tilting the sensor relative to the lens, greatly improving the focus on the lightsheet.

Three Point Grey Firefly MV cameras have been used. The cameras can be synchronised, and support custom frame rates. Full control over the imaging parameters, such as gain and shutter speed is also an essential feature, as automatic algorithms for these settings may not work well in a PIV environment. The cameras come as bare circuit boards and have been mounted on a custom Scheimpflug mount as shown in figure 7.9. The cameras connect directly to the PC via Firewire, with both power and data on the same cable, and have a good Software Development Kit (SDK) available. The resolution of the Firefly camera is 640x480 in greyscale, and they accept standard c-mount lenses.

The cameras are controlled using custom made software written in Visual C++, which accepts simple command line inputs to specify the number of frames and the target directory. The software allows manual operation from a command-prompt in Windows, and is called from the main control-program during automated operation as described in section 7.2.12. To synchronise the cameras a very simple microcontroller circuit has been developed. It is powered by one of the cameras, and emits a 5Hz square wave. A change of frame-rate is achieved by a simple reprogramming of the microcontroller with new timings.

All cameras use 12.5mm Cosmicar lenses for the final experiments. This yields an effective area of interest of approximately 10cm by 10cm for both the horizontal and vertical lightsheets.

The positioning of the cameras restrict visualisation to a maximum distance of 110cm

from the disc.

7.2.7 Refractive Index Matching Prisms

To allow the cameras to take clear images while at 45 degrees to the tank, refractive index matching prisms need to be used. A pair of hollow 45 degree prisms have been made out of perspex and filled with water. They are mounted in front of the cameras, and are traversed together with the camera and lightsheet.

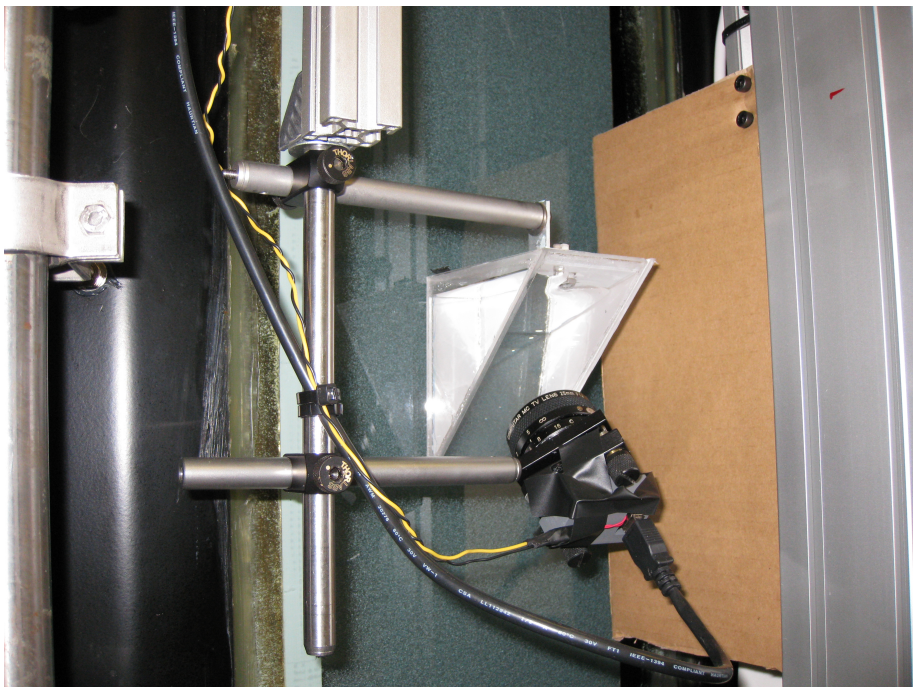

Figure 7.10: Perspex water filled refractive index matching prisms

The final incarnation of the prisms, shown in figure 7.10, have been made much larger than strictly necessary to simplify alignment, with the penalty of extra weight on the traverse. The sides of the prism are oversized to make them easier to seal. Tensol-12,

a chloroform based glue has been used to assemble the prisms, which creates a very thin waterproof seal which eliminated leakage problems. Accurate alignment of the prisms was found to be the most critical factor for image quality, with a much greater influence than the Scheimpflug adapter.

7.2.8 Lasers

Two diode lasers have been used to generate the lightsheet. The small size, low weight and high efficiency of the diode lases are important advantages compared to Nd-YAG lasers which tend to be bulky. The diode lasers are compact and light enough to be placed directly on the traverse. This removes the need for optical fibres, which significantly reduces complexity and cost.

The laser power required to image the particles without streaking depends on many factors. The flow velocity, the size of the area of interest, the type and density of seeding used, the distance the light travels through the seeded water, the losses encountered at interfaces between materials and the quality of the lightsheet optics all are important factors. Predicting the required laser power a priori is therefore difficult. The relationship between the shutter-time of the camera and light intensity is nearly linear, which allows testing with a cheap, weaker, laser to predict the power level needed before acquiring the final laser.

A 650nm red laser with a power rating of 200mW, costing less than £50, has been initially acquired. Testing showed the laser to be sufficiently powerful for the vertical

lightsheet to allow recording at 7.5Hz. For the horizontal lightsheet, a strong halo effect could be seen, which could be resolved by reducing the aperture size on the camera lens. The reduction in light intensity required a more powerful laser to be acquired.

A 655nm 1W red laser manufactured by CNI has been sourced for around £500 to generate the horizontal light sheet, with improved light sheet generating optics. The laser is shown in figure 7.11 inside the metal box designed to reduce unwanted reflections in the laboratory as well as providing a mount point to the traverse. The increased intensity of the light sheet is sufficient to provide clear images at 5 frames per second with a shutter time of 120ms.

The lightsheet is generated using a 50mm cylindrical lens. The lightsheet has some clear bright spots, but these proved not to be a problem in processing.

The 200mW laser is used to generate the vertical lightsheet, and forms the second PIV system together with another Firefly camera.

A control box has been made to switch the lasers on and off, using a microcontroller with a serial interface to the main control PC. A circuit diagram and source code are given in appendix B.3.

The 1W laser has an interlock input, which can be used as an on/off switch. The interlock input sources its own power, and is normally operated with a switch between

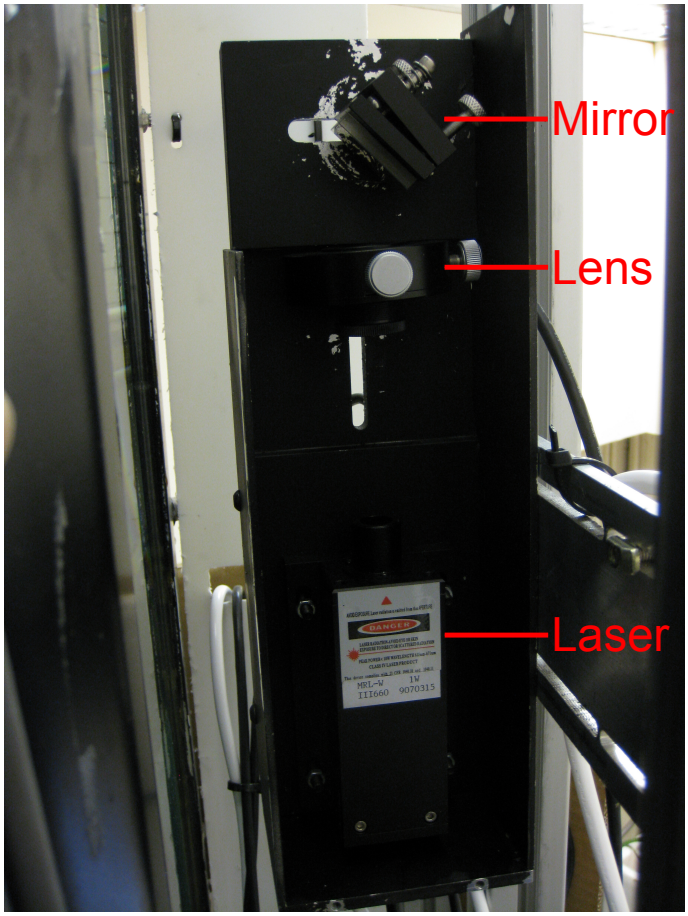

Figure 7.11: The 1W laser mounted on the traverse. The cylindrical lens generating the lightsheet is mounted in front of the laser, with a 45 degree mirror launching it into the tank.

two wires. To isolate the laser electrically from the control circuit, an FOD617 opto-isolator is used. When controlled through the interlock, the laser reaches full power nearly instantly when switched on. The very small leakage current of the opto-isolator when set to off caused the laser to emit a very weak, but visible, beam. This did not cause any problems during the experiments, but it is recommended to replace the opto-isolator with a relay in a future redesign to prevent unnecessary wear of the laser.

The 200mW laser is of a much simpler design, and does not offer an interlock input. The laser requires 5V to operate, which is supplied from the control circuit. The laser is controlled by a SUP75P03 P-channel MOSFET placed between the 5V supply and the laser, effectively used as a solid state switch operated by the control circuit.

7.2.9 Vertical Lightsheet

While the PIV-system using the horizontal lightsheet provides the vertical component of the flow, a second PIV system was implemented to get a direct visualisation of the meridional circulation. It also allows imaging the flow around the disc, which cannot be captured with the horizontal lightsheet. The vertical lightsheet PIV system is a simple single camera system. The system is constructed using a Firefly MV camera and a 200mW diode laser. Like the primary PIV system, it is mounted on the traverse allowing data-collection at different vertical positions. Due to the higher mounting of the laser and camera, it allows data collection only to 80cm below the disc. It does, unlike the primary PIV system, allow direct visualisation of the flow around the disc. In the later experimental runs the laser started to visibly dim, reaching the end of its expected 3000 hour operating lifetime, negatively influencing the image quality in these experiments. Not all experiments have therefore been run with the vertical lightsheet.

7.2.10 Seeding

The tank is seeded using Talisman-30 particles, which is a polymer normally used as a coating powder [29]. The specific gravity of the particles $\rho = 0.99 g/cm^3$, which is close enough to water to keep them suspended for several hours. The particle size is not uniform, and is specified by the supplier as less than $250\mu m$. These particles are low cost, even with the large quantity needed for the tank it is possible to discard them frequently. Before seeding the particles are shaken in a bottle half-filled with water with a small amount of laundry detergent to reduce the surface tension to reduce clumping. It is then added to the tank through a sieve to remove any remaining clumps.

To create an even distribution of particles, a Clarke CSE400A submersible pump has been used with a metal tube attached the outlet. Typically, the pump would be run for 1 minute with the tank rotating, and the tank was left to settle for 2 hours before starting any new experiments. When seeding the tank the pump is run continuously.

The particles require recirculation using the pump every 12 hours when newly put in the water. The particles deteriorate over time, reducing the window of "good quality seeding" to only a few hours due to excessive clustering. Particles have been replaced approximately every two weeks to ensure sufficient image quality.

7.2.11 Data Storage

The data storage requirements of the experiment are huge, and an efficient storage strategy is important. For the computer on the tank, two 500GB hard drives were purchased, the largest it could support. For long term storage, 6 external Western Digital MyBook 1TB USB2 drives were purchased. Copies of all data were kept on two separate hard drives in separate locations, to prevent data loss in the case of drive failure or theft. On the processing computer, 3 high performance internal 1TB Western Digital Black Edition drives were used as a working copy. For permanent storage, NTFS compression was used which reduced file sizes by about 65%.

A multitude of image file formats exists, with many different applications. For PIV, it is essential no information is lost, which rules out any lossy formats such as the ubiquitous JPEG format. The SDK for the cameras only support very few formats, and the only format that was supported by both the camera software and the PIV-software is uncompressed 24-bit BMP, which is inefficient but was used for simplicity.

The image files are first stored on the computer on the tank. Each experimental condition generates nearly 40GB of data, in batches of 600MB. The camera software first writes to a temporary file, which is split into individual images after completing the acquisition. This means every image is written twice, and read once. High disc performance is therefore essential to minimise the waiting time between acquisitions. This problem was compounded by the camera SDK used, which required temporary and final files to be in the same folder. This makes it impossible to use a fast drive for the temporary files, such as a RAM-drive, with a slower drive for the final split images.

Both off-tank storage via the wireless network and the external USB2 drives were found too slow to use as a temporary storage medium. The two internal 500GB IDE drives were alternated on the tank: once a drive was full, the tank rotation was stopped and the drive swapped for the other one. This method was found to be relatively quick, despite the extra time needed to spin up the fluid again.

7.2.12 Automation of the PIV systems

The time-scales involved in the experiments are long, with 8 hours needed to reach solid body rotation. Acquiring each dataset requires a large amount of simple steps, such as moving the traverse, creating storage folders and recording the temperature and disc rotation, with a potential for operator error. The combination of these two factors severely limits manual operation of the experiment. As all systems require a form of remote control due to safety reasons, full automation of the experiment is a logical step. An automated control system has been designed and implemented.

Nearly all functions on the tank can be automated, except for setting the tank rotation rate which must always be performed manually to ensure safety. With fully automated data acquisition only minimal user intervention is needed to keep the experiment running 24/7. This allows for much more efficient use of the experiment, and eliminates many causes of operator error. This frees up operator time to verify captured data, and to manage the data generated. It is estimated that automated operation allows four times as many experiments to be performed than is possible with manual operation.

The main control software is run on a relatively old computer with a 1GHz Pentium-3 processor and 512MB of RAM. It is placed on the turntable on the platform below the tank, and communicates with the individual control systems for different parts of the experiment, as well as with the cameras. The computer also holds the hard drive storing the recorded images. This computer is accessed using a wireless network and a "Remote Desktop". The components of the system are shown in figure 7.12

All control systems use RS-232 serial communications. The motor controller for the disc and the off-tank control system for the traverse are connected via a serial-over-Bluetooth wireless link. The motor and feedback are connected via the conventional serial port and a long cable. The laser control box is connected via a USB-to-serial connector, which due to a driver bug is only used to transmit data to the box.

The software to control the experiment is written in Visual C++ 2008, as a simple command line application, making extensive use of the serial communications functionality provided by the .Net framework to communicate with the remote devices. Most timing critical functions are processed on the microcontrollers, with only the long timescales handled by the control software using the realtime clock of the PC.

The SDK of the camera relies on the Microsoft Foundation Classes, and it was found to be difficult to fully integrate the camera software into the control program and was maintained as a fully separate program. Operationally this has one drawback, as it made it impossible to determine if the camera software had fully completed before continuing. The control software waits 90 seconds for the camera software to com-

plete, which is sufficient in normal circumstances. However, it was found in some exceptional cases that this was not long enough, and caused the camera software to crash because it was invoked more than once causing concurrency problems with the cameras. To optimise the waiting time for the camera software to complete, while still maintaining reliability, it is recommended to address this issue in a future version of the control software by either monitoring the process spawned or polling for the final file to be created.

The disc rotation-rate parameters for the runs are specified within the code itself, with a block of code specifying the conditions to run. Each parameter to be run consists out of a single line of code with a single function call, and as runs are completed these lines are commented out. When a new batch of experiments is set up it is necessary to recompile the code, but as this is a quick process this was not found to be a problem. While some user-friendliness can be gained by creating a GUI, the extra development time would not lead to any time savings running the experiment.

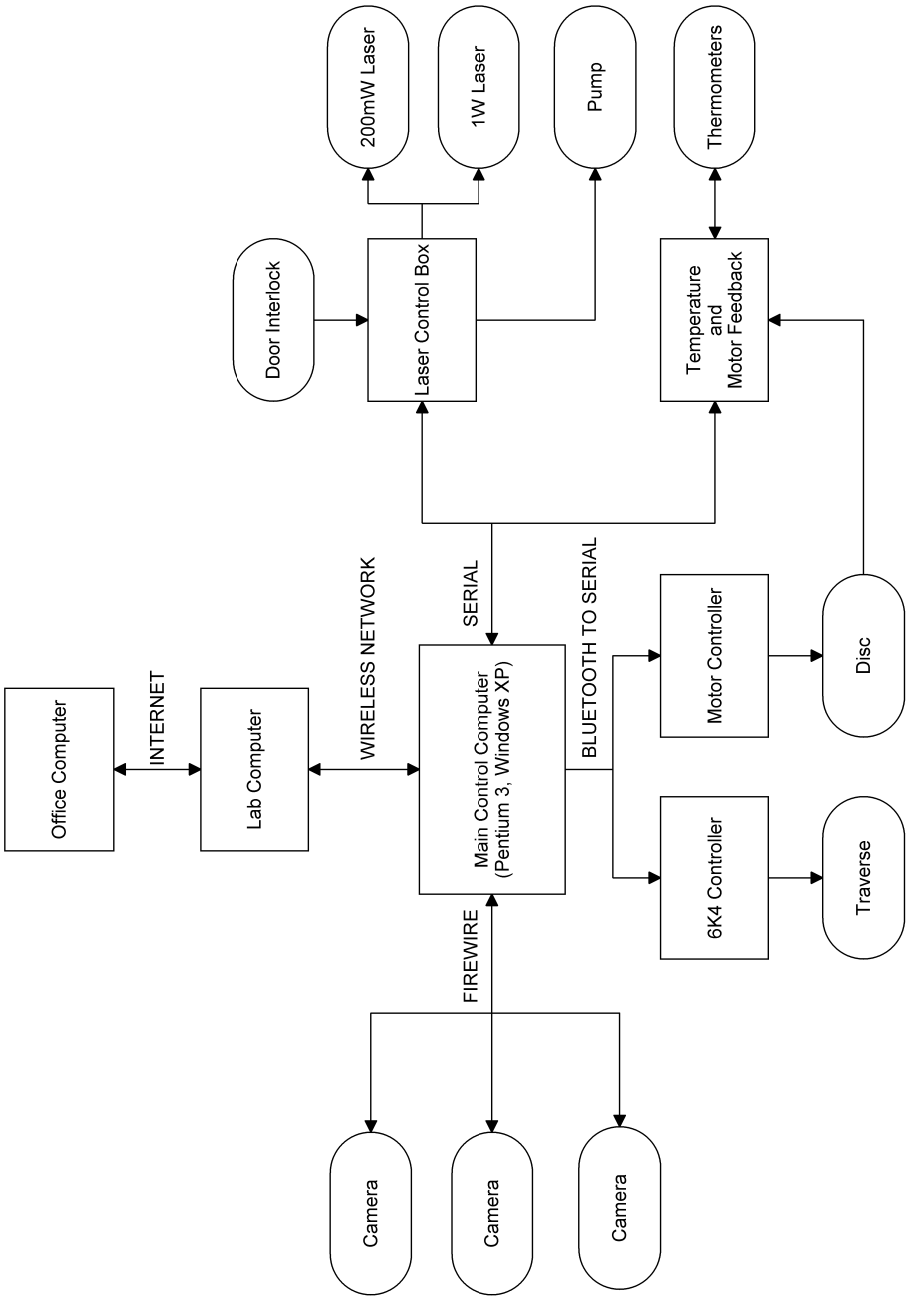

Figure 7.12: The components of the automated experiment.

Chapter 8

Experimental Conditions

The tank is filled using two hoses connected to taps in the laboratory. After filling, the water in the tank is allowed to reach room temperature, which takes around 2 days. After warming up, the seeding particles are added and the tank is spun up. The Ekman spinup time is given by [5]

$$t_e = d/(\nu\Omega)^{1/2} \tag{8.1}$$

which is in the order of 30 minutes for the experimental conditions.

Visual observations of the particle motion in the flow indicated a slightly longer spinup time was necessary than theoretically predicted. After about 2 hours, no particle motion could be observed in the rotating frame. To ensure solid body rotation has been achieved, the tank is spun up for a minimum of 8 hours before starting each experiment. The particles are pumped round to achieve a better distribution, after 1 minute of pumping the water is allowed to settle for 2 hours.

The disc is spun for 30 minutes before taking the first data to allow the Taylor-Column to settle. Starting at the top, data is then gathered at 23 heights at 5cm spacing, covering a little over half the length of the tank below the disc. At each position, the flow is 300 frames are recorded. The horizontal lightsheet is recorded first at 5fps after which the vertical lightsheet records at 7.5fps.

Two passes are made, to assess long term effects in the flow by measuring at the same position twice with 1 hour time difference. The top measurement position intentionally shines the horizontal lightsheet on the disc. While it is impossible to use the resulting images for PIV, it provides important information on the camera positioning. As the disc is a fixed reference point relative to the tank, any camera motion relative to the tank will show up in these images. It also allows verification of the rotation speed and direction of the disc.

All experiments have been performed fully automated. This allowed two measurement series of approximately 10 hours to be performed every day, each consisting out of 4 or 5 disc rotation rates, with short operator intervention required before each session to pump the particles round and set up the new parameters in the control software. This allowed all measurements to be performed in a relatively short time, with all the final experiments run from March until May 2010, after which the experimental setup was dismantled for a refurbishment.

8.1 Experimental Parameters

Experiments have been conducted at 3 tank rotation rates, of Ω = 6RPM, Ω = 9RPM and Ω = 12RPM and Ω = 18RPM. Only the disc with 2.5cm radius has been used due to time constraints, which has been rotated at 15 rotation rates between ω = 1RPM and ω = 6RPM, for both positive and negative disc rotation.

Chapter 9

Processing and Post-Processing

The experimental data is processed in DaVis, a state-of-the-art PIV package [21][34]. The Optical Engineering Group at the School of Engineering possesses several licenses for DaVis, and generously offered the use of one of their licenses to process the data. The resulting vectorfields are post-processed using Matlab, using the algorithms described in this chapter.

9.1 Data Selection

The processing of PIV data is very computationally intensive, and the availability of processor time is a significant limiting factor. A new, dedicated, PIV-processing machine has been built for this project with an Intel Core2Quad Q8300 2.5Ghz processor and 4GB of RAM, which alleviated this problem to some extent. The amount of data taken is much greater than can be processed in the available time. This provides max-

imum flexibility in analysing the data, but a selection of data to process needs to be made. Of the 23 heights measured, 21 positions can be processed as the top two have the disc obscuring part of the image. With 3+2 tank rotation rates (3 without and 2 with the end-wall in place), and 15 positive and 15 negative disc rotation rates, this corresponds to 3150 unique conditions. As each condition is measured twice, there are 6300 datasets of 298 vectorfields. With each dataset requiring a total processing time of over 1 hour, processing all data would require nearly a year even in ideal conditions.

Initially 6 vertical positions were processed for every single combination of disc and tank rotation rate measured. A vertical variation in the angular velocity was observed, which was a violation of the Taylor-Proudman theorem, and it was decided to process all vertical positions for a subset of the data to investigate this further. High noise levels were observed on the vectorfields, with the higher disc rotation speeds having substantially clearer Taylor-Columns. It was therefore decided to process all vertical positions of only the 5 highest disc rotation rates, at all tank rotation rates. This limits the amount of datasets to 2100, which was manageable in the time window the DaVis license was available. Further processing may be performed at a later date.

9.2 Calibration

A LaVision type 31 calibration plate, shown in figure 9.1, has been used to calibrate the cameras for the final experiments. The calibration plate is held against the disc and the traverse moved so the lightsheet is centered between the two layers of the calibra-

tion plate. The plate is illuminated using a 500W halogen bulb positioned underneath the bottom viewing window of the tank. A set of images is taken simultaneously from both cameras, to provide the base calibration. As the cameras are translated and rotated with the tank during the experiment, a further self-calibration is performed in DaVis.

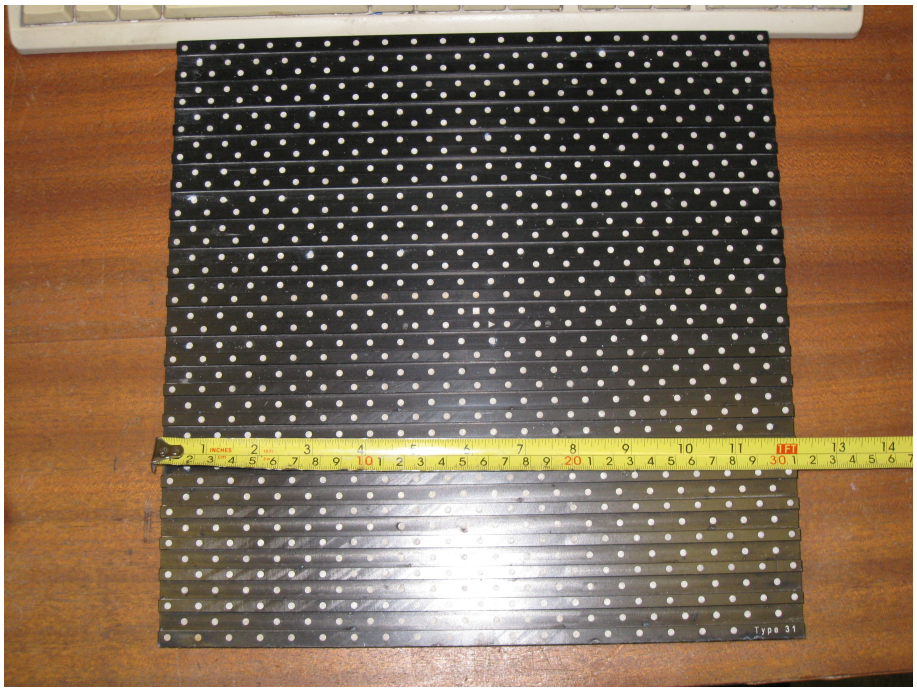

Figure 9.1: The LaVision Type 31 calibration plate

In principle, self-calibration needs to be performed after each movement of the camera. As the cameras rotate together with the tank, there is potentially a continual small relative movement of the cameras, which would introduce errors in the calibration. This movement, however is small, and can effectively be ignored. Moving the traverse up and down has a more significant effect, and for every vertical position within a dataset a separate self-calibration is performed, as the traverse may move inward or outward slightly. The traverse positioning was found to be sufficiently accurate to only

require a single self-calibration per height per tank rotation rate. As it is impossible in Davis 7.22, the latest version available at the time, to include a self calibration in an automated batch run, the reduction in the required number of calibrations was important, as it reduced the necessity of operator intervention to once every 12 hours, rather than once every hour.

9.2.1 PIV settings

Image pairs for cross-correlation are created from frames i and $i + 2$, corresponding to a temporal separation of 400ms. A separation of a single frame did not produce accurate results, due to the long exposure time of the cameras of 150ms, compared to the time between sucessive frames of 200ms. Increasing the separation above 2 frames did, however, not further improve the results.

The vectorfields are computed using multi-passes, the 1 pass at a window size of $32x32$ pixels and 3 passes at $12x12$ pixels with 25% overlap, using the standard FFT correlation function. For the final pass, Whittaker reconstruction is used to provide better sub-pixel accuracy [23].

9.3 Post-Processing

The data is post-processed using Matlab. The vectorfields are imported into Matlab using the ReadIMX toolbox provided by LaVision. The algorithms used in post-processing are described below.

9.3.1 Centre Finding Algorithm

Due to the lightsheet and camera configuration the centre of the tank is no longer defined in the camera frame, as no fixed reference point exists, and has to be determined from the flowfield. More importantly, it was observed that the centre of the Taylor-Column is not stationary, which makes an automated centre finding algorithm essential due to the large amount of vectorfields to be processed. An algorithm developed by Michard [10] has been used, which proved very robust.

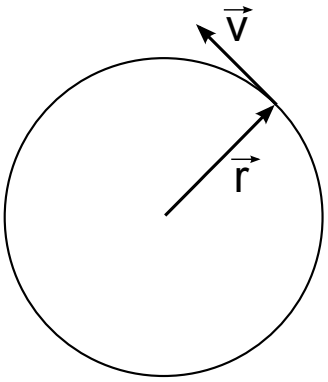

Figure 9.2: The angle between the position vector r and the velocity vector v is close to 90° if the centre is correctly defined.

In a circular vortex, the angle between the position vector r from the centre and the velocity vector v is 90°, and $|sin(\alpha)| = 1$, as shown in figure 9.2. By stepping over the measurement domain trying every possible position for the centre of the vortex, summing $|sin(\alpha)|$ in a box around it, and determining the maximum sum the centre can be found. The algorithm implements this as follows:

With P a fixed point in the measurement domain, a dimensionless scalar $\Gamma_1(P)$ is de-

fined as

$$\Gamma_1(P) = \frac{1}{S}\int_{M\epsilon S} \frac{PM \times U_M \cdot z}{\parallel PM \parallel \cdot \parallel U_M \parallel} dS = \frac{1}{S}\int_S sin(\theta_M) dS \tag{9.1}$$

with S a two dimensional area surrounding P. M lies in S, z is the unit vector normal to the measurement plane and θ_M is the angle between the radius vector PM and the velocity vector U_m.

If the vortex is axisymmetrical, the function will reach its maximum of $|\Gamma| = 1$ at when P is at the centre of the vortex. For PIV data, the velocity field is discretised onto a grid, and the function can be approximated on a rectangular domain S, which is centered on P.

$$\Gamma_1(P) = \frac{1}{N}\sum_S \frac{PM \times U_M \cdot z}{\parallel PM \parallel \cdot \parallel U_M \parallel} dS = \frac{1}{S}\sum_S sin(\theta_M) dS \tag{9.2}$$

The discretised function is then stepped over all possible locations of the Taylor-Column centre. The gridpoint where the function has its peak is returned as the centre.

The unoptimised versions of the algorithm is very time-consuming to run in Matlab, requiring approximately 40 minutes per dataset of 298 vectorfields. The algorithm has been re-coded in C++ and compiled to a Matlab MEX function using the Intel C++ compiler, reducing the execution time to only several seconds.

9.3.2 Azimuthal and Angular Velocity Profiles

The azimuthal velocity profiles are created by converting the velocity to the radial component v_r and azimuthal component v_θ, as shown in figure 9.3. The angular velocity profiles are created from the azimuthal velocity profiles by dividing by $2\pi r$. The accuracy near to the centre of the Taylor-Column suffers more greatly than with the azimuthal velocity profiles, as dividing by a small radius magnifies the error.

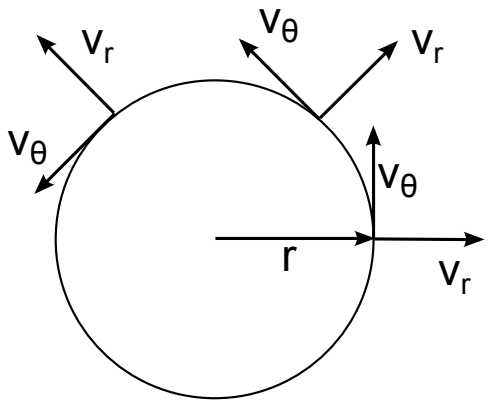

Figure 9.3: The velocity field is converted to radial and azimuthal components

9.3.3 Radius Finding Algorithm

The radius of the Taylor-Column is determined by finding the maximum azimuthal velocity along the edge. To improve the accuracy of the algorithm in noisy datasets, the median value is taken of the entire dataset.

9.3.4 Instability Modes

The instability of the Taylor-Column manifests itself as a series of waves superposed on the Taylor-Column, as shown in Hide and Titman's [13] results in figure 3.1. The resolution of the vectorfields obtained using PIV is insufficiently high to directly observe the vortices. However, the mode number can be determined computing the Fast-Fourier-Transform (FFT) of the azimuthal velocity around the edge of the Taylor-Column. The vectorfield converted to polar coordinates is used, with the edge of the Taylor-Column defined by the results of the radius finding algorithm. The FFT is performed on the azimuthal component along the edge of the Taylor-Column, with the magnitudes in the FFT summed over the entire one-minute long dataset. The dominant modes are defined as the modes that have at least 80% of the magnitude of the most unstable mode.

9.3.5 Matlab GUI

The algorithms to determine the centre and radius are not completely immune to noise, or indeed the absence of a Taylor-Column altogether. It is common for spurious vortices to appear in a vectorfield, with similar angular velocities as the Taylor-Column, making it impossible for the algorithms to distinguish between them reliably. A visual inspection of a small number of the vectorfields in each set has been determined as the most reliable method of determining the quality of the dataset. To reduce the significant amount of time necessary to inspect the datasets, a Matlab program with a GUI (Graphical User Interface) has been created. The GUI, shown in figure 9.4, displays a sequence of 7 vectorfields and the results of the centre-finding, radius-finding and

FFT algorithms to allow a quick assessment if the data is of good quality. If necessary, the centre-finding algorithm can be rerun with different parameters before accepting or rejecting the data.

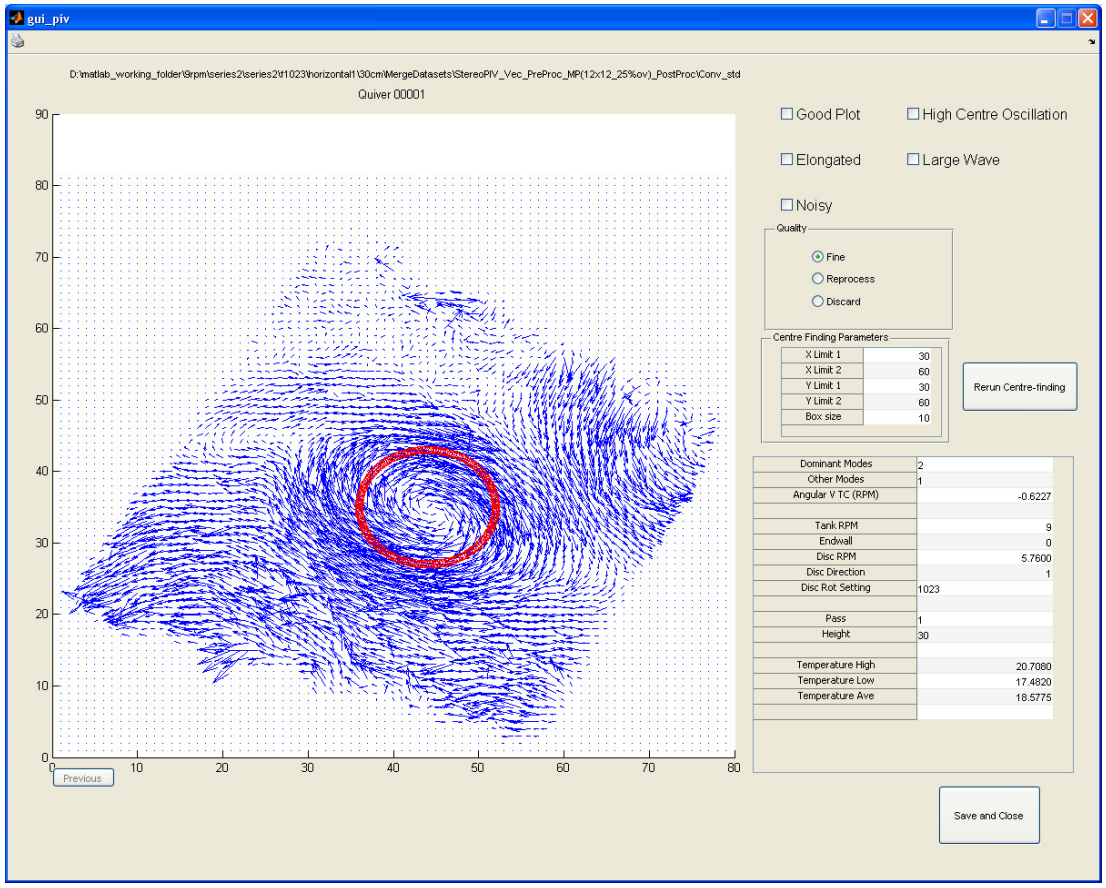

Figure 9.4: The GUI allows quick assessment of dataset quality.

Chapter 10

Results

A careful selection of the data was necessary to ensure accuracy, due to noise on the data. Despite this, consistent results have been obtained for the azimuthal velocity in the Taylor-Column.

10.1 Flow Noise

The experimental data is very noisy, and in some datasets no Taylor-Column can be observed at all. In other datasets, waves, jets or spurious vortices can be observed in addition to the Taylor-Column. These motions can also be observed visually in the raw particle images of both cameras. The noise is a feature of the flow itself, rather than an error introduced by the measurement system or by processing.

An example of flow noise can be seen vectorfields in figures 10.1, 10.2 and 10.3. The

Taylor-Column is expected to be continuous, but the measured data does not reflect this. Three instantaneous vectorfields are shown, taken from sequential datasets, taken only a few minutes apart and at a small vertical spacing. In 10.1, taken at 85cm, a very clear Taylor-Column can be seen, while in figure 10.2, which is taken only 5cm lower and 2 minutes later, no Taylor-Column can be seen. In figure 10.3, at 95cm, the Taylor-Column reappears, although it is more noisy than before. While the vectorfields shown are instantaneous, they are representative of their entire respective dataset of 298 vectorfields taken in 60 seconds.

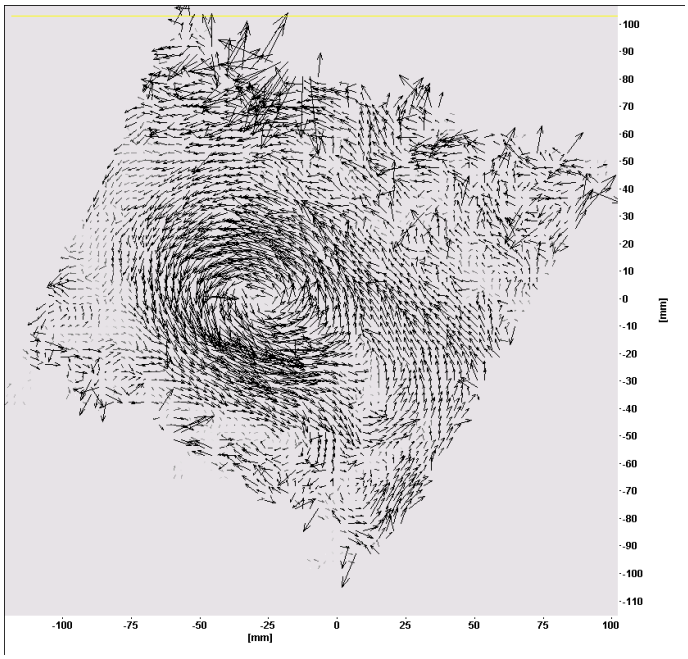

Figure 10.1: At 85cm a clear Taylor-Column can be seen.

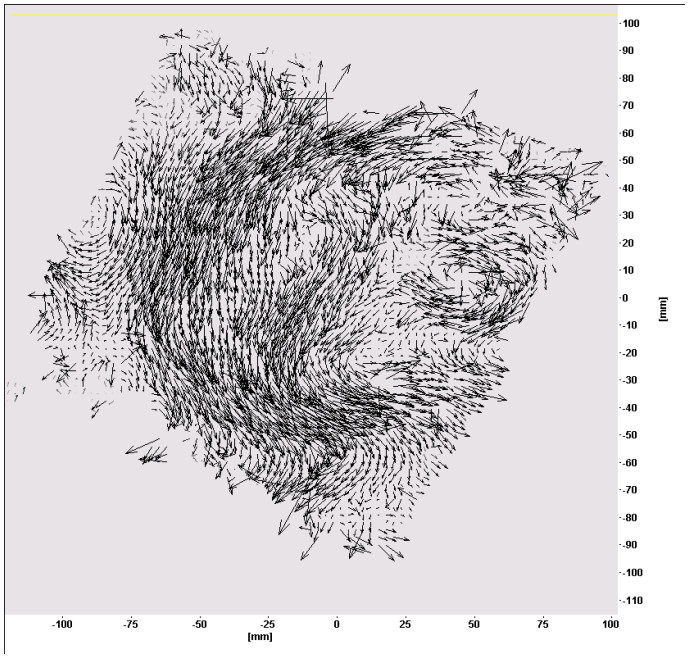

Figure 10.2: At 90cm no Taylor-Column is visible.

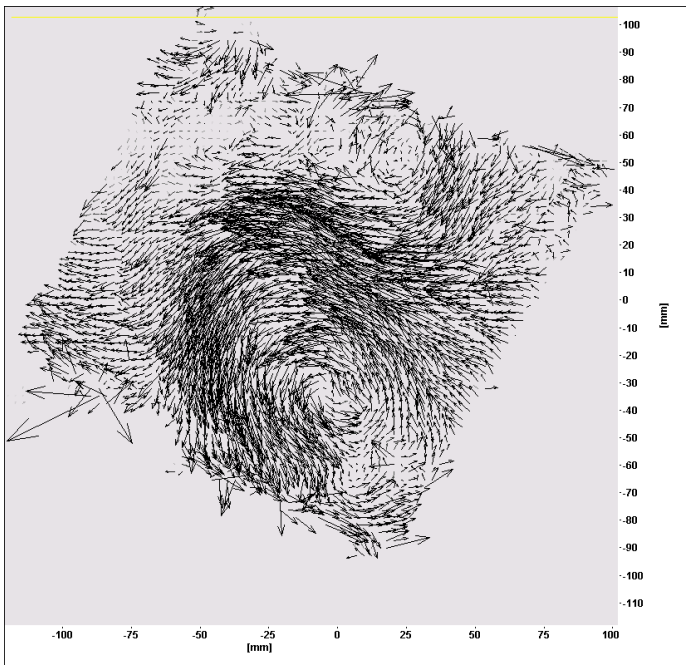

Figure 10.3: At 95cm the Taylor-Column reappears, but is more noisy.

All the datasets have therefore been assessed for the presence of the Taylor-Column, and have been discarded if the Taylor-Column is not present or the noise obscures it completely. In total, over 80% of the datasets processed have been discarded. The end-wall appears to significantly increase the noise, with only the data at Ω = 9RPM tank rotation and $\omega = -6.2$RPM producing valid data. This suggests tank vibration could play a role, with the large plate coupling noise into the fluid.

10.2 Azimuthal and Angular Velocity

Profiles of the azimuthal velocity have been obtained for 31 combinations of tank and disc rotation rates. Of these profiles, 13 extend the full 110cm from the disc with the other 18 only partial. For 49 combinations of disc and tank rotation the signal-to-noise ratio of the data obtained was too poor to observe the Taylor-Column at sufficient heights, and these conditions have been discarded. The most stable tank rotation rate appears to be Ω = 9RPM.

The full azimuthal and angular velocity profiles of a run at Ω = 9RPM and ω = 5.79RPM are shown in figures 10.4 and 10.5, which is a typical flow field for $+Ro$.

Figure 10.4 shows that the highest azimuthal velocity occurs near the edge of the Taylor-Column, with the highest angular velocity occurring near the centre of the tank. The radius of the Taylor-Column is in the order of 1.5 times the radius of the disc, for both positive and negative Ro. The angular velocities in the Taylor-Column near to the disc and in the centre of the tank are in the order of 0.3ω.

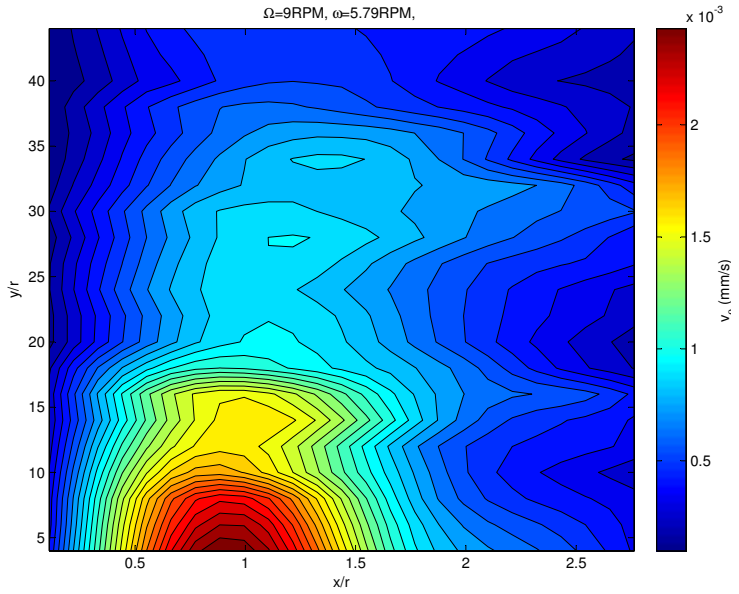

Figure 10.4: Contours of the azimuthal velocity for Ω = 9RPM and ω = 5.79RPM.

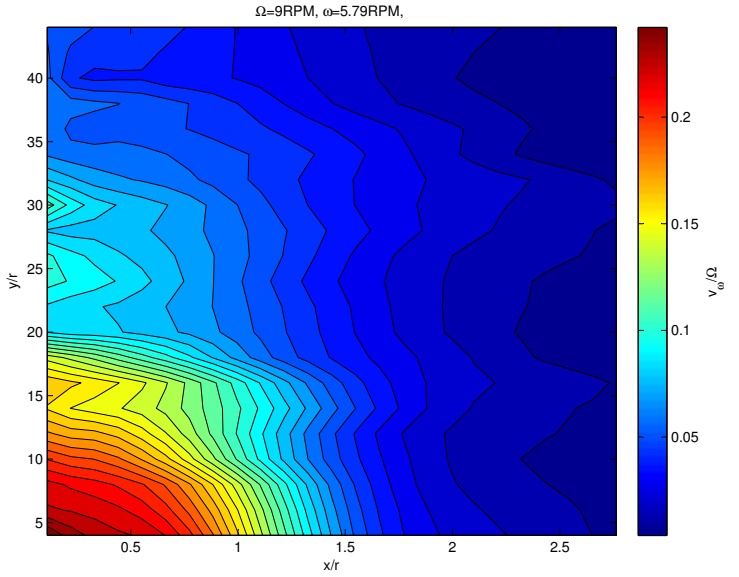

Figure 10.5: Contours of the angular velocity for Ω = 9RPM and ω = 5.79RPM.

Care should be taken, however, interpreting the angular velocity plots. Near to the centre of the Taylor-Column, the uncertainty in determining the angular velocity is expected to be higher due to the small radius. The azimuthal velocity is therefore more reliable when comparing different experimental conditions, especially when close to the centre.

10.2.1 Positive Ro

To investigate the vertical dependence of the azimuthal velocity, plots of the maximum azimuthal velocity at each height are created. The azimuthal velocity is non-dimensionalised by the velocity of the rim of the disc, with $v_{rim} = 2\pi r\omega$. In figure 10.6 at the end of this section the results for $\Omega = 9$RPM are shown. A clear decay of the azimuthal velocity can be observed for all disc rotation rates, which is close to linear until $h/r = 25$.

The radial dependence of the azimuthal velocity is shown in figure 10.7 for $Ro = 0.64$. The peak azimuthal velocity is reached close to $x/r = 1$ for all heights, moving outwards slightly at greater distances from the disc. A steady decay in velocity at increasing distance from the disc can also be observed.

The angular velocity is shown in figure 10.8, for $Ro = 0.64$, created from the raw azimuthal velocities from figure 10.7. A clear decay of the angular velocity in the Taylor-Column ω_{tc} can be seen at increasing radial distance from the centre, indicating a very thick shear-layer.

Figure 10.9 shows the maximal azimuthal velocities at $\Omega = 6$RPM. The azimuthal velocity again decays with increasing distance to the disc. The maximum velocities

attained in the Taylor-Column are lower than at Ω = 9RPM.

The radial dependence of the azimuthal velocity is shown in figure 10.10 for Ω = 6RPM and Ro = 0.87. The peak azimuthal velocity is again reached close to $x/r = 1$, but does not move outward at increasing distance from the disc as with Ω = 9RPM.

At 12RPM, shown in figure 10.11, only two disc rotation rates produced valid data due to the much greater amount of flow noise present. A small decay in azimuthal velocity is observed for Ro = 0.49RPM, while at Ro = 0.48RPM the azimuthal velocity increases sharply between 45cm and 70cm from the disc. No clear cause for this increase can be identified from the vectorfields.

The radial dependence of the azimuthal velocity at Ω = 12RPM and Ro = 0.48 are shown in figure 10.12. The peak in azimuthal velocity moves outwards at increasing distance from the Taylor-Column, similar to Ω = 9RPM.

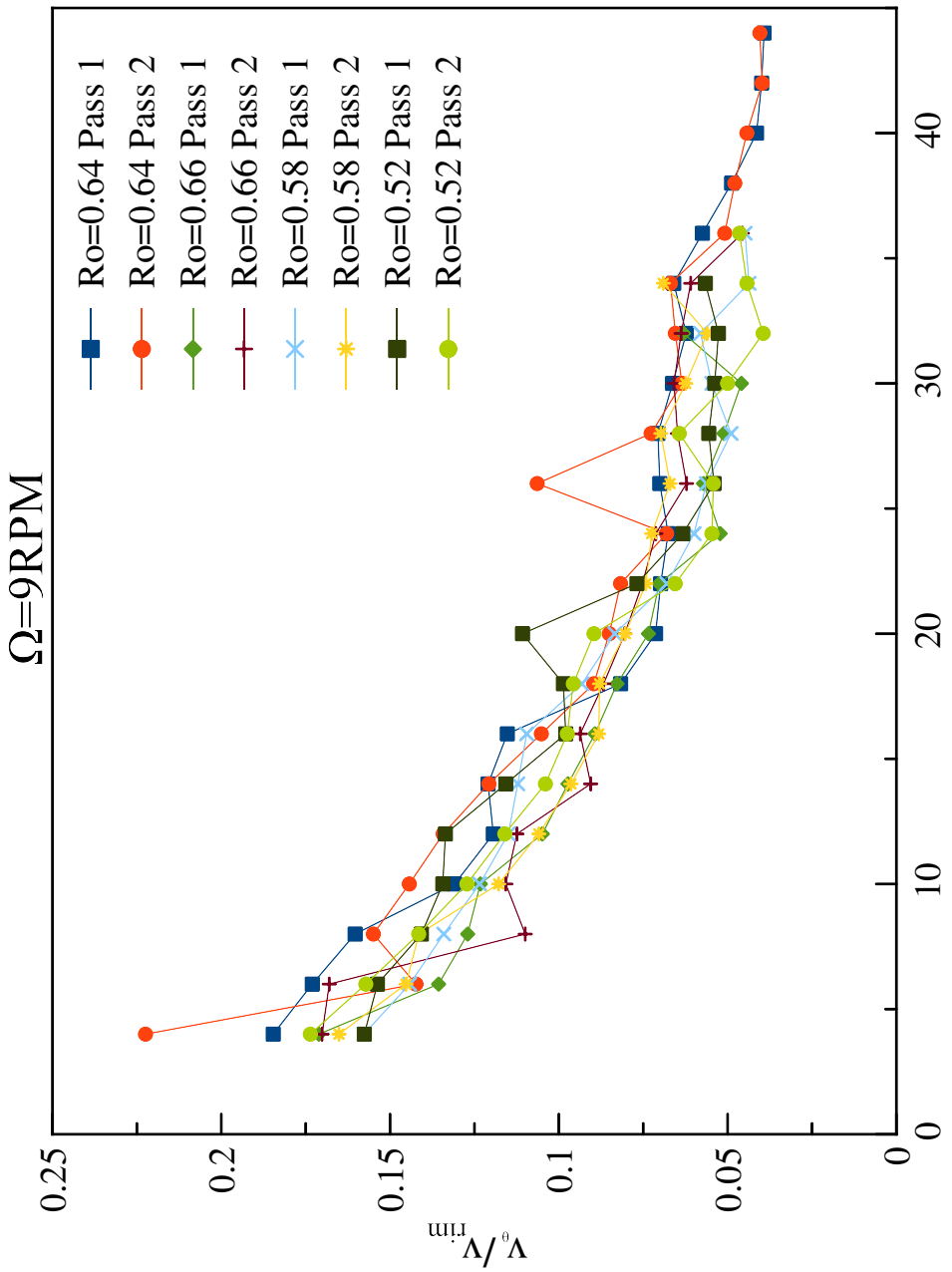

Figure 10.6: The dependence of the maximum azimuthal velocity on height for Ω = 9RPM.

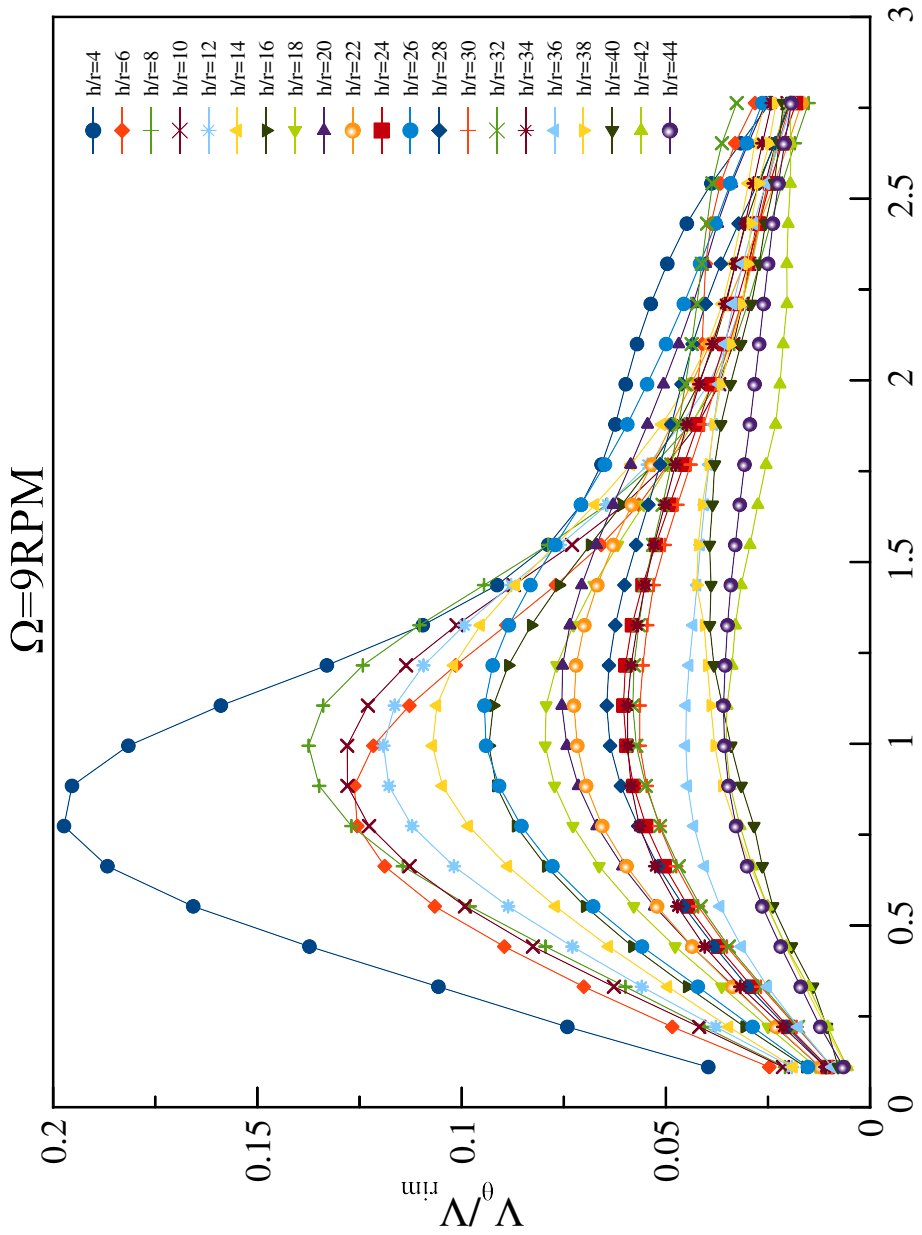

Figure 10.7: Azimuthal velocities for Ω = 9RPM and Ro = 0.64.

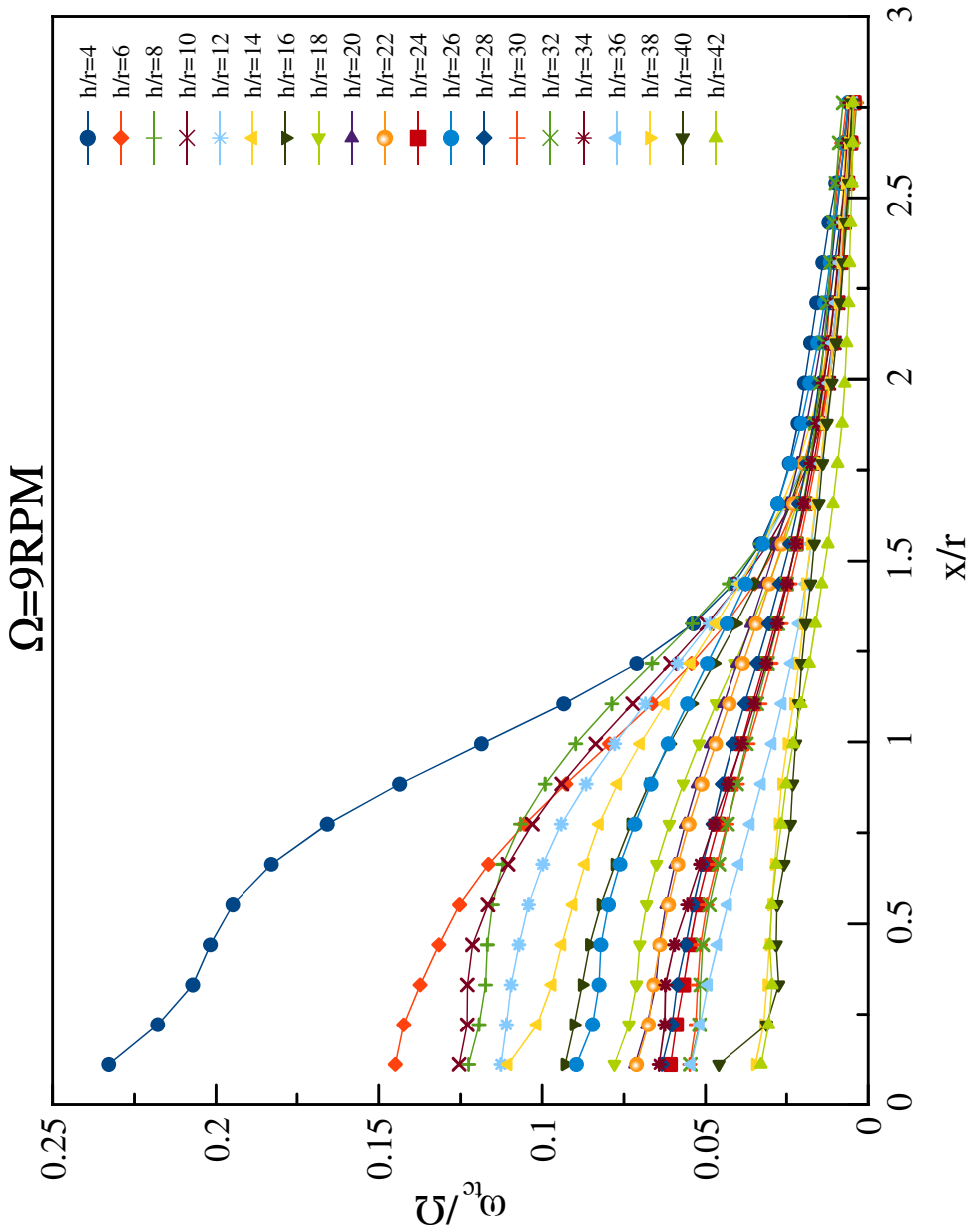

Figure 10.8: Angular velocities for Ω = 9RPM and Ro = 0.64.

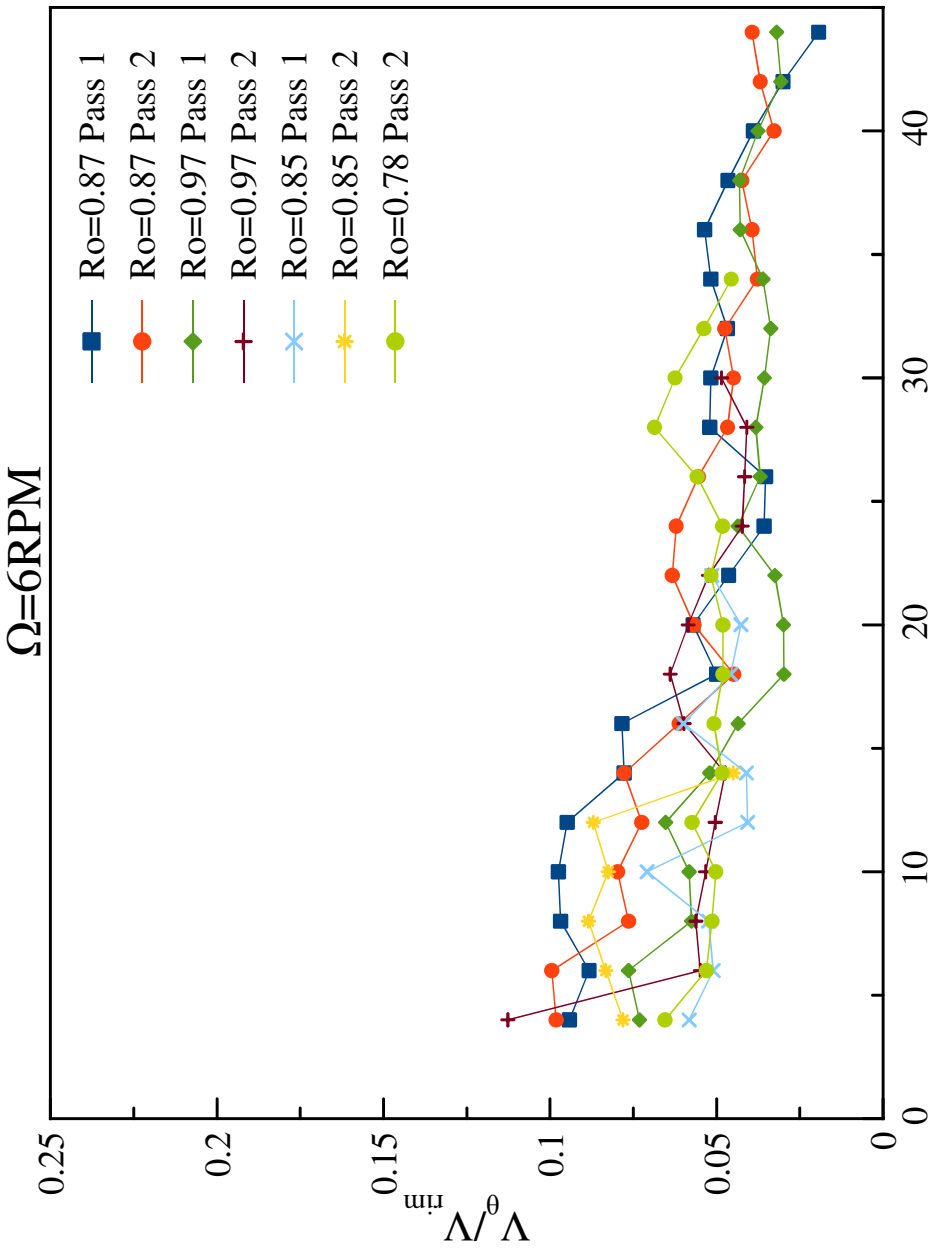

Figure 10.9: The dependence of the maximum azimuthal velocity on height for Ω = 6RPM.

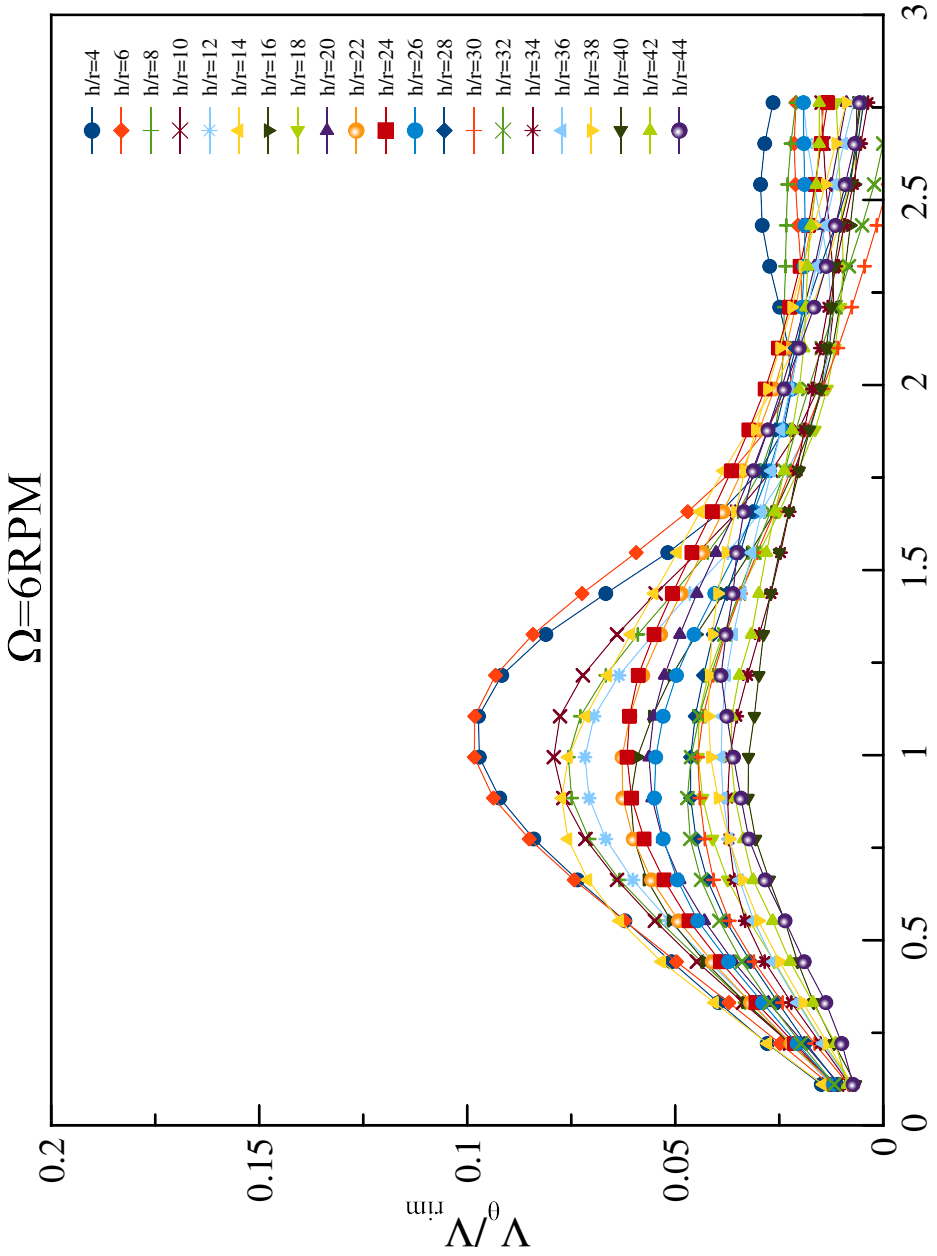

Figure 10.10: Azimuthal velocities for Ω = 6RPM and Ro = 0.87.

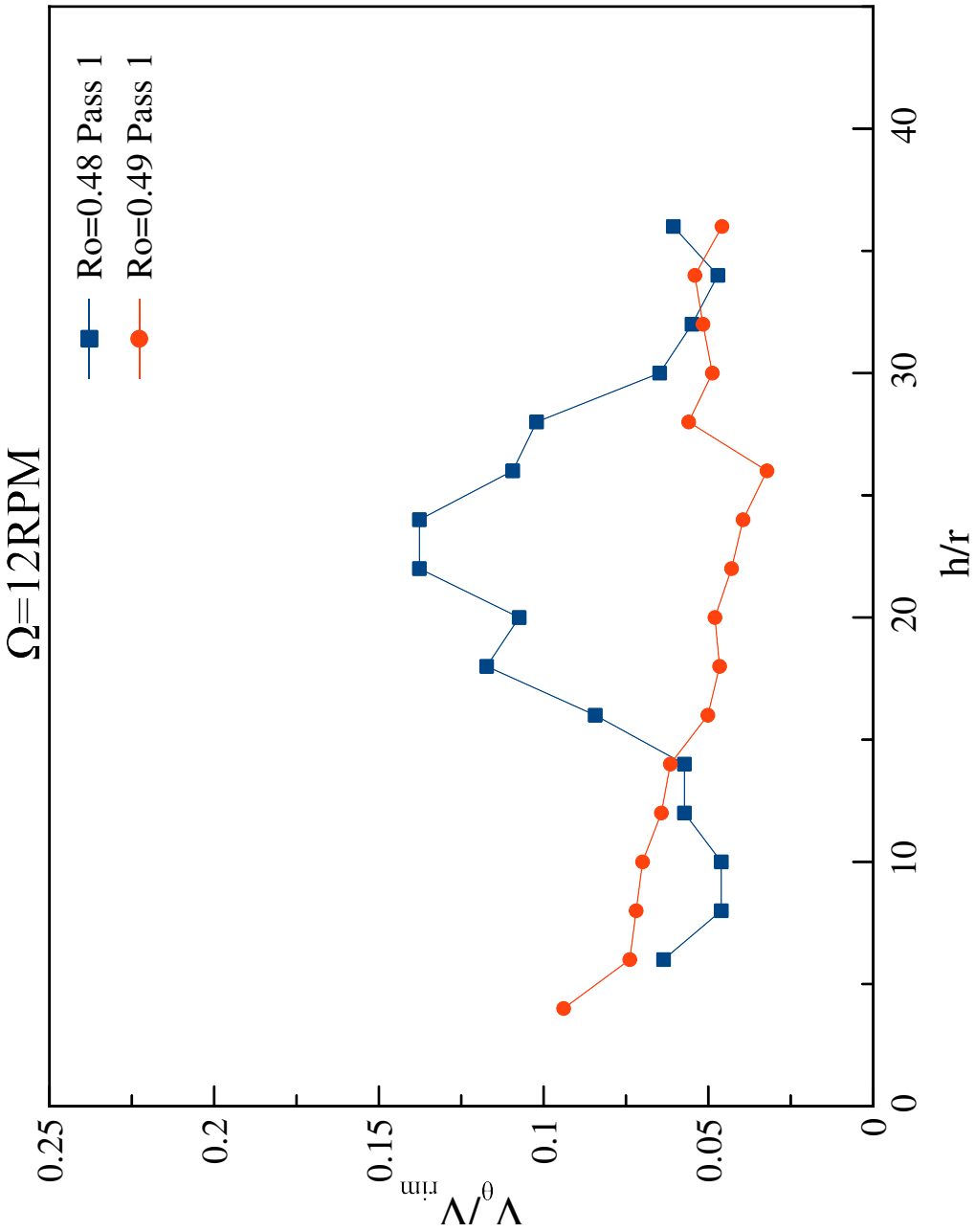

Figure 10.11: The dependence of the maximum azimuthal velocity on height for Ω = 12RPM.

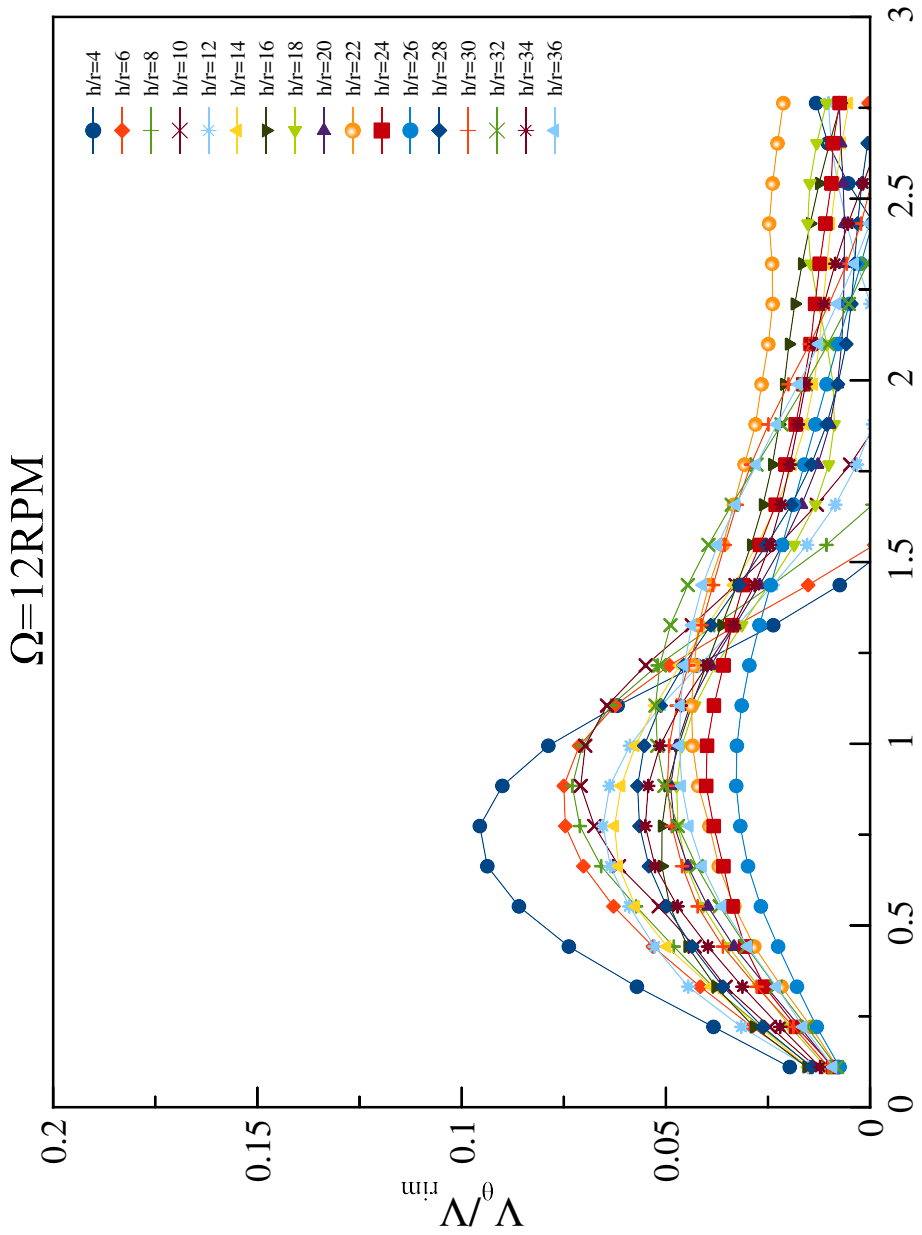

Figure 10.12: Azimuthal velocities for Ω = 12RPM and Ro = 0.48.

10.2.2 Negative Ro

For $Ro < 0$ all three Ω produce very similar results, shown in figure 10.13, 10.15 and 10.17 for 6, 9 and 12RPM tank rotation respectively. The azimuthal velocity found is lower than found with $Ro > 0$, but it does not decay strongly. Noise levels are higher, especially at Ω = 9RPM.

Figure 10.14, 10.16 and 10.18 show the radial dependence of the azimuthal velocity for 6RPM with $Ro = -1.0$, 9RPM with $Ro = -0.69$ and 12RPM with $Ro = -0.52$. There is no strong, consistent decay in the Taylor-Column as was observed for $+Ro$.

During some of the experiments the Taylor-Column could be observed visually, due to different densities of clustered particles inside the Taylor-Column and surrounding fluid. The higher density of large clusters of particles made the Taylor-Column appear brighter using normal room-lighting, and a sharply defined column could be seen extending the full length of the tank. The lighting was, however, insufficient for the phenomena to photograph well.

This only occurred under very special circumstances, with particles nearing the end of their life and thus clustering severely. It has not been observed directly for $Ro > 0$, but this could be due to the special conditions necessary to observe this phenomenon.

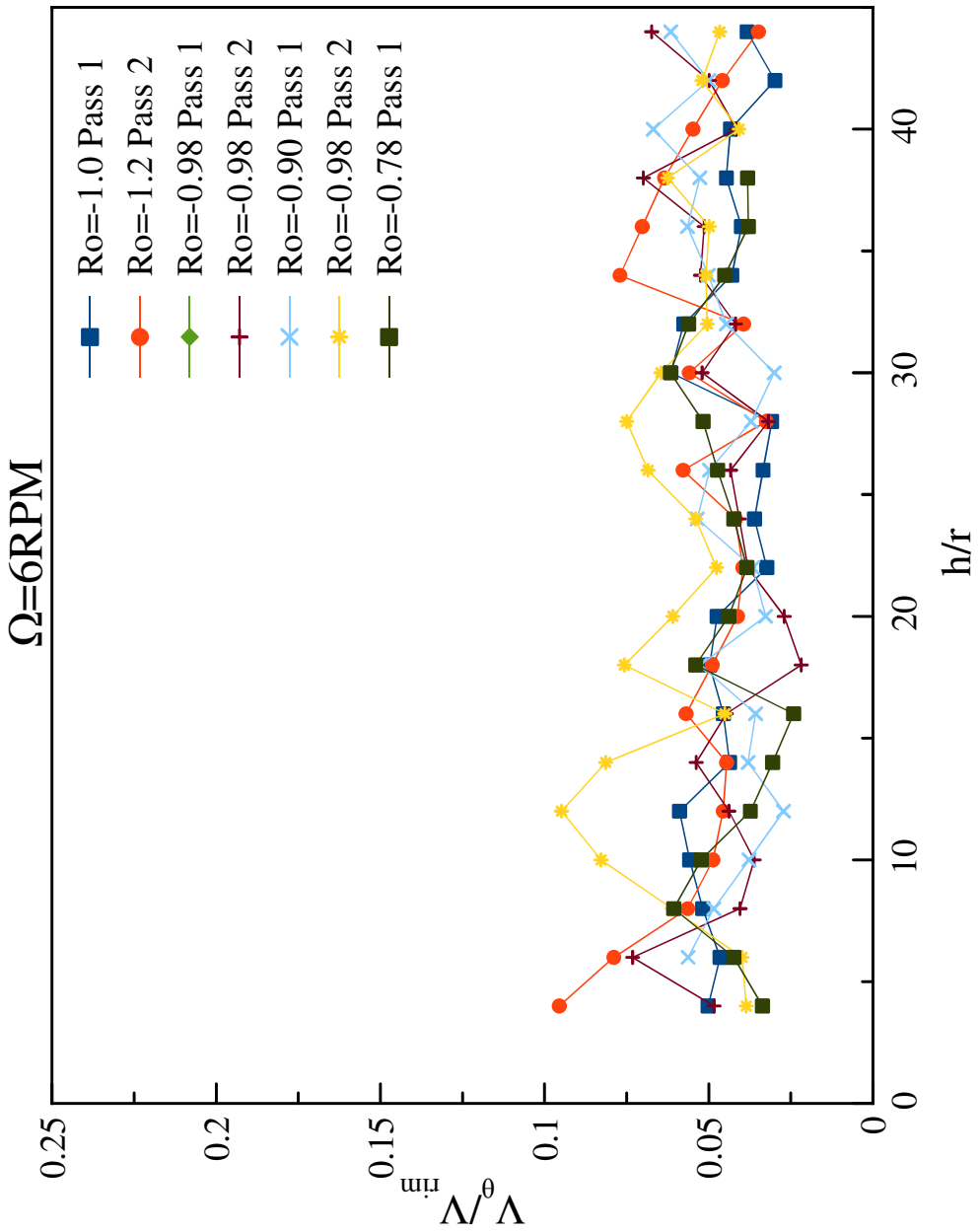

Figure 10.13: The dependence of the maximum azimuthal velocity on height for Ω = 6RPM.

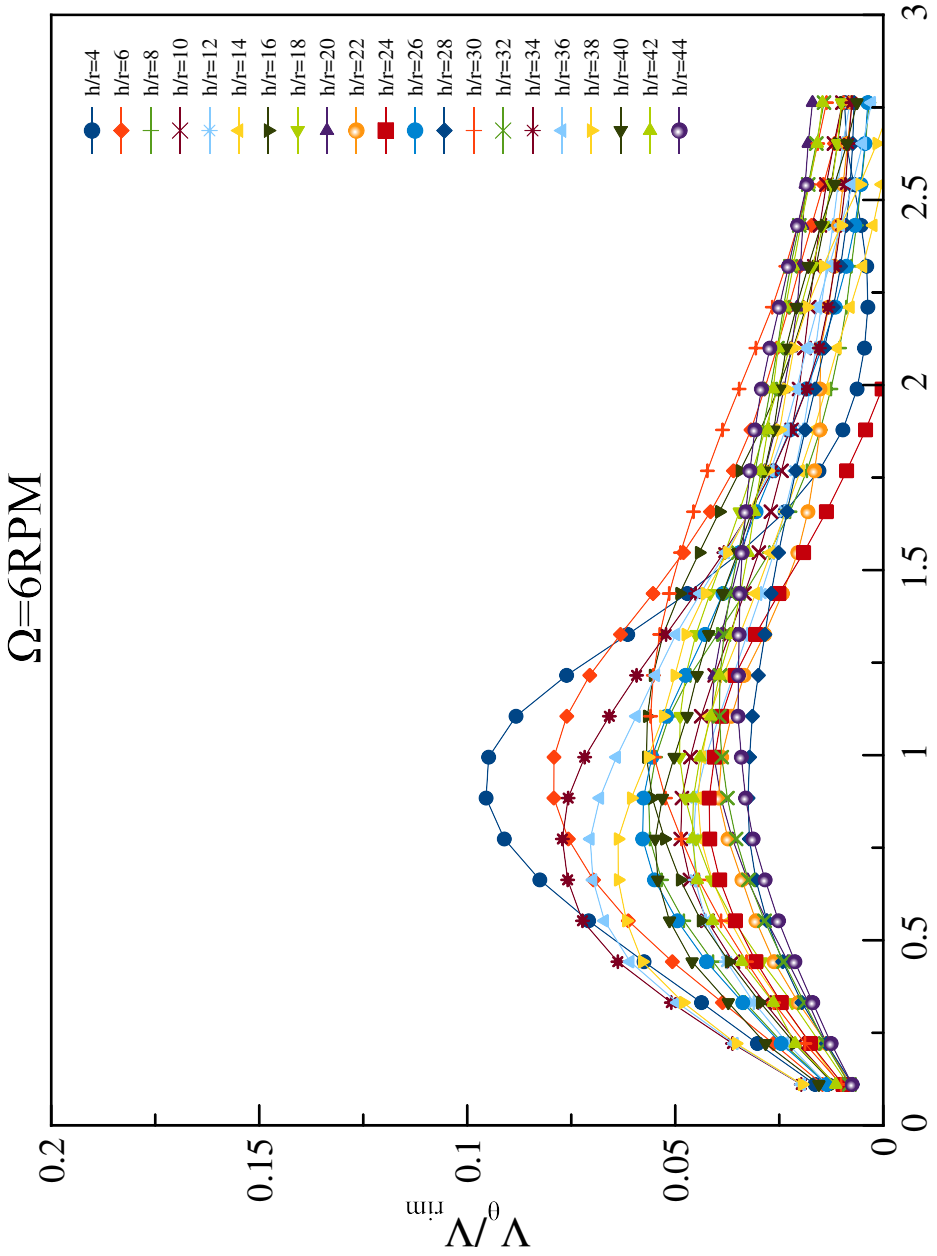

Figure 10.14: Azimuthal velocities for Ω = 6RPM and $Ro = -1.0$.

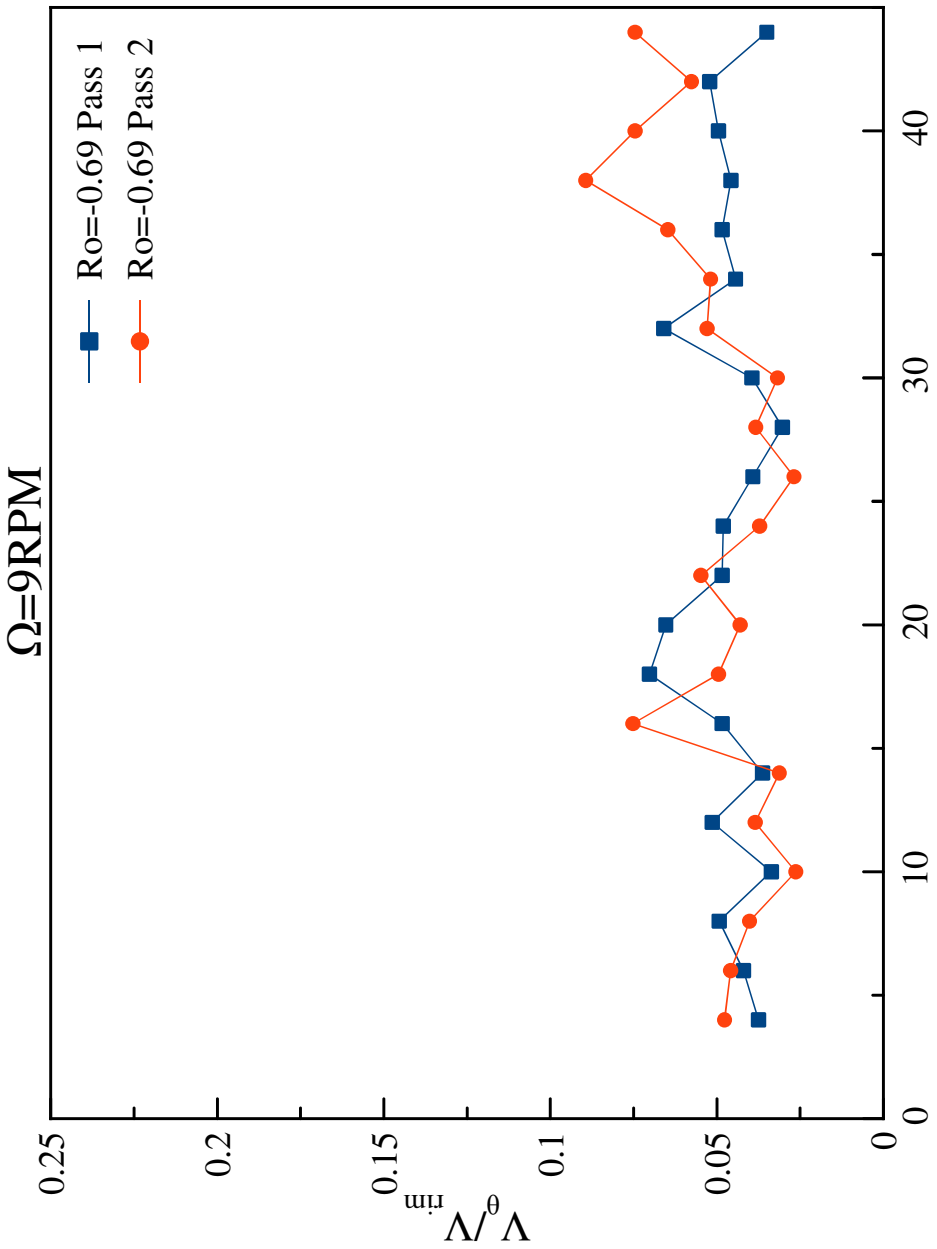

Figure 10.15: The dependence of the maximum azimuthal velocity on height for Ω = 9RPM.

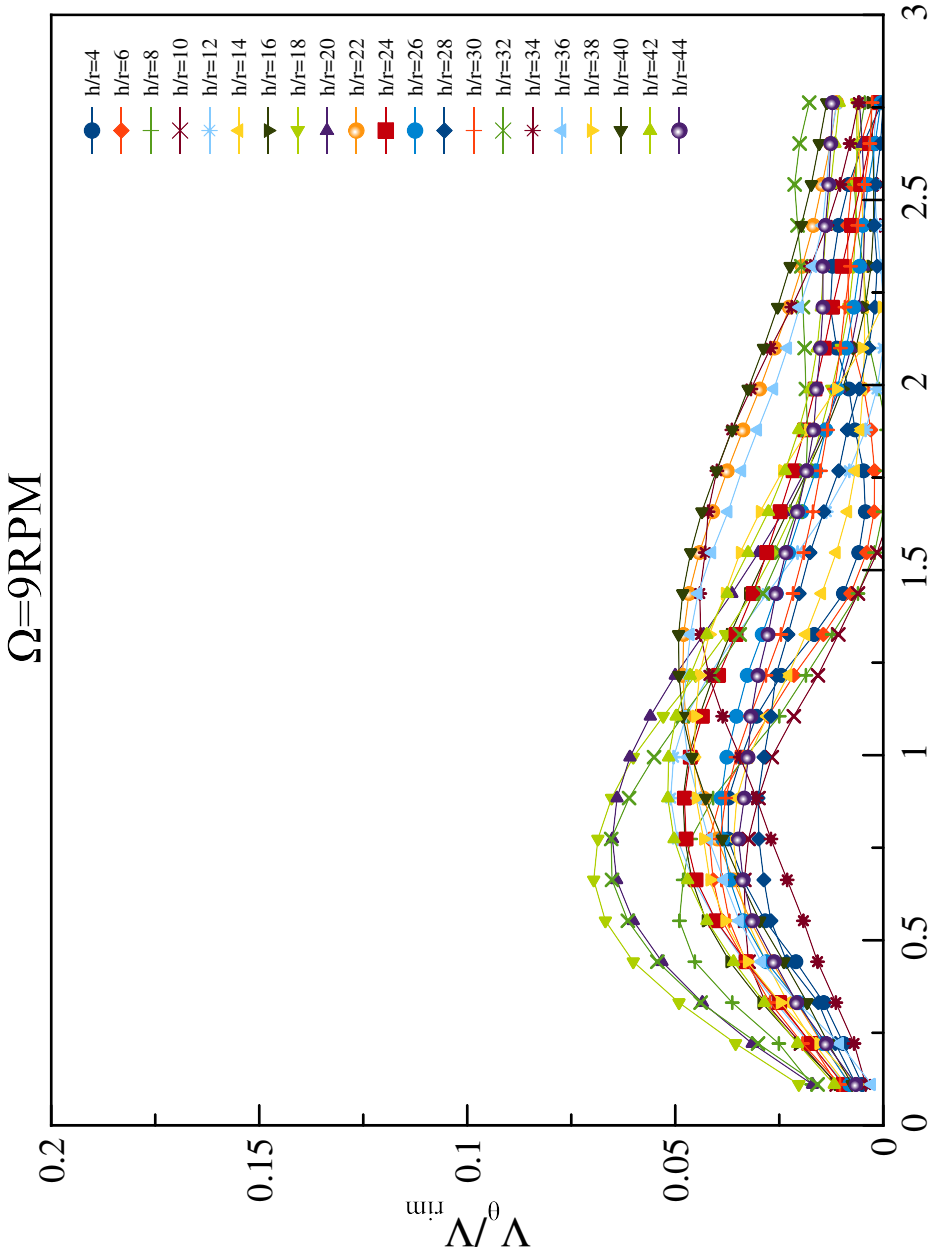

Figure 10.16: Azimuthal velocities for Ω = 9RPM and $Ro = -0.69$.

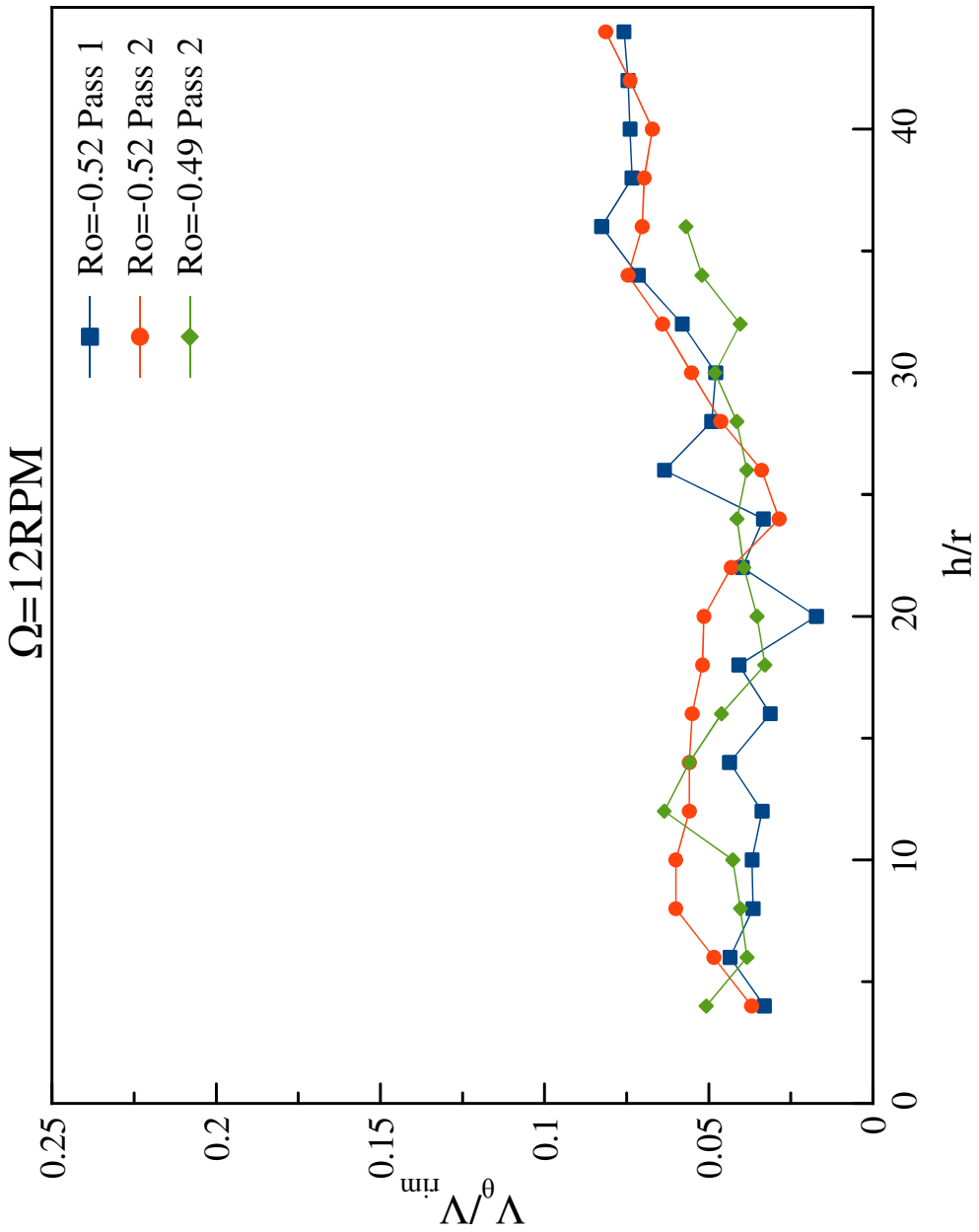

Figure 10.17: The dependence of the maximum azimuthal velocity on height for Ω = 12RPM.

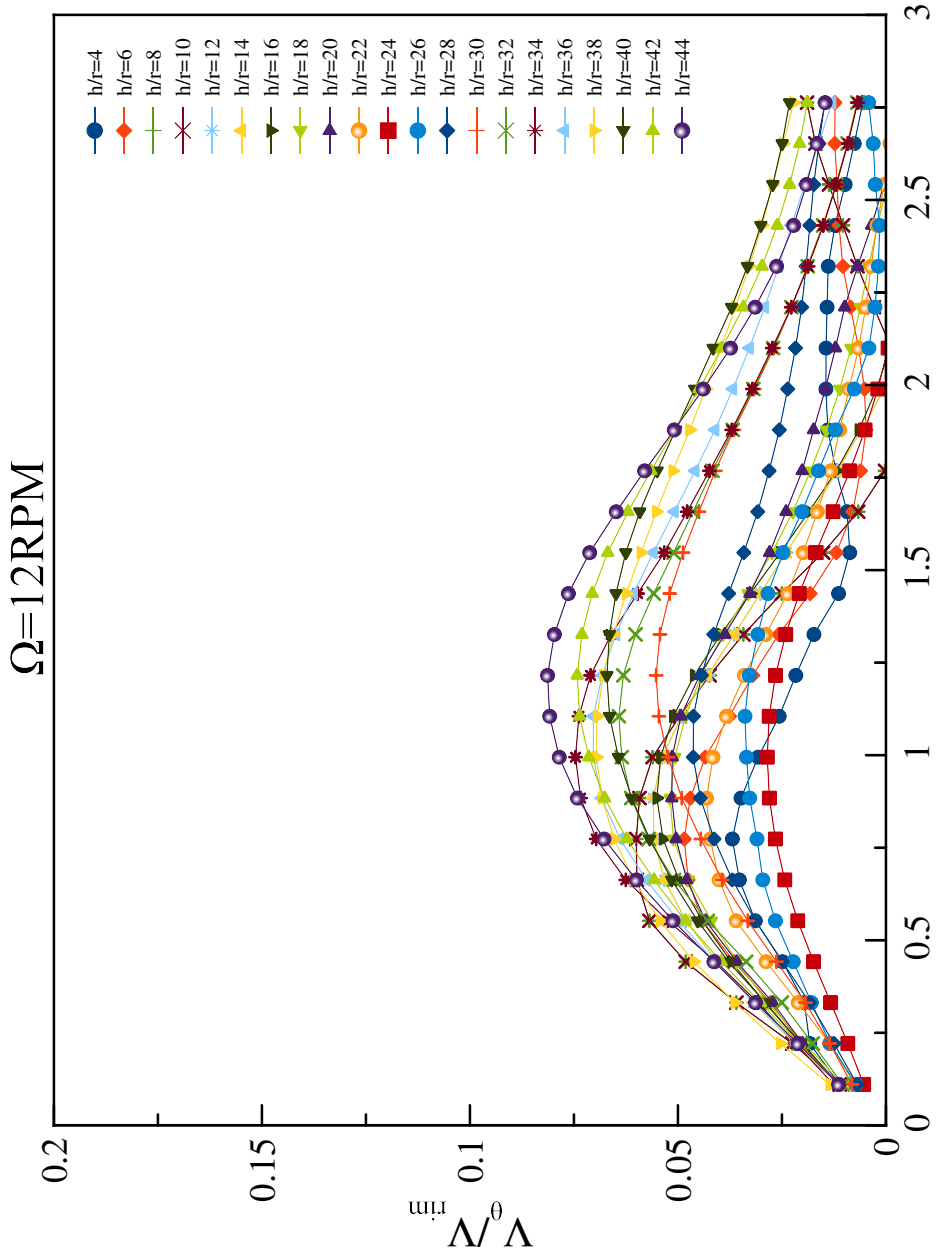

Figure 10.18: Azimuthal velocities for Ω = 12RPM and $Ro = -0.52$.

10.2.3 End-wall

Nearly all data obtained with the end-wall in place has been discarded, with only $\Omega =$ 9RPM and $\omega = -6.2$RPM producing valid data with a clear Taylor-Column. In both passes a clear Taylor-Column is observed, with the second pass ending at 75cm from the disc.

Figure 10.20 shows the full azimuthal velocities at $Ro = 0.68$, corresponding to the red line in figure 10.19. The Taylor-Column appears narrower with the end-wall in place, with a decay similar to $+Ro$ without the end-wall in place.

The difference in quality of the results between experiments with and without the end-wall in place is remarkable, but further research is necessary to investigate the cause. While it is possible that restricting the flow around the disc suppresses the Taylor-Column formation, it is also possible that vibration of the end-wall induces flow noise which obscures the Taylor-Column.

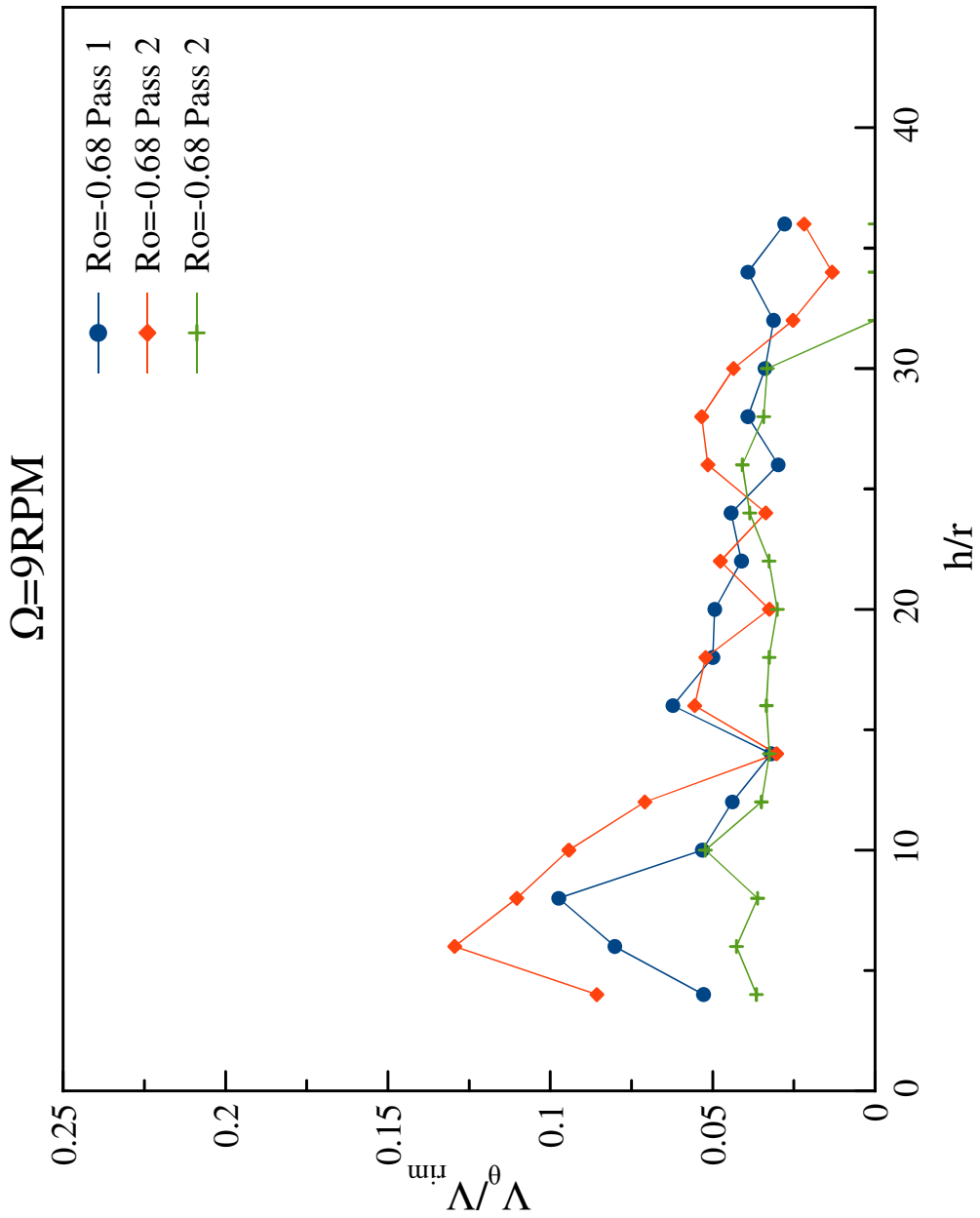

Figure 10.19: The dependence of the maximum azimuthal velocity on height for Ω = 9RPM with the end-wall in place.

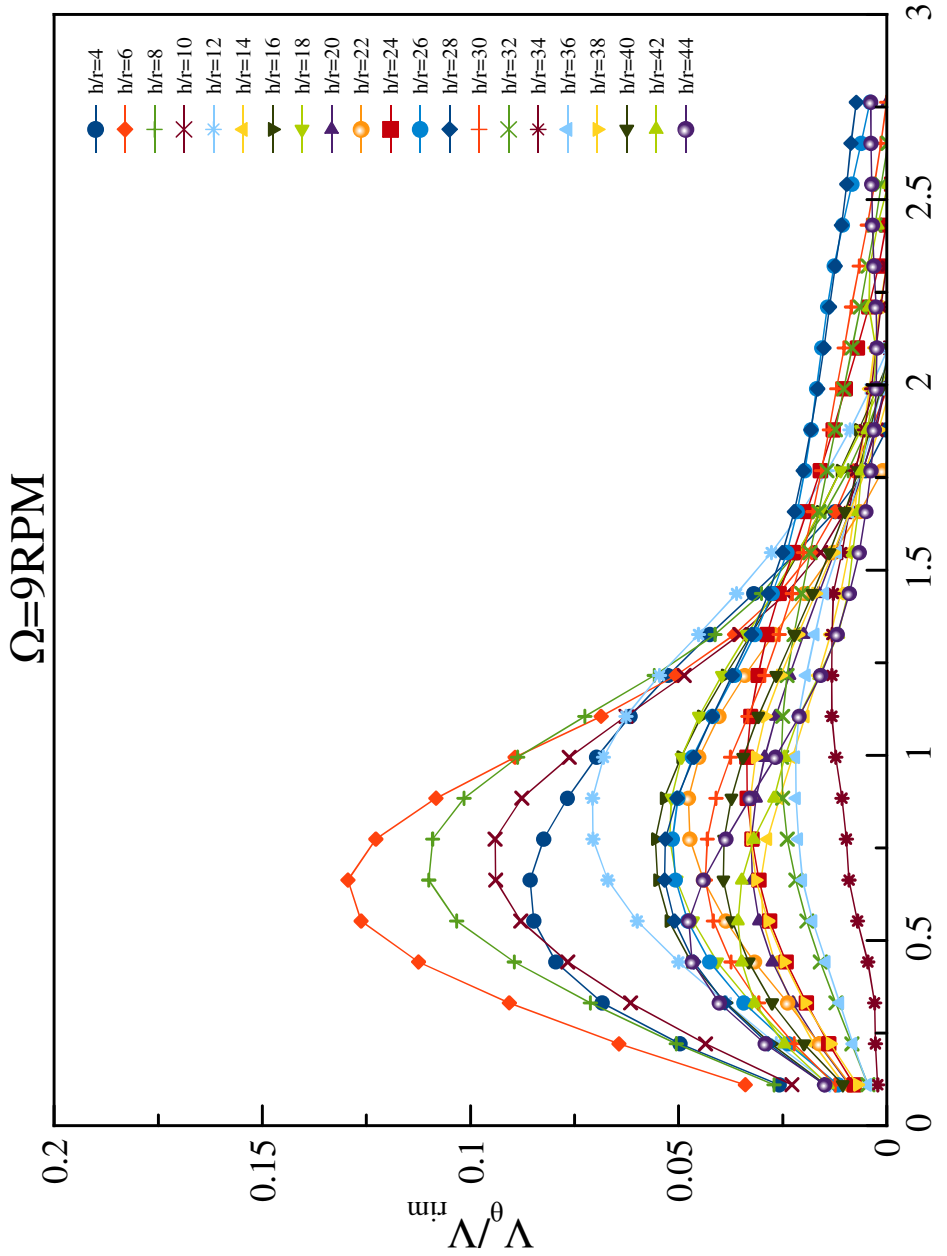

Figure 10.20: Azimuthal velocities for Ω = 9RPM and Ro = 0.684 with the end-wall in place.

10.3 Instabilities

Initially, one of the main objectives was the investigation of the instability of the Taylor-Column. The numerical simulations predict a critical $Ro \sim 0.2$. However, the velocities for these conditions were too low be resolved by the PIV system. All experiments have been conducted in the supercritcial regime, and no experimental observations of the critical *Ro* have been made. It is therefore also impossible to determine the most unstable mode, as at the relatively high *Ro* several modes may be unstable. The dominant mode has been determined, although it is not expected to be unique or consistent with the most unstable mode.

Due to the limited spatial resolution of the PIV-system direct observation of the instability modes is not possible. The intricate details of the flowfield as found by Hide and Titman [13] or Aguiar [3], such as the small counter-rotating vortices on the edge of the Taylor-Column, have not been observed in the vectorfields. The instability modes have only been determined using the algorithm described in section 9.3.4.

In nearly all cases the dominant mode found is $m = 2$, which is consistent with previous experimental observations which find a reduction in mode with increasing *Ro* [9][13]. While in a few cases higher modes such as $m = 3$ and $m = 4$ are found, this only occurs in very noisy datasets. The interaction of the noise with the Taylor-Column in these cases can adequately explain the higher m, and may not be physical.

10.4 Centre Rotation

In the experimentally obtained vectorfields, it was found that the centre of the Taylor-Column was not stationary. An algorithm, described in section 9.3.1, has been used to determine the centre of the Taylor-Column in each vectorfield.

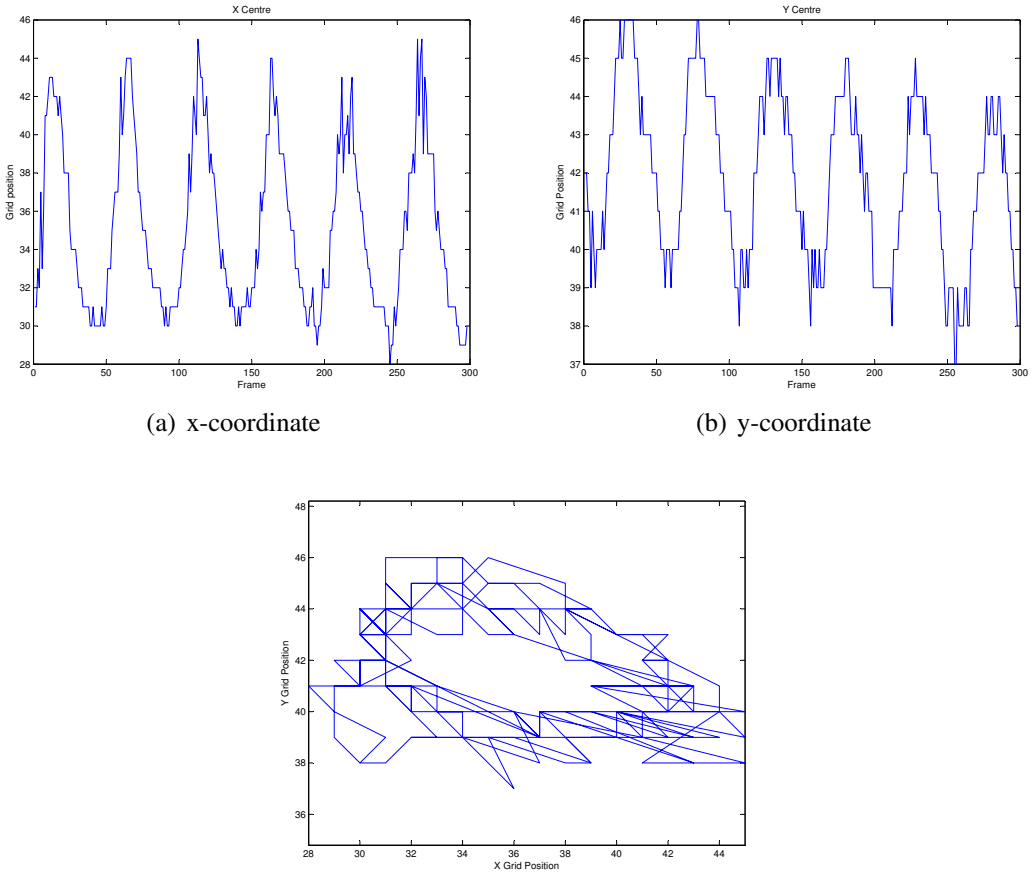

(a) x-coordinate

(b) y-coordinate

(c) parametric plot

Figure 10.21:
The centre of the Taylor-Column was found to rotate. In (a) the x-coordinate of the centre and in (b) the y-coordinate. The position of the centre describes nearly a circle, as can be seen in (c). The algorithm is only accurate to 1 gridpoint, which causes the jagged appearance of the plots.

The Taylor-Column centre was found to rotate with exactly the same rate as the tank, a plot at Ω = 9RPM is shown in figure 10.21. This remains true for all three rotation rates, showing either 6, 9 or 12 rotations per minute. The rotation of the centre of the Taylor-Column is always anti-cyclonic, independently of the sign of rotation of the disc, with amplitudes in the order of 2cm. The motion suggests the Taylor-Column is (locally) off-axis, with possibly a fixed position in the laboratory frame, with the cameras rotating around it. However, the centre of the rotating tank is undefined in the camera frame. It is therefore impossible with current data to determine the exact spatial position of centre the Taylor-Column.

Chapter 11

Discussion

The decay in azimuthal velocity of the Taylor-Column at increasing distance from the disc found experimentally has not previously been observed experimentally or predicted theoretically or numerically. Theoretical models [11] estimate the length of the Taylor-Column to be $h_{TC} = E^{-1}r$. Using the Ekman number based on disc radius, the highest value found in the experiments is $E_r = 2.5 \cdot 10^{-3}$ at $\Omega = 6$RPM, predicting $h_{TC} \approx 400r = 10$m. The difference between positive and negative Ro is also striking. The azimuthal velocities are lower for $-Ro$, but the velocity does not decay.

None of the previous experimental studies have looked specifically at the vertical dependence of the flow. Hide and Titman [13] and Niino and Misawa [28] have not performed any quantitative measurements of the azimuthal velocity at all, due to limitations in their visualisation systems. While Früh and Read [9] and Aguiar [3] have looked at azimuthal velocities, they have not investigated any vertical variation. The PIV-system used by Aguiar has a lightsheet thickness of 5cm, which is thick relative to the fluid depth of 10cm, and precludes accurate measurement of vertical variations

in the flow.

The numerical work performed by Hollerbach [16] and the extension of this work performed during the current investigation do not show any vertical variation, despite the already significant fluid depth. The numerical code does not assume that the flow is vertically uniform, and is able to resolve vertical variations in the flow, such as the Ekman layers. It is possible that the numerical solution changes when the size of the inner sphere is further decreased, as the parameter range does not overlap. However, it is more likely that a discrepancy exists between the underlying assumptions of the numerical code and the true experimental conditions. One such possibility is the existence of temperature gradients in the experiment, which have not been taken into account by the version of the code used in this project. The stratification which can result from temperature gradients has been considered by a different numerical study by Hollerbach [18], and the potential effects on the experiment are discussed below.

11.1 Measurement Uncertainties

Both the PIV-system and the residual motion and noise in the tank contribute to the uncertainty in the measurements. The effects of both have been mitigated to an extent by careful data selection and processing.

11.1.1 Noise and residual motion

The flow-noise in the tank has significantly complicated the analysis of the data. The noise obscures the Taylor-Column, which then cannot be measured. More importantly,

the noise potentially suppresses the formation of the Taylor-Column. No clear patterns have been identified in the noise, except that $\Omega = 9RPM$ appears to be less noisy for positive disc rotation and $\Omega = 6RPM$ for both positive and negative disc rotation.

At present, no detailed study has so far been performed to assess the residual motion in the tank after spin-up is thought to be complete. For previous experimental work on Vortex Rings [6] and the Sphere Wake [40] this has not been a serious shortcoming, as the flow velocities of interest are much greater than in the current investigation.

A full analysis of the causes and effects of noise could not be performed in the current study, due to the complexity this involves. The sources of noise are numerous, and may interact with each other. Mechanical causes include vibration or non-uniform angular velocity of the tank. A small vibration can be observed when the tank is rotating, which manifests itself as very small waves on the surface of the tank. Spatial and temporal variations in the temperature may cause convection currents to exist in the tank, and these can indeed be seen in a stationary tank by visually observing particle motion.

Flow-noise could be caused by other means in addition to the ones mentioned above, and it is possible for noise to exist in an otherwise “perfect” setup if it is generated by the flow itself rather than an imperfection.

11.1.2 PIV-system

The PIV-system has been designed based on predictions by the numerical simulation of the expected flow-velocities. In the actual experiments the velocities were much lower than predicted, and the system was running outside of the intended operating parameters. The processing relied heavily on the sub-pixel accuracy algorithms present in DaVis, but this introduced some uncertainty in the results. This problem is significantly mitigated for the azimuthal velocity profiles, since the random errors are reduced by extensive spatial and temporal averaging.

For the instantaneous vectorfields, which are used for determining the instability mode, the uncertainty introduced by the PIV system is potentially more serious. Spurious modes can be introduced, although the temporal averaging will to an extent reduce these errors.

11.1.3 Combined effects of Noise and PIV-system

The combined effects of flow-noise and the limited range of the PIV system severely complicates the analysis of the data. If a Taylor-Column cannot be identified in the velocity vectorfields, one of four scenarios is possible:

- The Taylor-Column does not exist.
- Noise suppresses the Taylor-Column, which would otherwise exist.
- A Taylor-Column exists, but noise obscures it.
- The PIV-system cannot resolve the Taylor-Column due to the very low flow velocities

present.

Absence of a Taylor-Column in the measurements therefore cannot be interpreted as conclusive proof that the Taylor-Column has ended. It is very common for the Taylor-Column to be interrupted by noise, while it can reasonably be expected for the Taylor-Column to be continuous.

Of the two causes mentioned above, the flow-noise is a much greater problem than the uncertainties introduced by the PIV-system. While the design of the PIV-system effectively restricted the analysis to a narrow band of flow velocities, this problem could be circumvented by carefully choosing the data to process. Aided by temporal and spatial averaging, the results are consistent. The flow-noise that is physically present in the tank cannot be reduced by simple averaging, as it alters the flow in the Taylor-Column and is not a random error. By very careful selection of the datasets, including visual inspection of all datasets and discarding all "suspect" data, the effects of noise have been reduced, but not completely eliminated.

11.2 Vertical Dependence of Azimuthal Velocity

11.2.1 Incomplete Taylor-Column Formation

An incomplete formation of the Taylor-Column could explain the vertical variation in azimuthal velocity as observed in the experiments. The time-scale for the formation of the Taylor-Column is expected to be of the order of the Ekman spinup time, which is 30 minutes [5]. A few long experiments have been performed to confirm this es-

timate. These experiments have been performed by recording particle images for 1 hour at 50cm distance from the disc, with ω = 4RPM. The flow speeds, however, were found to be too low to be resolved by the PIV-system, and no Taylor-Column could be observed.

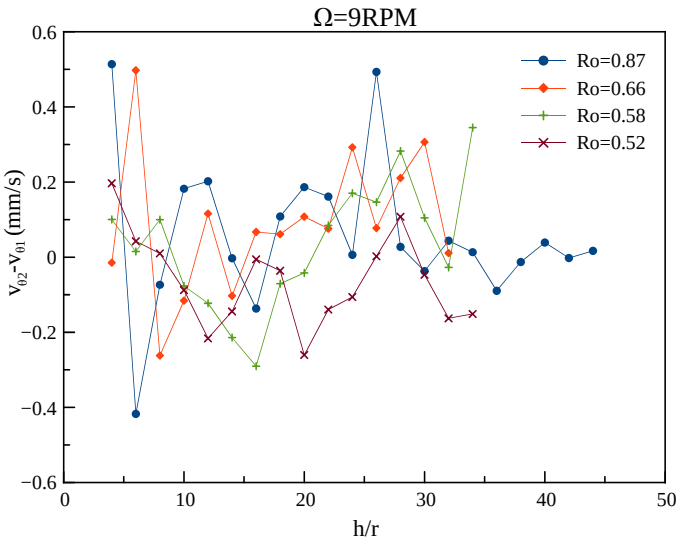

Figure 11.1: The difference in azimuthal velocity between the two measurement passes is not significant, which rules out incomplete Taylor-Column formation.

For each combination of tank and disc rotation the Taylor-Column is scanned twice, the completeness of Taylor-Column formation can be assessed by comparing both passes. If the Taylor-Column is still being formed during the first pass, the second pass should show higher flow velocities and/or a longer Taylor-Column. Figure 11.1 shows the difference in azimuthal velocity between the two passes at 9RPM with $+Ro$. A fluctuation around zero can be seen, which is not significant compared to the level of noise on the measurements. Incomplete Taylor-Column formation can therefore effectively be ruled out as a possible cause.

11.2.2 Stratification

Hollerbach [18] investigated the influence of stratification on the formation of the Taylor Column numerically. The code used is an extension of the same numerical code used for the computational work performed in this study. The stratification and gravity are oriented vertically, similar to the orientation in a laboratory experiment, rather than in the radial direction as in planetary interiors. All experiments have been performed with a radius-ratio of 6 between the inner and outer sphere. The stratification parameter is defined as:

$$S = \frac{\alpha\beta g}{\Omega^2} Pr \tag{11.1}$$

Where α is the thermal expansion coefficient, β the imposed temperature gradient, g the specific gravity and Pr the Prandtl number. For water, $\alpha \approx 2 \cdot 10^{-4}$ and $Pr = 7$.

Computations have been performed at three Ekman numbers, and four values of S. The results are reproduced in figure 11.2. Of each group of three, the left panel shows contours of the angular velocity, the middle shows streamlines of the meridional circulation, and the right shows the non-dimensional temperature deviation Θ. The numbers underneath correspond to $10^4 \cdot \psi_{max}$ for the middle panel, and Θ_{max} on the right.

The results show that when the effect of stratification is increased, corresponding to a increase in S and moving to the right in figure 11.2, the formation of Taylor-Columns is suppressed. The angular velocity is reduced, and the meridional circulation decreases. At very high values of S, the Taylor-Column will not reach the outer sphere, while at

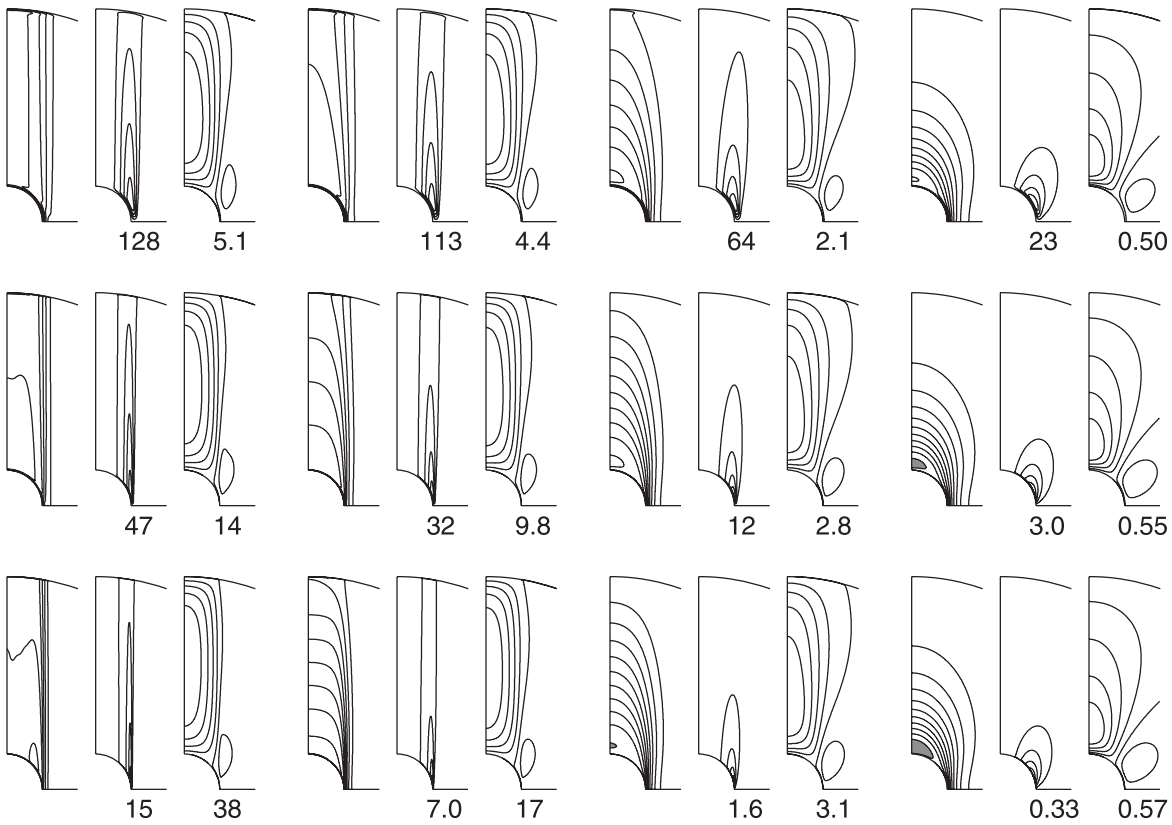

Figure 11.2: From left to right, the three panels show contours of the angular velocity, streamlines of the meridional circulation and the non-dimensional temperature deviation. From left to right, the groups correspond to $S = 10^{-3}$, $S = 10^{-2}$, $S = 0.1$ and $S = 1$. From top to bottom $E_r = 10^{-3}$, $E_r = 10^{-4}$ and $E_r = 10^{-5}$. Reprinted from [18].

more modest values of S the angular velocity decreases with increasing distance from the disc. Simulations have been performed at both positive and negative differential rotation, and in both cases the stratification supresses Taylor-Column formation in a similar manner.

In the experiment, a small temperature gradient is likely to exist, and while there is a significant difference in radius-ratio between experiment and computation, a tentative

comparison can be made. Using equation 11.1, and assuming a modest temperature difference of $1°C$ between the top and bottom of the tank, yields: $S = 1.4 \cdot 10^{-2}$ for Ω = 6RPM, $S = 6.2 \cdot 10^{-3}$ for Ω = 9RPM and $S = 3.5 \cdot 10^{-3}$ for Ω = 12RPM.

The assumptions above correspond to the second and third group of panels fom the left in figure 11.2. The panel showing the angular velocity, on the left of the group of three, shows an already significant reduction in angular velocity further away from the disc. This indicates that a relatively small temperature differential could therefore be responsible for the decay in azimuthal velocity observed experimentally.

When the experiment was designed, the influence of temperature variations was expected to be much less than predicted by the above study, and the measurement uncertainty for the temperature difference is $\pm 1°C$, which is relative high. The temperature difference measured between top and bottom is in the order of $\pm 1°C$, which is similar to the measurement uncertainty. The data is thus insufficient to either prove or disprove that stratification plays a role.

To gain further insight in the role of stratification on the results, further experimentation and computation is necessary. An improved temperature monitoring system, with more accurate sensors at more heights in the tank will allow a more precise assessment of the presence of temperature gradients in the tank. An extension of the numerical work to a larger radius-ratio will allow a better prediction to be made of the critical temperature difference where stratification starts to play a role in the experimental setup.

11.2.3 Other Effects

There are several other possible causes for the observed results that have not been investigated in detail. Most importantly, the influence of flow noise on the Taylor-Column deserves further attention in a future investigation. The set of parameters chosen for the experimental work also may explain the discrepancy with previous work. The Taylor-Proudman theorem assumes $Ro << 1$, which is certainly not the case in the experiments where $Ro \sim 0.5 - 1$ due to limitations of the visualisation system.

11.3 Rotation of the Centre of the Taylor-Column

The centre of the Taylor-Column has been found to oscillate with the same frequency as the Ω. Several possible causes are discussed below.

11.3.1 Possible Mechanical Causes

The rotation of the centre can potentially be introduced due to a purely mechanical vibration, and it is important to investigate this possibility. As the camera frame no longer has a fixed reference point to the axis of rotation, it is possible that the camera frame is moving relative to the fluid. The magnification factor of the optical system, where 15cm in real space is projected onto a sensor of 0.8cm, will amplify any vibration of the sensor to a much larger amplitude the field of view of the camera. The top position of the traverse had been chosen to show the disc in the camera images, illuminated by the laser. These images show if the cameras have moved from their initial position. If a significant vibration (or any movement) of the cameras is present,

it would be visible on these images. Analysis of these images between several datasets show no significant difference, both within a single dataset and between datasets taken several weeks apart.

While the above effectively rules out a vibration of the camera relative to the tank, there is still a possibility of the entire tank including the camera assembly vibrating relative to the fluid. This, again, is unlikely, as a vibration with an amplitude of several cm would have been observable visually. A more complex interaction between tank and fluid inducing a periodic wave is, however, still possible, and this cannot be completely ruled out with the current data.

11.3.2 Precession Due to Earth Rotation

An effect similar to the centre rotation in the current study has been observed in another experiment, performed on the 3 meter rotating sphere system at the University of Maryland [37]. In the experiment, two coaxial spheres are rotating in a geometry similar to the numerical code used for the current investigation. The diameter of the outer sphere is 3m, and the gap in between the spheres is filled with water. An oscillation which also has the exact same frequency as the tank rotation has been found experimentally. This has been attributed by the group conducting the experiments to precessional forcing by the rotation of the Earth [37][20].

It is possible that a similar effect explains the centre rotation found in the current investigation. Time constraints prevented a full investigation, and further study, includ-

ing processing and analysis of the data obtained with the vertical lightsheet is recommended.

Chapter 12

Further Work

The experimental results identify several opportunities for further research. Upgrading the experimental setup is the first priority, which will improve the accuracy of the results and greatly extend the parameter range that can be attained.

12.1 Upgrades to the Experimental Setup

The experimental setup is being relocated at the time of writing, which presents an ideal opportunity to address several issues that exist with the experimental setup. Recent developments in electronics, such as the availability of small, low-cost accelerometers [4], can be taken advantage of which will guide mechanical improvements to the rotating tank.

12.1.1 Rotating Tank

When running the experiments, some vibration of the tank was observed, which can be coupled into the flow which will cause spurious flows. The unstable rotation of the tank at certain rotation rates also limits the parameter range that can be attained. An in depth analysis of the mechanical behaviour of the tank is to be performed, to identify sources of undesired motion and to provide solutions to mitigate their effects.

While some of the effects can be observed on PIV-data, this is not a particularly good method due to the relatively low temporal resolution and long processing time required. A more convenient solution exists in the form of accelerometers which measure vibration and oscillation directly. This can be integrated into the automated data-acquisition system to provide simultaneous PIV and acceleration data allowing a direct estimation of the effects of these motions on the flow.

12.1.2 PIV-system

The PIV-system operated well in the narrow range of flow velocities it was designed for, and the automated data-acquisition system allowed a large amount of experiments to be performed in a short amount of time. A few upgrades can be made to the system which will increase the range of velocities that can be measured, and thus expand the range of experiments that can be performed with it. The most important component to upgrade is the laser, a more traditional pulsed laser will allow the camera to operate with much lower shutter times, allowing higher flow velocities to be measured. Upgrading the cameras to higher-resolution models will allow for a better spatial resolution. This allows measuring the Taylor-Columns at much lower flow velocities and

may reveal some of the more intricate features of the flow.

Upgrading DaVis to version 8 will allow PIV-processing to be performed on a graphics card, with a 10-fold increase in performance compared to the computer used in the current study [22]. The additional processing power will allow for a much quicker evaluation of experimental results, which will speed up development of the setup. Combined with the automated data acquisition developed in the current project, it will allow very quick data collection and processing, which will greatly increase the scope for future investigations.

12.2 Further Experimental Work

The experimental results show there is significant scope for a further study to investigate several of the observations in more detail. Several possibilities are outlined below.

12.2.1 Full Height Measurements

Measurements have only been performed on the first 110cm below the disc due to physical constraints on the traversing PIV-system. Converting the PIV-system for the cameras to look down rather than up is a straightforward method of obtaining data from the lower part of the tank. This is, however, very time consuming as the PIV system needs to be aligned and calibrated. Necessarily, the top and bottom fractions of the Taylor-Columns will be taken days or weeks apart, and they will not form a continuous measurement. Therefore, ideally two PIV systems are used, with one looking

up and the other looking down. Alternatively, a single good quality stereo-PIV system can possible provide sufficient data with a single vertical lightsheet, which allows movement along the entire height of the tank, at the expense of accuracy.

12.2.2 Assessment of Residual Motion

When the tank is spun up, it is expected to reach solid body rotation after a sufficiently long time has passed. However, even after a very long time motions will persist in the tank. These residual motions had a significant effect on the measurements taken in the current study, requiring a large amount of data to be discarded. There are several possible mechanisms that cause persistent residual motion, including temperature effects, tank vibration and precession.

An analysis of the behaviour of the fluid in the tank without any forcing except tank rotation is essential for future research. Separating the various different contributions to the motion, such as mechanical vibration, convection, precession and residual turbulence requires a significant experimental and theoretical effort, which has been beyond the scope of the current investigation. Advances in experimental equipment and efficiency of PIV software will simplify at least the experimental work needed, which may help to focus the analytical modelling. An in-depth assessment of the residual motion will allow experimental strategies to be used that mitigate their effects and improve the performance of the experimental setup for low-speed flows.

12.2.3 Multiple Aspect Ratios

While three discs have been manufactured, only one disc has been used in the experiments. The influence of aspect-ratio can be investigated by using the two other disc sizes. To allow for more aspect ratios, a horizontal, movable perspex plate can be placed in the centre of the tank, which effectively restricts the height of the tank. This allows investigation of the role that aspect ratio and fluid height play on the velocities found in the Taylor-Column. Aspect ratios can be chosen that are similar to the range which is easily numerically accessible, allowing for a direct comparison between experimental and numerical results.

12.2.4 Stratification

Numerical work has suggested that stratification may play a role in the suppression of the Taylor-Column. This can be further investigated with a few modifications to the experiment. Accurate temperature sensors which can measure to within $\pm 0.1^{\circ}$ allow the presence of temperature stratification to be estimated more reliably. Experiments can also be designed where a stratification gradient is imposed, either by forcing a temperature gradient, using different density fluids or introducing a salinity gradient. All of these experiments will require considerable effort to be implemented successfully on the very large scale existing on the experimental setup.

Chapter 13

Conclusion

The PIV-system designed and implemented during the project showed a good performance within the range of flow velocities it was designed for. However, due to the velocities in the Taylor-Column being much lower than predicted, it has limited analysis to experiments with relatively high flow velocity. This can be remedied by replacing the laser with a pulsed model, and the cameras with higher resolution variants. The automation of the system proved robust, and it greatly increased the amount of experiments that could be performed.

The numerical work finds solutions consistent with the experimental study of Hide and Titman [13], and numerical work by Hollerbach [16], showing the classical Stewartson-layer solution with no vertical dependence of the flow. The instabilities shown the same asymmetry around the sign of Ro as in Hide and Titman, which is the geometry it most closely resembles. Experimentally, the investigation of the stability was impeded by limitations of the visualisation system and noise in the tank, leading to all experiments analysed being conducted in the supercritical regime.

The experimental results found for $Ro > 0$ are markedly different from previous work, as the velocity in the Taylor-Column decays with increasing distance to the disc, which does not strictly obey the Taylor-Proudman theorem. A stratification gradient produced by small temperature differences in the room has been suggested as a possible explanation. Further experiments are suggested to investigate this theory further, as well as an investigation into the effects of the significant residual motion in the tank.

For $Ro < 0$, the Taylor-Column appears to follow the classic solution, with vertically uniform velocities. In visual observations the Taylor-Column has been observed to extend to the bottom of the tank. An important difference between $\pm Ro$ is the direction of the meridional circulation, and this could play a role. Further numerical work is to be performed to determine how the effects of stratification differ between the two states.

The vertical dependence of the Taylor-Column found experimentally is a unique result, and as such further experimental work is strongly recommended to investigate this in more depth. The automated PIV-system, with a few component upgrades and an investment in DaVis 8 or a similarly powerful PIV-package, provides a solid base for conducting further experimentation at a much increased parameter space at higher accuracy than could be achieved in the current investigation. Combined with further numerical and theoretical work a more detailed understanding of the new and unique flow phenomena discovered in the current study can be achieved.

Appendix A

List of Computers used for Numerical Simulation

Several machines have been used to perform numerical simulation. Initial runs have been performed on standard desktop machines, but most processing power has been provided by the supercomputers at the Centre for Scientific Computing at the University of Warwick. A list of the machines used is given below.

Skua

A 112 GB shared memory machine with 54 Itanium2 processors. After the commissioning of Francesca most other users of Skua migrated to the new system. Running code became free of charge on Skua, and with very few other users this became a viable platform to run code on. From mid 2008 an average of over 30 processors on Skua have been used to run simulations, until early 2010 when the experiment received priority and the average utilisation dropped to around 10 processors.

Francesca

A large cluster, divided into 240 nodes with two dual-core Xeon processors and 8GB of RAM each. Commissioned early 2008. Initially used to run simulation, but abandoned due to the high cost. Despite being 3 years younger than Skua, the performance per processor core was inferior to Skua.

Pentium-D

A standard RM desktop computer with a 3.4GHz Intel Pentium-D945 dual-core processor and 2GB of RAM. Used with both Windows and Linux. Used extensively for preliminary runs. Due to limited memory and its primary role as a work computer no longer used for simulations after resources on Skua became available.

Core2Duo

Desktop computer with a 1.86 GHz Intel Core2Duo E6300 dual-core processor, with 8GB of RAM. Used extensively for preliminary runs and compiler evaluation. After resources on Skua became available this machine was used extensively to test settings for spatial and temporal resolution of the numerical code.

Dual-Core Celeron

Low-cost desktop computer with a Celeron Dual Core 1.6GHz processor and 2GB of RAM, used in the lab for code development and initial PIV processing. During downtime in the lab used in a similar manner to the Core2Duo machine. Later cannibalised to build the PIV processing machine.

Appendix B

Circuit Diagrams

B.1 Motor Controller

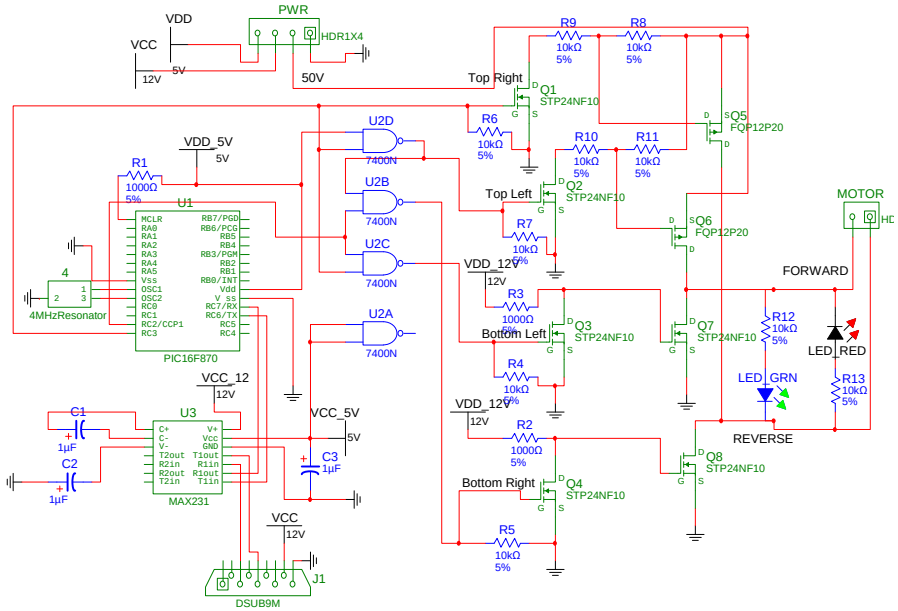

Figure B.1: The circuit diagram of the motor controller.

B.2 Motor Rotation Measurement System

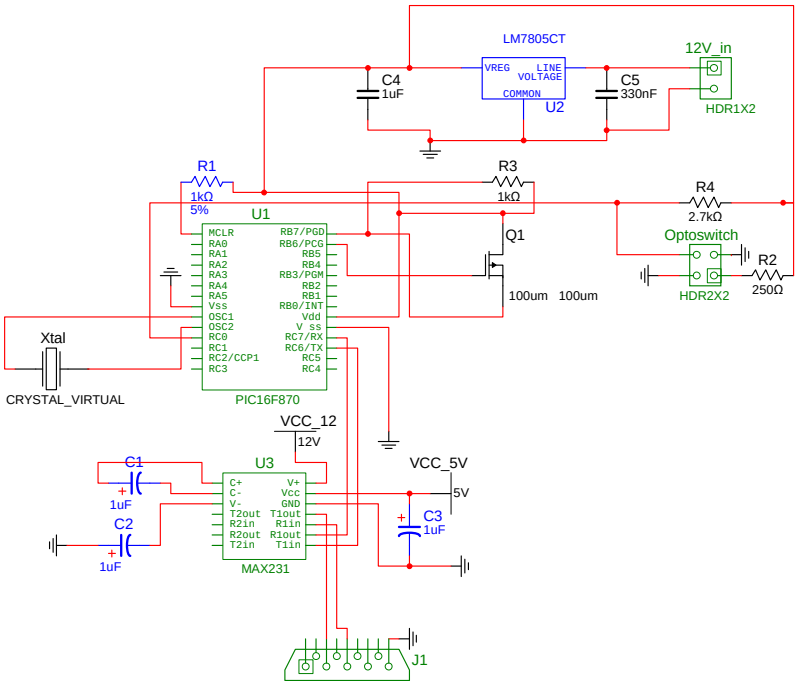

Figure B.2: The circuit diagram of the motor rotation and temperature measurement system.

B.3 Laser Control Box

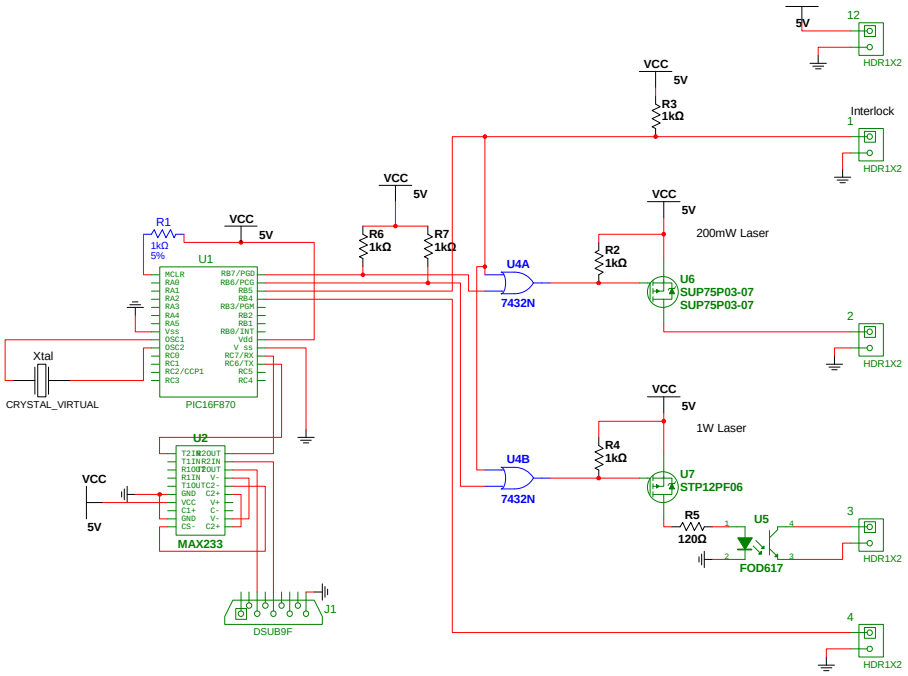

Figure B.3: The circuit diagram of the laser control box.

References

[1] Adrian, R. (1986). Multi-point optical measurements of simultaneous vectors in unsteady flow–a review. *International Journal of Heat and Fluid Flow*, **7**(2), 127–145.

[2] Adrian, R. (2005). Twenty years of particle image velocimetry. *Experiments in Fluids*, **39**(2), 159–169.

[3] Aguiar, A. C. B. (2008). *Instabilities of a shear layer in a barotropic rotating fluid*. Ph.D. thesis, St Hugh's College, University of Oxford.

[4] Analog Devices (2011). Low g accelerometers | MEMS |. http://www.analog.com/en/mems/low-g-accelerometers/products/index.html.

[5] Benton, E. and Clark Jr, A. (1974). Spin-up. *Annual Review of Fluid Mechanics*, **6**(1), 257–280.

[6] Brend, M. A. (2010). *Traversing SPIV for the measurement of vortex rings under background rotation*. Ph.D. thesis, School of Engineering, University of Warwick.

[7] Busse, F. (1968). Shear flow instabilities in rotating systems. *Journal of Fluid Mechanics*, **33**(03), 577–589.

[8] Cushman-Roisin, B. (1994). *Introduction to geophysical fluid dynamics*, volume 320. Prentice Hall.

[9] Früh, W. and Read, P. (1999). Experiments on a barotropic rotating shear layer. Part 1. Instability and steady vortices. *Journal of Fluid Mechanics*, **383**, 143–173.

[10] Graftieaux, L., Michard, M., and Grosjean, N. (2001). Combining PIV, POD and vortex identification algorithms for the study of unsteady turbulent swirling flows. *Measurement Science and Technology*, **12**, 1422.

[11] Greenspan, H. (1968). *The theory of rotating fluids*. Cambridge University Press.

[12] Hecht, E. (2001). *Optics*. Addison Wesley, 4th edition.

[13] Hide, R. and Titman, C. (1967). Detached shear layers in a rotating fluid. *Journal of Fluid Mechanics*, **29**(01), 39–60.

[14] Hollerbach, R. (1996). On the theory of the geodynamo. *Physics of the earth and planetary interiors*, **98**(3-4), 163–185.

[15] Hollerbach, R. (2000). A spectral solution of the magneto-convection equations in spherical geometry. *International Journal for Numerical Methods in Fluids*, **32**(7), 773–797.

[16] Hollerbach, R. (2003). Instabilities of the Stewartson layer Part 1. The dependence on the sign of Ro. *Journal of Fluid Mechanics*, **492**, 289–302.

[17] Hollerbach, R. (2006). The Magnetorotational Instability. In *Warwick Turbulence Symposium: Instabilities and Turbulence in MHD*.

[18] Hollerbach, R. (2009). Instabilities of Taylor columns in a rotating stratified fluid. *Physics Letters A*, **373**(41), 3775–3778.

[19] Keane, R. and Adrian, R. (1990). Optimization of particle image velocimeters. I. Double pulsed systems. *Measurement Science and Technology*, **1**, 1202.

[20] Lathrop, D. (2010). personal communication.

[21] LaVision GmbH (2011a). Lavision - particle image velocimetry (piv). `http://www.lavision.de/en/techniques/piv.php`.

[22] LaVision GmbH (2011b). Lavision press release: Enormous boost in processing speed. http://www.lavision.de/en/news/2010/1163/.

[23] Lourenco, L. and Krothapalli, A. (1995). On the accuracy of velocity and vorticity measurements with PIV. *Experiments in Fluids*, **18**(6), 421–428.

[24] Matsuda, T. and Hashimoto, K. (1978). The structure of the Stewartson layers in a gas centrifuge. Part 1. Insulated end plates. *Journal of Fluid Mechanics*, **85**(03), 433–442.

[25] Maxim-IC (2010). Ds18s20 high-precision 1-wire digital thermometer datasheet. `http://datasheets.maxim-ic.com/en/ds/DS18S20.pdf`.

[26] Maxworthy, T. (1970). The flow created by a sphere moving along the axis of a rotating, slightly-viscous fluid. *Journal of Fluid Mechanics*, **40**(03), 453–479.

[27] MiniTec UK Ltd (2011). Minitec profile system. `http://www.minitec.co.uk/profile_system.html`.

[28] Niino, H. and Misawa, N. (1984). An experimental and theoretical study of barotropic instability. *J. Atmos. Sci*, **41**, 1992–2011.

[29] Plascoat Systems Ltd (2011). Performance polymer alloy coating datasheet. http://www.plascoat.com/techdocs/datasheets/talisman_30.htm.

[30] Prasad, A. and Jensen, K. (1995). Scheimpflug stereocamera for particle image velocimetry in liquid flows. *Applied Optics*, **34**(30), 7092–7099.

[31] Proudman, J. (1916). On the motion of solids in a liquid possessing vorticity. *Proceedings of the Royal Society of London. Series A*, **92**(642), 408.

[32] Raffel, M., Willert, C., and Wereley, S. (2007). *Particle image velocimetry: a practical guide*. Springer Verlag.

[33] Schaflinger, U. and Stibi, H. (1987). On centrifugal separation of suspensions in cylindrical vessels. *Acta mechanica*, **67**(1), 163–181.

[34] Stanislas, M., Okamoto, K., Kähler, C., Westerweel, J., and Scarano, F. (2008). Main results of the third international PIV challenge. *Experiments in fluids*, **45**(1), 27–71.

[35] Stewartson, K. (1957). On almost rigid rotations. *Journal of Fluid Mechanics*, **3**(01), 17–26.

[36] Taylor, G. (1923). Experiments on the motion of solid bodies in rotating fluids. *Proceedings of the Royal Society of London. Series A, Containing Papers of a Mathematical and Physical Character*, **104**(725), 213–218.

[37] Triana, S. A. (2010). *Inertial Waves in a Laboratory Model of the Earths Core*. Ph.D. thesis, University of Maryland.

[38] Tritton, D. (1988). *Physical fluid dynamics*. Clarendon Press, Oxford.

[39] Vanyo, J. (2001). *Rotating fluids in engineering and science*. Dover Pubns.

[40] Vlaskamp, J. H. A. (2006). *The Flow around a Sphere in a Rotating Fluid*. Master's thesis, School of Engineering, University of Warwick.

[41] Wikipedia (2011). Scheimpflug principle. `http://en.wikipedia.org/wiki/Scheimpflug_principle`.

[42] Wilmshurst, T. (2010). *Designing embedded systems with PIC microcontrollers: principles and applications*. Newnes.

[43] Yoshimoto, T., Vlaskamp, J., Brend, M., Thomas, P. J., Murai, Y., and Takeda, Y. (2008). Twisted wake of a sphere in rotating fluid. *Bulletin of the American Physical Society, 61st Annual Meeting of the APS Division of Fluid Dynamics*.